SAPIENZA
UNIVERSITÀ DI ROMA

High resolution imaging and production of thin barriers for ultracold ^6Li Fermi gases

Master thesis in Physics

External Supervisor:
Prof. Massimo Inguscio

Internal supervisor:
Prof. Marco Grilli

Defended by:
Andrea Morales

Academic Year 2012-2013

Acknowledgements

First I would like to thanks Prof. Massimo Inguscio for the great occasion he gave me to work within the lithium project; it has been a fruitful and fantastic experience to enter this challenging field of Physics. Secondly I have to thank Prof. Grilli for his patience in helping me in whatever I needed, from Physics to bureaucracy. Thank you very much.

But my deepest gratitude goes to Giacomo Roati and Matteo Zaccanti, to have welcome and accompanied me into this field, with enthusiasm and passion. Thanks to Matteo for the wonderful talks on Physics, early in the morning on the roof of LENS. I experienced from each of them. It has been really great to learn physics from you. Thanks to Giacomo to have encouraged me in my skylls and to have taught me the way of getting things to work, even when it seems very hard. Thanks also for supporting me in these months. Thanks to both for the responsibilities you decided to give me, it has been fantastic to work with both of you. I will never forget the night in which eventually we obtained our first molecular BEC with 6Li. You gave me a real feeling of what working in a group means.

Thanks to the rest of the lithium group, Giacomo, Jorge and Alessia who helped me during these months in understanding the experiment and answering my doubts. You have all been very kind to me. Thanks to the rest of the quantum degenerate physics group at LENS who have welcome me so warmly.

I would probabily not be here if it wasn't for my wonderful family, that supported me in these months of hard and intense work and in the previous years of study. You have all been fundamental to this achievement. I owe you everything. This work is dedicated to you.

Finally my thanks go to my friends in Rome, with whom I grew up as a young physicist, sharing knowledge and fun, which I will never forget about. Thanks to everyone. I wish you all the best.

A.M.

To my family,
Piero, Carla and Raffaello

Contents

Introduction

In the seminal lecture of 1982 [1], R.Feynman's proposed the idea of *quantum simulation* as a novel tool to address quantum many body physics in a more controlled way.

In this framework, ultra cold atoms are enjoying widespread interest both in the quantum many-body and atomic physics communities, due to the unprecedented control of most of the experimental parameters, that allows the unique possibility of implementing strongly-correlated quantum models [2, 3].

In particular, the combination of ultracold atomic gases and optical potentials has opened up a new way to study condensed matter problems. In fact it is possible to realize artificial quantum environments that mimic conventional but also exotic systems in nature, as for example, ordinary crystals and graphene [4]. In addition, interactions between atoms can be freely manipulated from the negative infinity to the positive infinity by means of Feshbach resonances [5], allowing the studying of both weakly and strongly correlated systems.

This interest has been demonstrated by recent outstanding results achieved with both bosonic and fermionic systems, addressing new quantum phases, typically inaccessible by conventional room temperature experiments [3].

Among the latest most exciting results, was the observation of superfluidity in fermionic systems [6]. Superfluidity is one of the most spectacular phenomena in nature, intimately connected to superconductivity, being a superfluid essentially a superconductor carrying zero charge.

In particular some shared properties between high-T_c superconductors and ultra-cold atomic strongly interacting fermions demonstrates as these last may provide interesting insights into this exciting and challenging field.

With ultra-cold fermions it is possible, crossing a Feshbach resonance - to explore continuously the transition between a molecular Bose-Einstein condensate (mBEC) and a superfluid of Cooper-like pairs described by the Bardeen-Cooper-Schrieffer theory (BCS).

At the resonance, between the two regimes, many-body effects in the form of strong correlations become dominant and the size of the pairs become much smaller than the one of conventional Cooper pairs. The same feature is observed in a high-T_c superconductor, showing the strong link among these two systems. This regime is known in literatures as BEC-BCS crossover [7, 8].

Towards the quantum simulation of high-Tc superconductors, people are now designing and setting up always more sophisticated experimental apparatus to implement Fermi-Hubbard hamiltonians on these atomic systems.

These models are supposed to unveil the physics of these exotic and intrigu-

ing superconducting materials. Their phase diagram is indeed considered the Holy Grail in the theory of strongly correlated systems. The ground state properties are largely under debate. One possibility is that these models may support (in some limit) the d-wave superconducting phase at high-Tc. At the moment there is neither analytical nor numerical results that can support conclusively this hypothesis.

The direct implementation of these quantum Hamiltonians with degenerate atomic fermions may provide useful information to this debate, eventually addressing also the intriguing interplay between superfluidity and disorder that may be added into those atomic systems via optical laser speckles [9, 10].

This thesis fits in this context, describing a new-generation experimental set-up devoted to the production of superfluid Fermi gases of lithium atoms. In particular, during my work, I have developed and applied new experimental schemes to produce, to observe and to manipulate strongly-correlated fermions.

Within the period of my work at LENS (European Laboratory for Non-Linear Spectroscopy) my main contributions have been:

- Project, realization and characterization of a compact optical set-up to produce and imprint sheet-shaped optical potentials, with extension comparable to the correlation length of the fermionic superfluid system. This kind of potential acts like a thin barrier that will be used for example to initially segregate different spin components or to study coherent Josephson-like tunneling of pairs, mimicking the ordinary superfluid junctions.

- Project and characterization of an optical imaging system to image the atoms with a final tested resolution of $\sim 1\mu$m. High-resolution imaging is indeed becoming one of the main and mandatory tool that allows to extract the wavefunction behavior of the system.

- I was also deeply involved in the successful implementation of a new cooling scheme which allowed us to cool the temperature of the magneto-optical-trap (MOT) of fermionic lithium to temperatures well below the previous limit. This technique will be surely applied in many other laboratories worldwide.

- I have aligned and characterized the optical potential where the last stage of cooling to quantum degeneracy is performed. In particular, we have finally observed a molecular Bose-Einstein condensate of lithium atoms. This is the first important step towards the production of an atomic superfluid Fermi gas of Lithium.

This thesis is divided into four chapters:

- In *chapter one* I describe the properties of Fermi gases and cooling techniques; then I illustrate in some details the main features of ^6Li atoms.
- In *chapter two* I describe the experimental apparatus which is able to produce superfluid gases of fermionic atoms.
- In the *third chapter* I describe the optical setup that I have realized to imprint optical potentials on the atomic cloud and improve the imaging system of the experiment. Here I also report the measurements I have done to characterize this setup.
- In *chapter four* I first present the experimental implementation of a new cooling scheme based on D1 transition line. In the second part I describe the experimental realization of a molecular Bose-Einstein condensate (mBEC) made of atomic fermions.

Chapter 1

Degenerate Fermi gases: Theory and Cooling Techniques

This chapter is divided in three sections. In the first one we start with recalling some concepts of quantum statistics, with particular attention to fermions. We will then step through the collisional properties of a fermionic gas and approach a general description of the Feshbach resonances. In the second section I describe the lithium 6 atomic structure. The third section gives an overview of the laser cooling techniques which we employed in our experiment, giving some fundamentals theoretical details.

1.1 The role of quantum statistics in ultra cold atoms

Quantum statistic of particles: bosons *versus* fermions

Quantum statistics is what we use to distinguish fermions from bosons in a quantum theory. In such a theory trajectories lose their meaning and two identical particles can no longer be distinguished. In particular the state of a physical

system made of N indistinguishable particles is determined by a set of quantum numbers addressing their properties, namely the positions, the spins and the energy. Indistinguishability means that an exchange of any two particles a and b of the system will not be detectable in terms of any physical measure. This has tremendous consequences on the nature of particles. In fact, if we consider for simplicity a system of two particles (N=2)[1], in terms of its wavefunction this means that the physical state obtained by exchanging the two particles with each other, must be, in force of their identity, physically equivalent to the first one, i.e. their wavefunctions can differ just for an arbitrary phase[2]. This reads as

$$\psi(\zeta_1, \zeta_2) = e^{i\alpha}\psi(\zeta_2, \zeta_1) \tag{1.1}$$

α being a real constant and ζ addressing all the relevant coordinates of the particles. If we do the exchange again we go back to the initial configuration, but the function ψ will be multiplied by $e^{2i\alpha}$. This can only mean that $e^{2i\alpha} = 1$, i.e. that $e^{i\alpha} = \pm 1$ and to conclude we get the symmetry/antisymmetry condition for the wavefunction

$$\psi(\zeta_1, \zeta_2) = \pm\psi(\zeta_2, \zeta_1) \tag{1.2}$$

If the wavefunction stays unchanged under any exchange of identical particles it is said *symmetric* (bosons); if it does change sign it is said *antisymmetric* (fermions). We point out that indistinguishability implies that we cannot decide which particle is in a certain quantum state, but we can only know how many particles occupy that state. This means that the wave function of a fermionic/bosonic two particle system with particles in different states E_1 and E_2 must take into account both the situations in which particle 1 is in E_1 and particle 2 is in E_2, and its reversed situation:

$$\psi(\zeta_1, \zeta_2) = \frac{1}{\sqrt{2}}[\psi_{E_1}(\zeta_1)\psi_{E_2}(\zeta_2) \pm \psi_{E_2}(\zeta_1)\psi_{E_1}(\zeta_2)] \tag{1.3}$$

where the plus holds for bosons and the minus for fermions. For a system of N fermionic particles (minus sign), the state of the system can be conveniently written in the form of a *Slater determinant*:

$$\Psi_{n_1,n_2.....n_\infty}(x_1, ..., x_N) = \frac{1}{\sqrt{N!}} \begin{vmatrix} \psi_{E_1}(x_1) & \psi_{E_1}(x_2) & \dots & \psi_{E_1}(x_N) \\ \psi_{E_2}(x_1) & \psi_{E_2}(x_2) & \dots & \psi_{E_2}(x_N) \\ \dots & \dots & \dots & \dots \\ \psi_{E_N}(x_1) & \psi_{E_N}(x_2) & \dots & \psi_{E_N}(x_N) \end{vmatrix} \tag{1.4}$$

[1] The argument can be extended easily to systems with an arbitrarly large number of identical particles (see [11]).

[2] In fact the modulus of the wavefunction contain all the physical information.

where the exchange of two columns (two particles) reproduce the correct change in the sign. We also note that if two columns are equal, by definition of determinant, the wavefunction is zero. This is the true fingerprint of fermions, also know as *Pauli exclusion principle*, stating that two fermions can never occupy the same quantum state, being their wavefunction always zero in that case. This is clearly visible also in equation 1.2 and tells us that for a fermionic system the occupancy number of any quantum state, i.e. the number of particles occupying a certain quantum level, can only assume the values 0 or 1.

Quantum statistics of atoms

The statistics of *composite particles* (like atoms) is determined by the parity of the number of elementary fermions which actually form it. Exchanging a couple of composite particles corresponds to simultaneously exchanging multiple elementary identical particles pairs. Then all particles made up of an odd number of elementary fermions obey the *Fermi-Dirac Statistics* for fermions, while the ones made up of an even number of them obey the *Bose-Einstein Statistics* for bosons.

Grand canonical ensemble

The fact that we can only know how many particles occupy a certain state makes the so called *grand canonical ensemble* picture the most suited to describe quantum systems. It can be used to describe systems in contact with a reservoir with which they can exchange particles and energy. The Boltzmann factor $e^{-(E_T-\mu N)/k_BT}$ gives the probability that the system is in any state with particle number N and total energy E_T, where μ and T have to be thought of as parameters imposed by the reservoir. We can add quantization to the picture by considering a non interacting quantum gas of particles, characterized by quantum levels of energy E_i, n_i being the corresponding occupancy number. Then the canonical partition function can be written as

$$Z = \sum_{\{n_i\}} e^{-(\sum_i E_i n_i - \mu n_i)/k_BT} = \tag{1.5}$$

$$= \sum_{\{n_i\}} \prod_i e^{-n_i(E_i-\mu)/k_BT} \tag{1.6}$$

where $E_T = \sum_i E_i n_i$. Using that $n_i = 0, 1$ for fermions and any positive integer for bosons we get the partition functions for bosons and fermions:

$$Z_{Bosons} = \prod_i \frac{1}{1 - e^{-(E_i - \mu)/k_B T}}$$
$$Z_{Fermions} = \prod_i \left(1 + e^{-(E_i - \mu)/k_B T}\right) \tag{1.7}$$

Both of them at high temperature $T \gg \mu$ tend to the Maxwell-Boltzmann distribution.

Dilute regime

At high temperature we cannot distinguish fermions from bosons. The quantum nature of particles is somehow obscured as long as the extension of their wave packets is small compared to the interparticle spacing. As long as this holds, the particles of a system stay distinguishable and their quantum statistics is not crucial to describe the properties of the system. But as the temperature is lowered, quantum mechanics becomes important: the length scale associated to the propagation of each particle or to the extent of its wave function - the so called *de Broglie wavelength*- depends on temperature as $\lambda_{dB} \propto 1/\sqrt{T}$. Thus, at very low temperature, it eventually becomes comparable with interparticle spacing, which depends on the density n of the gas as $n^{-1/3}$. When this happens, particles start to behave as waves and their quantum statistics eventually becomes relevant. As the temperature approaches zero, for bosons a phase transition to a Bose-Einstein condensate (BEC) occurs ($T < T_c$), while identical fermions -according to the Pauli principle - start to populate with one particle the lowest energy states available up to a Fermi energy E_F ($T < T_F$): we enter the regime of quantum degeneracy of the gas. From a quantum statistical point of view this occurs when in a volume Ω the number of available quantum states, which is roughly given by Ω/λ_{dB}^3 becomes comparable to the number of particles N, i.e. when the condition $n\lambda_{dB}^3 \sim 1$ is met. Unfortunately in experimental laboratories, at the temperatures required for quantum degeneracy to occur , essentially all gases are solid, the only exception being Helium. The only way out is to work out of equilibrium in the *dilute regime* $n < 10^{15} cm^{-3}$. In fact before a gas of atoms can form a solid, a certain amount of time is needed, allowing three atoms to collide together to form a molecule, the third particle carrying away the released energy and momentum. We need our gas to thermalize on a time scale smaller then this time window, so that we can perform experiments on it. It turns out that while thermal equilibrium only requires *two body* collisions, whose rate is proportional to the density, molecules formation requires

(at least) *three body* collisions, whose rate is proportional to the density square. Then at low enough density we enter the regime in which three body collisions are strongly suppressed in the gas and the lifetime of our quantum degenerate gas is extended.

1.1.1 More on Fermi gases

Fermions are all particles whose spin is a half integer number, obeying the Pauli exclusion principle. For this reason they are much more difficult to cool when compared to bosons, because at very low temperature the elastic scattering cross section is strongly Pauli suppressed since identical fermions can not occupy the same position in space: thermalization processes involved in fundamental cooling techniques such as evaporative cooling becomes inefficient.
The statistic of these particles is described by the well known *Fermi-Dirac distribution*, which is obtained by the second of 1.7 as

$$\boxed{\langle n_F \rangle = k_B T \frac{\partial ln Z}{\partial \mu} = \frac{1}{e^{\beta(E-\mu)}+1}} \tag{1.8}$$

providing the average number of fermions[3] occupying the quantum level with energy E, being μ the *chemical potential* of the gas and $\beta = 1/k_B T$. In accordance with the Pauli Principle this averaged value is always lower than one. The following limits hold:

- High temperature limit:

$$\langle n \rangle = z e^{-\beta E} \quad with \quad z \equiv e^{\beta\mu} \equiv fugacity \tag{1.9}$$

- Low temperature limit:

$$\langle n \rangle = \langle n \rangle_{T=0} + \frac{sign(E-\mu)}{exp(\beta|E-\mu|)+1} \tag{1.10}$$

A plot of the FD distribution is reported for both $T = 0$ and $T/T_F \ll 1$, T_F being the Fermi temperature defined by eq. 1.18. At zero temperature fermions populate all the momentum states available for the system starting from the ground state, up to a maximum level known as *Fermi level* (k_F) with an associated *Fermi energy* (E_F) such that:

$$E_F = \frac{(\hbar k_F)^2}{2m} \tag{1.11}$$

[3]For bosons the calculation is the same and the result has just the opposite intermediate sign.

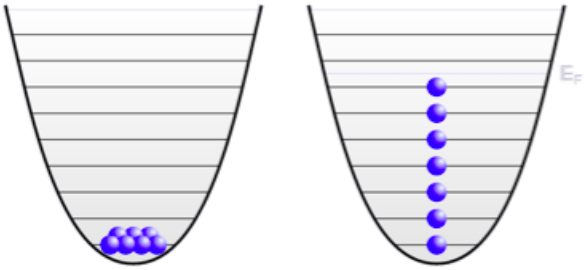

Figure 1.1: *Different configurations for a system of bosons (left) and fermions (right) at zero temperature.*

All these states together form the *Fermi sphere*. At low but finite temperature the distribution is significantly modified only in the vicinity of the Fermi level, i.e. in the vicinity of the Fermi surface of the sphere: these states are the only one important to affect the physical properties of the system described by its thermodynamics quantities (E, S, N, ecc).

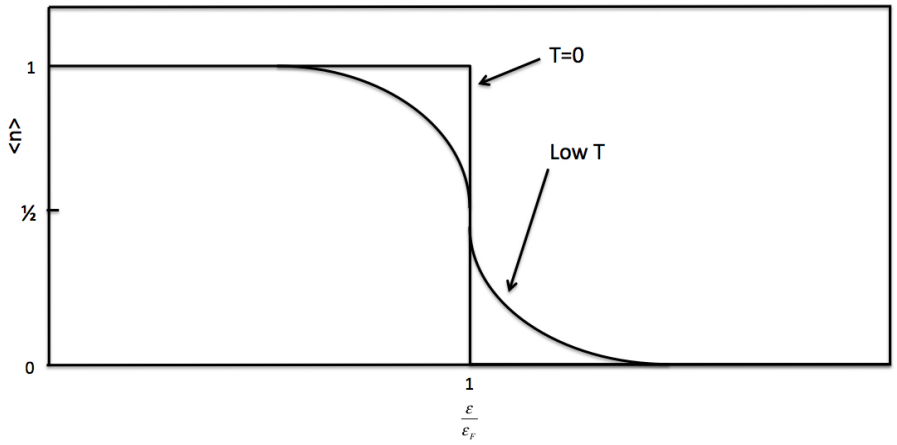

Figure 1.2: *Plot of the average occupation number of fermionic system for* $T = 0$ *and* $T < T_F$*. The function is modified only in the vicinity (*$\sim k_B T/E_F$*)of the fermi value of the energy. For T=0 the first derivative diverges at* $E = E_F$*; as soon as* $T \neq 0$ *it become finite.*

To calculate thermodynamics quantities it is useful to introduce the *density of states* $g(E)$ which counts how many states the system has for each energy value. We can use it to evaluate the total number of particles

$$N = \sum_{statess} \langle n_s \rangle = \int dE \; g(E) \; \frac{1}{e^{\beta(E-\mu)} + 1} \tag{1.12}$$

The analytic dependence of the $g(E)$ on the relevant quantities reads as

$$g(E) = c_\alpha E^{\alpha-1} \tag{1.13}$$

α being a coefficient dependent on the dimension and on the potential acting on the system and c_α a coefficient independent from the energy.

Interesting Physical Systems

	Homogeneous Gas	**Harmonic potentials**
3D	$\alpha = 3/2$	$\alpha = 3$
2D	$\alpha = 1$	$\alpha = 2$
1D	$\alpha = 1/2$	$\alpha = 1$

We shall see that in ultra-cold atoms experiments the trapping potential is realized via magnetic fields or focussed laser radiation; this potentials are usually harmonic near the center of the trap. We report in the table above some values of α for the most relevant physical situations. The total energy of the system reads as

$$E = \int_0^\infty g(E')\ n(E')\ E'\ dE' \tag{1.14}$$

Since the levels in a narrow interval centered around the Fermi sphere are the only one that contribute to the thermodynamics at very low temperature, we can evaluate integrals in 1.12 and 1.14 expanding $g(E)$ near its value at E_F

$$g(\epsilon) \sim g(E_F) + \frac{dg}{dE}\Big|_{E=E_f} \delta E \tag{1.15}$$

We get respectively

$$Small\ T\ :\quad \begin{cases} N \sim \dfrac{1}{\alpha}\ E_F\ g(E_F)\Big[1 + \dfrac{\pi^2}{8}\big(\dfrac{K_B T}{\mu}\big)^2 \alpha(\alpha-1)\Big] \\ E \sim E(T=0)\Big[1 + \dfrac{\pi^2}{8}\big(\dfrac{K_B T}{E_F}\big)^2 (\alpha+1)\Big] \end{cases} \tag{1.16}$$

these being correct on the order $O(\frac{T}{E_F})^2$ [12].

Homogeneous gas

- 3D

  In this case we have $c_{\alpha=3/2} = \Omega\frac{(2\pi)(2m)^{3/2}}{\hbar^3}$. Using 1.16 we find

$$T = 0\ :\quad \begin{cases} E = \dfrac{3}{5} N E_F \\ N = \Omega \dfrac{k_F^3}{6\pi^2} = \Omega\rho \end{cases}$$

- 2D
  In this specific case, in which $c_{\alpha=1} = \left(\frac{2\pi m}{h^2}\right)\Omega$, we can evaluate both N and E in a non approximated way (analitically) to find

$$Any\ T\ :\quad \begin{cases} E = \dfrac{3}{5}NE_F \\ \dfrac{N}{\Omega} = \dfrac{1}{\lambda_T^2} log(1+e^{\beta\mu}) \end{cases} \qquad with \qquad \lambda_T = \frac{h}{(2\pi m k_B T)^{1/2}}$$

Harmonic Potential

As mentioned before the trapping potential employed in an ultra-cold atom experiments is usually harmonic. We assume here the potential to be isotropic.

- 3D
  For this physical configuration we have $c_{\alpha=3} = \frac{1}{2(\hbar\omega)^3}$ and for 1.12 and 1.14 we find:

$$T = 0\ :\quad \begin{cases} E = \dfrac{3}{4}NE_F \\ N = \dfrac{1}{6}\dfrac{E_F^3}{(\hbar\omega)^3} \end{cases}$$

  Inverting the first equation we get the following value for the Fermi Energy

$$E_F = (\hbar\omega)(6N)^{1/3} \tag{1.17}$$

  We observe that the same dependence on total number of particles and trapping potential frequency is found for the BEC critical temperature $T_c \propto \hbar\omega N^{1/3}$ (see for example [13]). This allows us to say that the energy scale for Fermi degeneracy in a harmonic potential, is basically given by the *Fermi energy*. In term of temperature one can introduce a *Fermi temperature* simply defined by:

$$T_F = \frac{E_F}{k_B} \tag{1.18}$$

1.2 Collisional properties of a weakly interacting ultracold gas

Here we recall the collisional properties of an ultra cold gas, meaning we describe how the scattering cross section and amplitude behave when we change the energy and/or some parameters of the system, as a magnetic field. Scattering amplitude is linked to the parameters which control the interaction between atoms.

General overview

In any real gas the atoms interact mutually through some interatomic potential. If we neglect the weak magnetic dipole interaction between the spins, the interatomic interaction is described by a central potential V(r) that, at large relative distances, is given by the *van der Waals* potential $\sim -\frac{C_6}{r^6}$ due to mutual interaction between the fluctuating electric dipoles of the atoms. In fact the fluctuation of the electronic cloud around the nucleus of the atom 1 can temporarily generate a dipole moment p_1 with an associated electric dipole field $E_1 \sim \frac{p_1}{r^3}$. This field can induce a second dipole moment p_2 on a close atom (2). If atom 2 has polarizability α, the strength of the induced dipole is given by $p_2 = \alpha E_1 = \alpha \frac{p_1}{r^3}$. Then the interaction potential energy between atoms 1 and 2 depends only on the relative interparticle distance r and is given by $V(r) \sim -\frac{p_1 p_2}{r^3} = -\frac{\alpha p_1^2}{r^6} < 0$, whose sign means attractive interaction. This interaction is then **isotropic** (central field like) and **short range** ($\sim 1/r^6$), the latter meaning that beyond a certain distance r_{vdW} the interaction is negligible. This holds down to a few a_0 distance, below which the two electron clouds touch each other and strong Coulomb interaction prevents the atoms to come further close by. This can be approximated as a hard-wall repulsive interaction. The distance r_{vdW} is called the *range* of the potential. From a general point of view, it is important to point out that interactions among atoms does affect the thermodynamics of the gas as well as its kinetics. With *thermodynamics*, we mean that interaction does change the relation between pressure and temperature, i.e. the equation of state of the gas. With *kinetics* on the other side, interactions determine the time scale over which thermal equilibrium is reached.

At very low temperatures the stable phase of any gas is the solid one (Helium being the only exception). But as we said, in ultra dilute regime it can take minutes for the gas to fall in its solid ground state. This is due to strong suppression of three-body collisions -which are required to form molecules and larger clusters of bond atoms (see paragraph *Dilute regime*)- with respect the two-body kind, that allow thermalization of the gas through elastic collisions and subsequent redistribution of momentum among atoms. In this sense, inelastic collisions between particles are strongly unwanted, for they lead to change in the internal states of the involved atoms and subsequent trap loss. Fortunately they can be eliminated by keeping atoms in the lowest internal energy states.

Thus for sufficiently low densities the behavior of the gas is governed by two-body interactions, i.e. the probability of finding three atoms simultaneously within a sphere of radius r_{vdW} is much smaller then the one of finding just two of them within it. This condition is satisfied in the dilute regime, when the mean

inter particle spacing $n^{-1/3}$ is much larger than the range r_{vdW}, i.e. when:

$$nr_{vdW}^3 \ll 1 \qquad (Dilute) \tag{1.19}$$

More, the gas is ultra cold, which means that typical collisions occur at low relative momenta compared to the scale $1/r_{vdW}$ of the potential:

$$k \ll \frac{1}{r_{vdW}} \qquad (Ultra\ cold) \tag{1.20}$$

and the relative de Broglie wavelength is $\lambda_{dB} = 2\pi/k \gg r_{vdW}$. In these regime of low-energy scattering processes, the details of the true short-ranged interaction potential is never explored. In other words it can be thought that, since particles are widely delocalized in space at very low temperature, they experience the interaction potential on a large region of space, and thus are sensitive to an effective interaction resulting from the average potential within this region. This allows for modeling the real two body scattering potential in real space with a delta-like pseudo potential, which is much easier for theoretical description.

1.2.1 Elastic scattering and pseudo-potential

In this section we follow the approach of [14]. As we saw due to the diluteness of the gas, two body collisions are predominant. Two body physics is easy to describe in the center-of-mass frame of the colliding atoms, where $\mu = m/2$ is the reduced mass and $\vec{k}$ the relative wave vector before the scattering. The Schrödinger equation for the scattering problem can be written as

$$(H_0 + V)|\psi\rangle = E|\psi\rangle \tag{1.21}$$

where H_0 is the kinetic energy for the free particle[4] (plane wave) and V is the interaction potential. The solution for the ket $|\psi\rangle$ can be found in the complex plane avoiding the singularity of the operator $\frac{1}{E-H_0}$ as

$$|\psi\rangle = |\phi\rangle + \frac{1}{E - H_0 \pm i\epsilon} V|\phi\rangle \tag{1.22}$$

This is the so called **Lippman-Schwinger equation** for the ket in the Hilbert space. It shows how the wave function in the presence of a center of diffusion is made up by the sum of the incident plane wave plus the effect of the diffusion[5].

[4] Because we are dealing with elastic scattering, the eigenstate of the energy E is the same for the states of the system who do not experience V.

[5] V is assumed to have a finite range, as in all physically interesting problems, and to be local, i.e. diagonal in the position representation: $\langle x'|V|x"\rangle = V(x')\delta^3(\vec{x}' - \vec{x}")$. The finite range can be introduced manually with a cut-off in momentum space, or it can be deduced by the proper scale of the potential at play.

For $V \to 0$, ψ reduces to the solution ϕ of the unscattered plane wave. Projecting equation 1.22 on the basis of the positions and using the residues theorem, the *Green function* of the problem can be evaluated as

$$G_{\pm}(\vec{x}-\vec{x}') = \frac{\hbar^2}{2\mu}\langle x\Big|\frac{1}{E-H_0\pm i\epsilon}\Big|x'\rangle = \\ = \int \frac{d^3p}{(2\pi)^3}\frac{e^{i\vec{p}\cdot(\vec{x}-\vec{x}')}}{k^2-p^2+i\epsilon'} = -\frac{1}{4\pi}\frac{e^{\pm ik|\vec{x}-\vec{x}'|}}{|\vec{x}-\vec{x}'|} \tag{1.23}$$

the plus and minus sign being referred to the incoming or outgoing spherical wave. Eq. 1.23 contains all the meaningful physical properties of the scattering processes and it can be used to write the explicit form of the scattered wave function:

$$\psi^{\pm}(\vec{x}) = e^{i\vec{k}\cdot\vec{x}} + \int d^3x' G_{\pm}(\vec{x}-\vec{x}')V(\vec{x}')\psi^{\pm}(\vec{x}') \tag{1.24}$$

Eq. 1.23 is also the solution of the Helmholtz equation $(\nabla^2+k^2)G_{\pm}(\vec{x}-\vec{x}') = \delta^{(3)}(\vec{x}-\vec{x}')$ for a point-like source of scattering. It is indeed a more general result [12] that the effect of any finite range potential can be described in terms of point-like (delta) sources of scattering. Considering the outgoing wave (+) far from the region of interaction, i.e. for $r = |\vec{x}| \gg |\vec{x}'| = r'$, one can use $|\vec{x}-\vec{x}'| \sim r - \hat{r}\cdot\vec{x}'$ to find that

$$\boxed{\psi^{+}(\vec{x}) = \langle x|\psi^{+}\rangle \xrightarrow{r\gg 1} e^{i\vec{k}\cdot\vec{x}} + \frac{e^{ikr}}{r}f(\vec{k}',\vec{k})} \tag{1.25}$$

where $\vec{k}' = k\ \hat{r}$ is the diffused wavevector (in accordance to elastic condition $k = k'$), and $f(\vec{k}',\vec{k})$ is the **scattering amplitude** defined as

$$f(\vec{k}',\vec{k}) = -\frac{1}{4\pi}\int d^3x' e^{-i\vec{k}'\cdot\vec{x}'}\frac{2\mu}{\hbar^2}V(x')\langle x'|\psi^{+}\rangle \tag{1.26}$$

This is easily related to the *differential scattering cross-section* as $\frac{d\sigma}{d\Omega} = |f(\vec{k}',\vec{k})|^2$, while the *total scattering cross section* σ_{tot} is provided by integration over the solid angle. Despite the appearance, equation 1.26 is an integral equation for the scattering amplitude, where the n-th order contains n times the potential V. It is thus perfectly suited to implement a perturbative approach. Substituting eq. 1.25 in 1.26, to second order one gets:

$$f(\vec{k}',\vec{k}) = -\frac{2\mu V(\vec{k}'-\vec{k})}{4\pi\hbar^2} + \int \frac{d^3p}{(2\pi)^3}\frac{V(\vec{k}'-\vec{p})\ f(\vec{p},\vec{k})}{k^2-p^2+i\epsilon} \tag{1.27}$$

The latter equation shows explicitly how interactions due to the interparticle potential are mediated by scattering processes, described by the scattering amplitude $f(\vec{k}',\vec{k})$. For a contact potential in real space of the form

$$V(\vec{r}) = g\ \delta^3(\vec{r}) \tag{1.28}$$

we get a constant potential in momentum space and equation 1.27, at the lowest order, gives the so called *Born approximation*

$$f \sim -\frac{1}{4\pi}\frac{g\ m}{\hbar^2} = f_{Born} \tag{1.29}$$

Within this model f is independent of the scattering angle between k and k' and is therefore adequate to describe isotropic scattering. In ultra cold atoms interaction potential has a Lennard-Jones shape due to van der Waals interactions ($\sim -\frac{1}{r^6}$) at long distances and strong repulsion of electronic clouds at short distances ($\sim \frac{1}{r^{12}}$). Therefore the central nature of this potential allows to express the scattering amplitude in terms of the scattering angle θ between k ad k' and of the incident energy $E \sim k^2$. This spherical symmetry means the hamiltonian H commutes with the angular momentum L ($[H, L] = 0$) leading to factorization of the radial part of the wavefunction from its angular one. The scattered wavefunction thus results axially symmetric with respect to the incident wavevector k and can be written as

$$\psi_k(\vec{r}) = \sum_{l=0}^{\infty}\sum_{m=-l}^{m=l} Y_{l,m}(\theta,\phi)\frac{u_{k,l,m}(r)}{r} \tag{1.30}$$

where ϕ is the azimuthal angle and $Y_{l,m}(\theta,\phi)$ are the eigenfunctions of the angular momentum L. The problem 1.21 is solved when equation

$$u"_{k,l,m}(r) + \Big(k^2 - \frac{l(l+1)}{r^2} - \frac{2\mu V(r)}{\hbar^2}\Big)u_{k,l,m}(r) = 0 \tag{1.31}$$

is satisfied for every k, l, m. Thus, the Schrödinger equation for the complete wavefunction splits into infinite equations, one for each angular momentum component. This is the mathematical expression of the physical fact that central fields cannot change angular momentum. If we assume k parallel to z, the incoming wave is eigenstate of L_z operator with eigenvalue $m = 0$ [6], and can be written with partial wave expansion [11] in terms of Legendre polynomials P_l as

$$\psi_k(\vec{r}) = \sum_{l=0}^{\infty} P_l(cos\theta)R_{k,l}(r) \tag{1.32}$$

where $R_{k,l}(r) = \frac{u_{k,l,m=0}(r)}{r}$. Solving equation 1.31 one finds $R_{k,l}(r) \propto \frac{1}{r}sin\big(r - l\frac{\pi}{2} + \delta_l\big)$ that can be substituted in 1.32 and by comparison with the partial wave expansion of 1.25 gives, for the scattering amplitude, the expression

$$f(k,\theta) = \frac{1}{2ik}\sum_{l=0}^{\infty}(2l+1)(e^{2i\delta_l} - 1)P_l(cos\theta) \tag{1.33}$$

[6] The fact that the angular momentum component along the propagation axis must vanishes is pretty clear classically since $\vec{L}\cdot\vec{p} = (\vec{r}\times\vec{p})\cdot\vec{p} = 0$

Due to conservation of the flux for each l, each component of the scattered wave differs, from the one of the incoming wave, by only a phase shift δ_l [11, 14]. If we furthermore consider the ultracold regime, i.e. the limit $k \ll 1/r_0$ - r_0 being the range of the potential- the phase shifts behave as $\delta_l = k^{2l+1}$ and for small k, all terms with positive l are negligible with respect to $l = 0$ ($\delta_{l>0} \ll \delta_{l=0}$). This can be heuristically explained by classic arguments: the effective potential in eq. 1.31 is made of two parts,

$$V_{eff} = V(r) + \frac{\hbar^2}{2\mu}\frac{l(l+1)}{r^2} \tag{1.34}$$

where the short ranged interaction potential is summed to the centrifugal barrier. For small k values, particles with $l > 0$ can not penetrate the centrifugal barrier and thus they never experience the potential $V(r)$ inside it. In contrast, particles with $l = 0$ (*s-wave*) do not feel any centrifugal repulsion, and thus they are the only one scattering in the small k limit. Thus at low energy and for any short ranged potential, particles interact only in the isotropic s-wave channel[7]. Equation 1.33 reduces in this limit to [11]

$$f \sim f_{s-wave}(k) = \frac{1}{2ik}(e^{2i\delta_s} - 1) = \frac{1}{kcot\delta_s - ik} \sim \frac{1}{(-\frac{1}{a} + r_{eff}\frac{k^2}{2}) - ik} \tag{1.35}$$

where we have expanded $k \cdot cot\delta_s$ for $k \ll \frac{1}{r_0}$ up to 2^{nd} order in k and defined the **scattering length** as

$$a = -\lim_{k\to 0}\frac{tan\delta_s}{k} \tag{1.36}$$

where r_{eff} is the *effective range* for the potential. The value of both a and r_{eff} are set by the microscopic details of the interatomic potential. Importantly completely different microscopic interactions can lead to the same low-energy scattering amplitude: one can thus substitute the true complicated interatomic potential with a much simpler effective interaction parametrized by the scattering length a and the effective range r_{eff}.

Accounting for indistinguishability among particles results in (anti) symmetrization of the wave function for (fermions) bosons, which slightly modifies the differential cross section as:

$$\left(\frac{d\sigma}{d\Omega}\right)_{identical} = |f(\theta) \pm f(\pi - \theta))|^2, \qquad 0 < \theta < \pi/2 \tag{1.37}$$

[7] In equation 1.26 for finite range (r_0) potentials, only $\vec{x}'$ inside the range contribute to f: when $k \to 0$, $e^{-i\vec{k}'\cdot\vec{x}'} \sim 1$ and f become independent of the scattering direction. Time reversal symmetry guarantees independence also on the incident direction, and thus $f(\theta)$ is independent of the scattering angle θ.

This leads from eq. 1.35 for $k \to 0$ to [11]:

$$\begin{cases} \sigma_{id.bosons} = \dfrac{8\pi a^2}{1+k^2a^2} \\ \sigma_{id.fermions} = 0 \qquad\qquad (Pauli\ \ Principle) \\ \sigma_{non\ \ id.particles} = \dfrac{4\pi a^2}{1+k^2a^2} \end{cases} \tag{1.38}$$

The second equation results from the fact that identical fermions (f.e. a spin up-spin up pair) have symmetric spin-wavefunction and thus can only interact via a spatially antysimmetric wavefunction, the first one (lower in energy) being the p-wave configuration ($l = 1$). This requires for the two scattering particles an energy at least equal to the centrifugal barrier $\hbar^2/2\mu r^2$. For 6Li the maximum height of the p-wave barrier is 600 μK.

From equation 1.35 we get some interesting limits:

- $k|a| \ll 1$ and $k\ r_{eff} \lesssim 1$: f becomes independent of momentum and the entire physics - i.e. f - is described only by one parameter: $f = -a$. In this limit, within the Born approximation 1.29, the interaction can be described by a contact pseudopotential[8]

$$V(r) = g\ \delta^3(r) \tag{1.39}$$

with coupling constant

$$g = \frac{4\pi\hbar^2 a}{m} \tag{1.40}$$

Eq. 1.38 in this limit read as

$$\begin{cases} \sigma_{id.bosons} = 8\pi a^2 \\ \sigma_{id.fermions} = 0 \\ \sigma_{non\ \ id.particles} = 4\pi a^2 \end{cases} \tag{1.41}$$

Of course the latter equations can not hold in general, since a divergence in the scattering length would produce an unphysical divergence in the total scattering cross-section.

- $k|a| \gg 1$ and $k\ r_{eff} \ll 1$: this is called *unitary limit*. The scattering amplitude from equation 1.35 is now $f = \frac{i}{k}$. This situation occurs whenever a bound state is supported by V [15]. The resultant total scattering cross section for fermions from the third of eq. 1.38 is $\sigma_{tot} = \frac{4\pi}{k^2}$ which is the maximal possible for s-wave collisions.

[8] We are interested in contact potential since it can be shown [12] that the effect of any short ranged potential on the wavefunction can be modeled at low-energies as the one of an hard-core potential where the radius of the core is the scattering length a.

Bound states

The poles of the scattering amplitude determines the energy of the bound states of the interaction potential [16]. For $a > 0$ and $r_{eff} = 0$, eq. 1.35 admits a single pole, describing a molecule (dimer) with binding energy $E_b = -\hbar^2/(2\mu a^2)$. In general for a non zero r_{eff} the binding energy reads as $E_b = -\hbar^2/(2\mu a^{*2})$, with $a^* = 2R^*/(\sqrt{1 + 4R^*/a} - 1)$ and $R^* = -r_{eff}/2 > 0$.

Born approximation at higher orders

The form of eq. 1.22 is perfectly suited to perform perturbation theory and diagrammatic calculations. If we consider higher orders of equation 1.27, we find divergences yet at the second order. This is due to the unphysical nature of the delta potential which does not exhibit a characteristic scale, neither in real space or in momentum space: all physical potential must fall off over a certain distance. To overcome the problem, an explicit cut-off in momentum must be introduced. This can be done manually by simply impose the potential to be zero outside a certain region, or by proper renormalization of the coupling constant. Details on this procedure can be found in [6].

1.2.2 Feshbach resonances

An extremely useful tool available in ultra cold atoms experiments is the possibility to tune interactions through the so called Feshbach resonances, by simple means of a homogeneous magnetic field B. Interactions lay at the heart of the formation and dynamics of our degenerate gas. As discussed already, the magnitude of the scattering length a basically gives a measure of the strength of the interaction and its sign eventually indicates whether the interaction is repulsive ($a > 0$) or attractive ($a < 0$). Thus tuning the interaction means tuning the scattering length a.

Coupling between open and closed channels

A Feshbach resonance occurs in scattering processes between atoms in different internal hyperfine states, when the energy of a bound state in the interatomic potential is brought into resonance with the energy of the two colliding atoms. For the two colliding atoms interaction is mediated by some kind of potential which depend on their internal states: for alkali atoms (with one external electron per atom) it might be a triplet potential or a singlet one. Conservation of energy allows processes only into the so called "open channels" of scattering. Forbidden channels are referred to as "closed channels". In general different

internal atomic states are characterized by different interatomic potentials, as the different relative spin orientation of the valence electrons may change the nature of the interaction - for example from triplet to singlet. In particular, if the open and closed channels have different magnetic moments, their relative energy can be tuned by adjusting an external magnetic field, and, if bound states are supported by the potential of the closed channel, one of them can become degenerate (resonant) with the energy of the open channel (see figure 1.3). A coupling between open and closed channel arises, leading to second

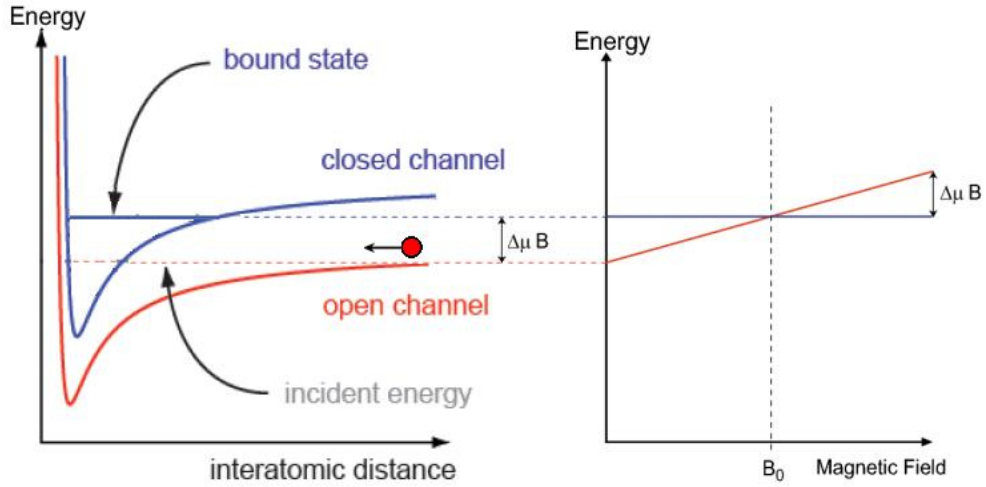

Figure 1.3: *Picture of scattering channels of colliding atoms. The energy of the continuum can be brought to resonance with a bound state of the potential of a close channel by tuning an external magnetic field.*

order processes where the closed channel may be temporarily occupied by the colliding atoms during the interaction processes, which eventually come back to the open channel when the interaction ends. The accounted phase shifts, which depends on the coupling between the channels, and eventually on the external magnetic field B, modifies the scattering length according to equation

$$a = a_{bg}\left(1 + \frac{\Delta B}{B - B_0}\right) \tag{1.42}$$

where a_{bg} is the background, i.e. the non resonant, scattering length independent on the magnetic field, ΔB is the width of the resonance and B_0 the value of the resonance. Because of the dependence on $1/(B - B_0)$, large changes in the scattering length can be produced by small variations in the magnetic field. A detailed derivation of this formula can be found in [15].

$|1\rangle$-$|2\rangle$ resonance in ^6Li

Accurate knowledge of the two body interaction potential is required to calculate the curve $a = a(B)$ for a certain atom. In the case of ^6Li one can refer to [17] [18]. All combinations of two of the three lowest hyperfine state of ^6Li, hereafter denoted as $|1\rangle$, $|2\rangle$ and $|3\rangle$, exhibit Feshbach resonances for magnetic field below 1000G. In our experiment we prepare our fermionic Lithium gas in the lowest hyperfine states which we address as $|1\rangle$ and $|2\rangle$. At low and high field they are identified by the following quantum numbers:

State	$B = 0$	High field $B > 100$ *Gauss*
$\|1\rangle$ =	$\|F = \frac{1}{2}; m_F = -\frac{1}{2}\rangle$	$\|m_I = +1 \ ; \ m_j = -\frac{1}{2}\rangle$
$\|2\rangle$ =	$\|F = \frac{1}{2}; m_F = +\frac{1}{2}\rangle$	$\|\mathrm{m}_I = 0 \ ; \ m_j = -\frac{1}{2}\rangle$

They exhibit a broad Feshbach resonance which according to equation 1.42 is described by the following parameters [19]:

B_0 **(G)**	ΔB **(G)**	a_{bg} (r_{Bohr})
≈ 832	≈ 262	≈ -1582

Referring to figure 1.4, we can distinguish two main behaviors: the right side –or BCS side- of the resonance where a is negative, and the left side –or BEC side- where a is positive. When a potential gives a state that is only weakly bound, a is large and positive, as the case of the molecular BEC side of the resonance, while a slightly shallower potential in which the state is not bound, produces a large and negative value of a. Then for a fermionic gas such as ^6Li, a large and negative scattering length may enable the observation of a BCS-like phase transition to a superfluid state: here in fact the Cooper condition of an arbitrary weak attractive interaction between fermions on top of a Fermi sea is fulfilled [6]. On the BEC side, due to three body processes three atoms collide, two bind together with energy $E_B = -\frac{\hbar^2}{ma^2}$, the third absorbs the released kinetic energy: Feshbach molecules are created. The closer to resonance on the left side, the less the molecules are bound, the more the fermionic nature of the atoms prevails. As we decrease the B field, the binding gets stronger and the atoms get closer: the molecules start to behave as bosons and, if the temperature is enough low, Bose-Einstein condensation occurs.

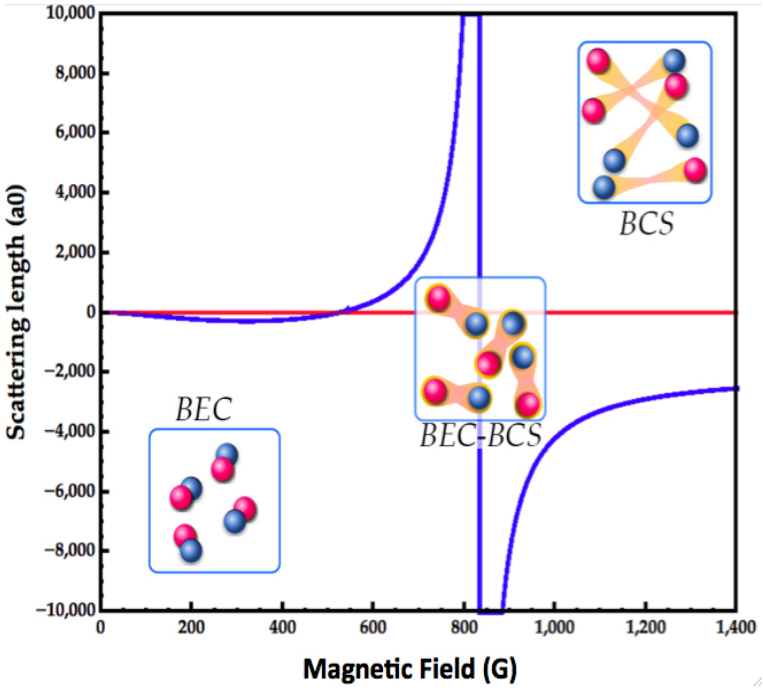

Figure 1.4: *Scattering Feshbach resonance between states* $|1\rangle$ *and* $|2\rangle$ *of* ^6Li *at* 832 *Gauss. A picture of the many body quantum states (BEC, BCS, crossover) that can be explored is presented. Their nature depend on the sign of* a.

1.3 Lithium 6

Why Lithium 6?

In the ultra-cold atom community, lithium is one of the most exploited atomic species involved in the realization of toy model of condensed matter physics within the quantum degenerate regime. It exists in both bosonic (^7Li) and fermionic (^6Li) stable isotopes, which are widely used to perform experiments respectively with BECs and quantum degenerate Fermi gases. The great interest of this species is due to the large number of Feschbach resonances among different hyperfine levels which are extremely broad compared to others alkali. This allows a fine tuning of the scattering length of the two body process across different regimes of interaction [20, 21]. In our case the presence of these broad resonances makes of ^6Li the ideal candidate for studies of both Fermi- and Bose-Hubbard models [22]. Furthermore, due to its small mass, Li has a larger photon-recoil energy compared to other alkali. This results in a larger tunneling rate and faster timescale for super-exchange processes, and allows easier access to spin dominated regimes [23].

1.3.1 Atomic structure of ^6Li

Among alkali elements, ^6Li is one of the only two stable isotope -the other one being ^{40}K. It has configuration $[He]2s^1$ and atomic weight 6.015 u= $9.988\times10^{-27}Kg$ with three neutrons and atomic number Z=3 (N=6 nucleons). Having just one s-electron in the outer shell, determines its total electronic spin $|\vec{S}| = \frac{1}{2}$. The fine interaction due to spin-orbit coupling writes as $\sim \vec{L}\cdot\vec{S} = J^2 - L^2 - S^2$ with the proper constant of proportionality, where the electronic angular momentum $\vec{J} = \vec{L} + \vec{S}$ has been introduced. The *nuclear angular momentum* (or *nuclear spin*) is $|\vec{I}|$=1 and thus the atom experiences *hyperfine interaction* between the associated nuclear magnetic moment[9] and the magnetic field created by the surroundings electrons. This interaction writes as

$$H_{HF} \sim \vec{I}\cdot\vec{J} \tag{1.43}$$

This interaction breaks the degeneracy on the m_j and gives origin to a hyperfine structure. The vector $\vec{F} = \vec{I} + \vec{L} + \vec{S} = \vec{I} + \vec{J}$ is used to classify the associated hyperfine states: in fact the energy operator 1.43 is diagonal in the basis

[9] If a charged particle posses an angular momentum $\vec{I}$ the g-factor is the constant of proportionality between $\vec{I}$ and a magnetic dipole moment (μ) naturally associated with $\vec{I}$.

$$\vec{\mu} = g_I\vec{I}$$

and g_I has the sign of the electric charge.

$|$L,S,J,I;F;M$_F\rangle$ and the energy splitting can be calculated as [24]

$$\Delta H_{HF} = \frac{1}{2} A_{level} \Big(F(F+1) - I(I+1) - J(J+1) \Big) \tag{1.44}$$

where the constant A depends on the atomic level. Useful values of A for ground and first excited state from ref. [25], are reported in tab.1.

Associated atomic level	Value [MHz]
$A_{2^2S_{1/2}}$	152.1368407
$A_{2^2P_{1/2}}$	17.386
$A_{2^2P_{3/2}}$	-1.155

Table 1: Hyperfine constants of the atomic levels of ^6Li.

We report in figure 1.5 a schematic and yet useful scheme of the atomic level to picture the situation.

Ground state and first excited

In the **ground state** configuration $1s^2 2s^1$ the electronic angular momentum is $|\vec{L}| = 0$: spin orbit interaction is zero. Here $\vec{J} = \vec{S}$ and thus from elementary addition of angular momentum, the quantum number F can only takes values in integral steps in the range:

$$|J - I| \leqslant F \leqslant J + I \tag{1.45}$$

which in this case means $F = 1/2,\ 3/2$.

- $F = \frac{1}{2}$
  Hyperfine splitting from equation 1.44 -using the appropriate value from table - results $\Delta H_{HF} \simeq -152\ MHz$.
- $F = \frac{3}{2}$
  In the same way one get $\Delta H_{HF} \simeq 76.068\ MHz$.

The distance in energy between this two states then results $\Delta E(F = 3/2 \leftrightarrow F = 1/2)$=228 MHz. The same procedure can be extend to other levels[10]. The half integer values of F are fingerprint of the fermionic character of ^6Li.

In the **excited state** configuration $1s^2 2p^1$ the total electronic angular momentum is $|\vec{L}| = 1$. Thus, in addition to hyperfine interaction, *spin-orbit interaction*

[10] For the $2^2P_{3/2}$, quadrupole interaction should also be taken into account [26].

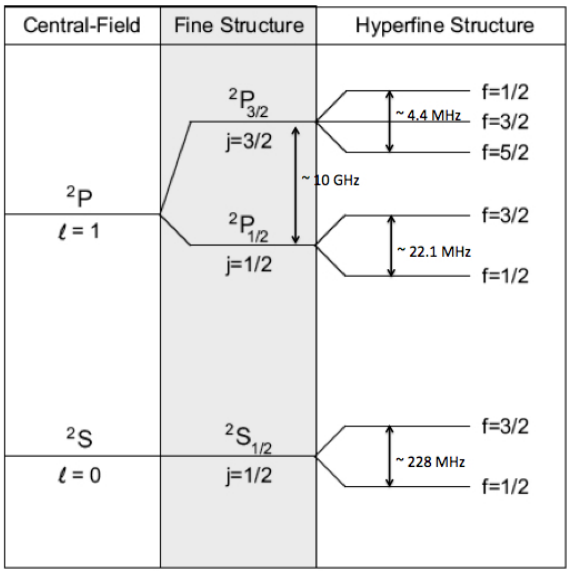

Figure 1.5: *Atomic levels of fermionic Lithium in a region of space where no external fields are present. Levels are classified with quantum numbers L,J and F. Energy splittings are not at scale. Figure taken from [26].*

is now present due to the coupling between the magnetic dipole moment arising from electronic spin and the angular momentum [11]. It has the usual form

$$H_{SO} \simeq \vec{L} \cdot \vec{S} = \frac{1}{2}\Big(J^2 - L^2 - S^2\Big) \tag{1.46}$$

When we include also the hyperfine interaction 1.43 we can distinguish two cases: J=1/2, for which $\vec{F}$ can assume the same values of the ground state; J=3/2, for which F=-5/2, -3/2, -1/2,1/2, 3/2, 5/2 are all possible states. The transition lines between the ground state level L=0 and the excited fine-splitted sub-levels L=1 are referred to as D1 and D2 lines, being D1 ($2^2S_{1/2} \leftrightarrow 2^2P_{1/2}$)=670.992 421 nm and D2 ($2^2S_{1/2} \leftrightarrow 2^2P_{3/2}$)=670.977 338 nm. The fine structure energy splitting of the excited state is found to be $\Delta E_{FS} = 10.053\ 044\ GHz$ [27].

External magnetic fields: Zeeman shift

If atoms are put in a non zero magnetic field region, energy splitting of the hyperfine levels into a total of (2S + 1) (2I + 1) = 4I + 2 states occurs. In the presence of a static $\vec{B}$ field the interaction energy is given by:

$$\Delta E = -\vec{\mu} \cdot \vec{B} \tag{1.47}$$

[11] In general the interaction between two angular momenta is due to the gyromagnetic ratios (g-factor or g). Two angular momenta will produce two dipole moments which interact with each other.

where the atom's total magnetic moment has two distinct contributions from the electrons and the nucleus: $\vec{\mu}_F = \vec{\mu}_J + \vec{\mu}_I$[12]. The Zeeman Hamiltonian for an alkali atom in a static external magnetic field B is obtained by minimal substitution of the momentum operator. Neglecting the diamagnetic term the part of the Hamiltonian including the B-dependent terms can be written as

$$\begin{aligned}\hat{H}_{tot} &= \hat{H}_0 + \hat{H}_{SO} + \hat{H}_{HF} + \hat{H}_{Zeeman}(B) = \\ &= -\frac{\hbar^2}{2m_e}\nabla^2 + V(\vec{r}) + \underbrace{\xi(\vec{r})\vec{L}\cdot\vec{S}}_{Spin-Orbt} + \underbrace{\zeta(\vec{r})\vec{I}\cdot\vec{J}}_{Hyperfine} + \hat{H}_{Zeeman}(B)\end{aligned} \tag{1.48}$$

Referring the energies to the fine structure levels, the interesting part of the hamiltonian is

$$\hat{H}_{HF} + \hat{H}_{Zeeman} = \zeta(\vec{r})\vec{I}\cdot\vec{J} + \hat{H}_{Zeeman}(B) \tag{1.49}$$

The quantization axis is chosen along the z-direction. For **low fields** ($\ll 10^2 G$ for the case of ^{6}Li which is a very light atom) $\hat{H}_{Zeeman} \ll \hat{H}_{HF}$, and its effect can then be considered as a perturbation to the hyperfine atomic structure (*anomalous Zeeman effect*). Interaction between $\vec{I}$ and $\vec{J}$ is yet strong and thus F remains a quite good quantum number to distinguish the atomic levels, despite their energy splitting follow the m_F component as

$$\Delta E_{Zeeman} = \frac{\mu_B}{\hbar} g_F m_F B \tag{1.50}$$

where the *Landè factor* g_F associated to each hyperfine level is mixing g_J with g_I as $g_F = g_J \frac{F(F+1)-I(I+1)+J(J+1)}{2F(F+1)} + g_I \frac{F(F+1)+I(I+1)-J(J+1)}{2F(F+1)}$, $\mu_B \sim 1.4 MHz/G$ the Bohr magneton and $B = |\vec{B}|$. Properly speaking F is no longer a good quantum number and is substituted by M_F. States with same value of M_F are now mixed[13]. The values of electronic and nuclear g-factors from [25] are reporter in the following table

[12] $|\vec{\mu}_I| \propto \mu_N = \frac{e\hbar}{2m_p}$ and $|\vec{\mu}_J| \propto \mu_B = \frac{e\hbar}{2m_e} = \mu_N \times N \cdot 2000$, N being the number of nucleons. Thus the nuclear contribution $\vec{\mu}_I$ is much smaller then the electronic one $\vec{\mu}_J$ and it can often be neglected.

[13] The elements of matrix of the Zeeman hamiltonian in 1.49 can be computed in the diagonal basis of quantum numbers $|L, S, J, I; F; M_F>$ which can be obtained from the basis $|L, S, J, M_J, I, M_I>$ by means of Clebsh-Gordan coefficients as

$$\begin{aligned}&|I, J, F, M_F> = \\ &= \sum_{M_I + M_J = M_F} |I, M_I, J, M_J>< I, M_I, J, M_J | I, J, F, M_F>\end{aligned}$$

where we omitted for simplicity the quantum numbers L and S.

g-factors	Value
g_I	-0.000 447 654 0
$g_J(2^2S_{1/2})$	2.002 301 0
$g_J(2^2P_{1/2})$	0.666 8
$g_J(2^2P_{3/2})$	1.335

The atomic scheme of the levels in presence of an external magnetic field is reported in figure 1.6.

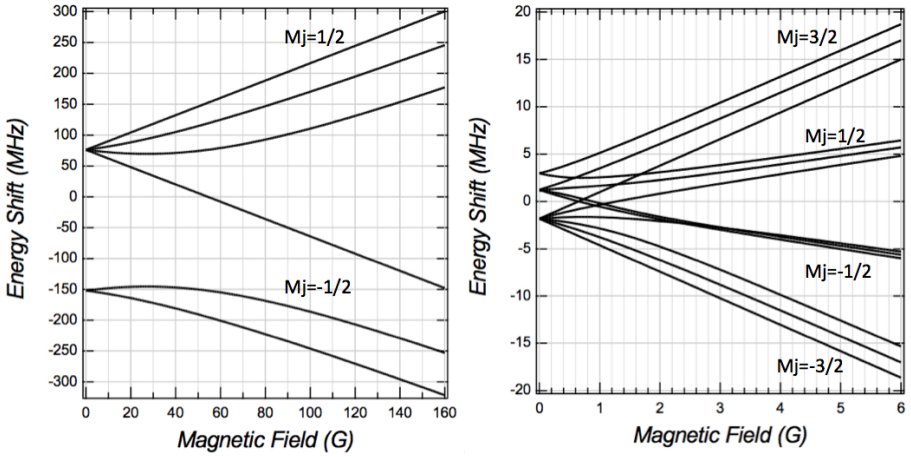

Figure 1.6: *Energy splitting due to external magnetic field induced Zeeman shift for ground state level $2^2S_{1/2}$ (left) and excited level $2^2P_{3/2}$ (right). Note that the scales of the two figures are different: due to very low hyperfine splitting of the excited state level ($\sim 5MHz$), the Paschen-Bach regime is entered for small magnetic field ($B \approx 3Gauss$), while for the ground state level it starts at $B \approx 100Gauss$. Figure taken from [26].*

As it can be seen in fig. 1.6, both ground and excited states enter the intermediate **Paschen-Bach regime** at relatively small values of the magnetic field: about 2 Gauss for excited state and 100 Gauss for ground state. Zeeman shift can no longer be considered as a perturbation to the hyperfine structure. J and I are basically decoupled and their separate magnetic interaction 1.47 with B become dominant over the Hyperfine one. The energy splitting is thus given by:

$$\Delta E_{Zeeman} = \frac{\mu_B}{\hbar}(g_J m_J + g_I m_I)B \tag{1.51}$$

Usually the second term can be neglected being $g_I \ll g_J$.
Subsequent quantization of space imposes *selection rules* for transitions in dipole

approximation which are given by:

$$\Delta l = \pm 1 \quad \Delta j = 0, \pm 1 \ (no\ 0 \leftrightarrow 0) \quad \Delta m_j = 0, \pm 1 \tag{1.52}$$

where

$$Observation\ (\hat{k})\ \perp\ B: \begin{cases} \Delta m_j = \pm 1 \quad lin.\ polar. \perp B\ (\sigma\ lines) \\ \Delta m_j = 0 \quad lin.\ polar. \parallel B\ (\pi\ line) \end{cases} \tag{1.53}$$

and

$$Observation\ (\hat{k})\ \parallel\ B: \begin{cases} \Delta m_j = \pm 1 \quad circular\ polarization \\ \Delta m_j = 0 \quad forbidden \end{cases} \tag{1.54}$$

1.4 Cooling and trapping atoms with laser light

Basic concepts

The principle of cooling matter with laser light is based on the transfer of momentum involved in a scattering process due to absorption/emission of a photon by one atom. We imagine the atom as a two level system at rest in the ground state. When a photon of wave vector $\vec{k}_{ph}$ is absorbed by the atom, its momentum ($\hbar\vec{k}_{ph}$) is acquired by the two level system which recoils with an energy of

$$E_{rec} = \frac{\hbar^2 k_{ph}^2}{2M_{at}} \tag{1.55}$$

and the photon's energy is used by the atom to get excited in the upper level. After a typical time $\tau = 1/\Gamma$, Γ being the natural width of the excited state, the atom will spontaneously emit a photon falling back into the ground state, this time losing the same amount of momentum gained with photon absorption. The fundamental difference between the two processes is that while spontaneous emission is a directionally random process, absorption is not. The immediate consequence of it, is that averaging on a great numbers of absorption-emission processes, the transfer of momentum due to spontaneous emissions will average zero, while the one due to absorption will not[14]. The atom will then experience a macroscopic force in the direction of the radiation. The change in velocity in a single absorption-emission cycle is $\delta v = \hbar k_{ph}/M_{at}$ and its order of magnitude is mm/s. Using D_2 line transition $\delta v \sim 100 mm/s$ for ${}^6Li$ and $\sim 5.9 mm/s$ for ${}^{87}Rb$, because of its greater mass. Atomic clouds are created by evaporation of a heated reservoir. At this point the speed of a Li atom is about 1000m/s

[14]Here we are completely neglecting the effect of stimulated emission: this is a good approximation provided that Γ is not too small.

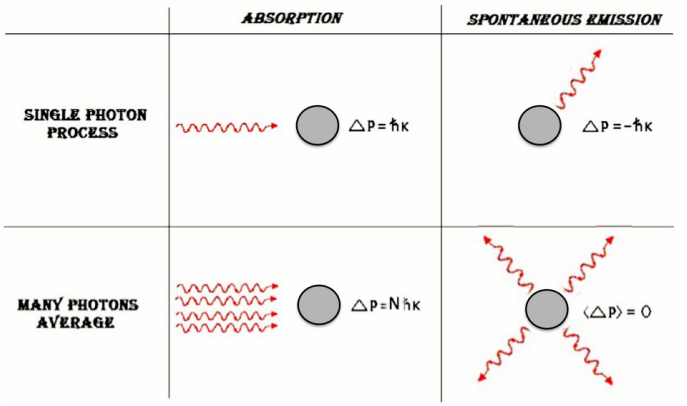

Figure 1.7: *Basic principle of laser cooling technique is to transfer momentum from radiation to atoms so that in a great number of absorption-emission cycles, atoms will exchange a net negative momentum with photons. In figure we have sketched the situation for an atom at rest (v=0): radiation is here resonant with a two level atomic transition.*

fast so that the number of photons the single atom should absorb to decrease significantly its speed is about $N = 1000(m/s)/\delta v \sim 10^4$.
Thus, the most basic principle behind the use of coherent radiation for cooling techniques is that when a photon is scattered by an atom, the change in its translational energy - and thus in momentum - results in a net mean force acting on it. This idea can be explored and developed in many contests which we will describe in some more details in the following paragraphs.

1.4.1 Photon-atom interaction

Let us consider the effect of a laser light characterized by frequency $\omega/(2\pi)$ and wavevector $\vec{k}$, on a free atom moving with a certain velocity ($\vec{v}$). We are interested in calculating the number of photons scattered (N_{ph}) by the atom in the unit of time (Δt). Indeed the radiative pressure force can be written as

$$\vec{F} = \hbar\vec{k}\frac{N_{ph}}{\Delta t} \tag{1.56}$$

where $\hbar\vec{k}$ is the single photon momentum. This force is proportional to the rate of scattering events and even if inappreciable at macroscopic level, nonetheless became extremely relevant when acting on an atomic cloud. If the frequency of the laser is close to be resonant with an atomic transition, the atom can be

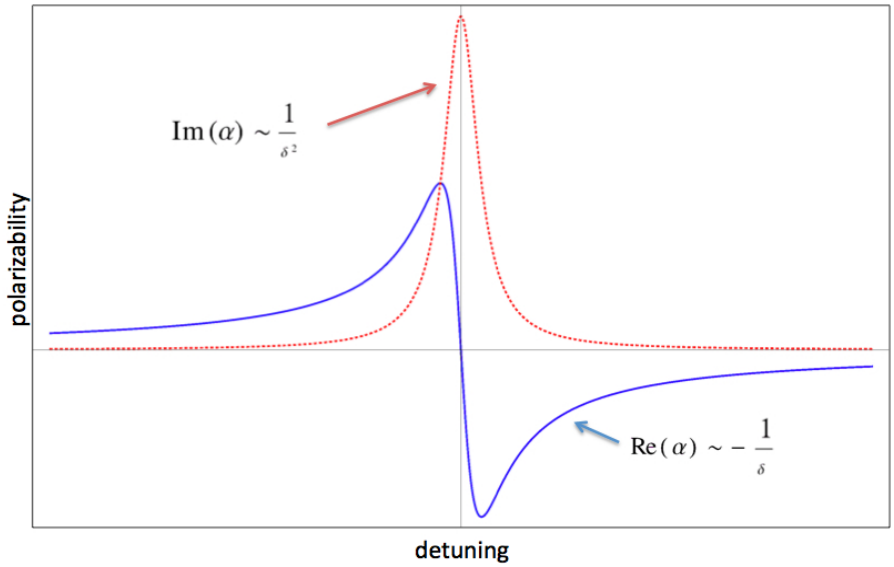

Figure 1.8: *Real and imaginary part of the polarizability. The imaginary part can be linked to a quasi-resonant interaction: it is responsible for absorption of photons as already described in 1.4.1 and causes dissipation of energy. The real part instead has a typical dispersive behavior: it can be associated to a conservative force and can be used to implement optical traps or optical lattices.*

approximated as a closed two level system[15] [28]. The quantity $\delta_0 = \omega - \omega_0$ is known as the *detuning* of the laser frequency from the natural atomic transition ω_0[16]. Each event of scattering is associated with an absorption-emission cycle. Atoms must populate the excited state in order to be scattered. Thus the ratio $\frac{N_{ph}}{\Delta t}$ can be expressed as the product between the average population of the excited state due to the strength of laser-atom interaction, and the inverse of the typical time after which it comes back to the ground state, which by definition is the natural width Γ. A basic theory of photon-atom interaction makes use of the dipole hamiltonian

$$H_{AL} = -\vec{d} \cdot \vec{E}(t) \tag{1.57}$$

where d is the *atomic electric dipole*. When an electric field is acting on an atom, an electric dipole $\vec{d}$ is induced. The latter can be written in term of the atomic polarizability α as $\vec{d} = \alpha \vec{E}$. Classically we can think to the induced electric dipole as due to the displacement of the electrons from their equilibrium position, while quanto-mechanically it is due to mixing of orbitals with different spatial charge distribution. Within the density matrix formalism [29] the polarizability has the form:

$$\alpha = -\frac{e^2 \mu_{eg}^2}{\hbar} \frac{\delta - i\frac{\Gamma}{2}}{\delta^2 + \frac{\Gamma^2}{4} + \frac{|\Omega|^2}{2}} \tag{1.58}$$

where $\vec{\mu}_{eg}$ is the *transition dipole moment*, $\Omega =: e\frac{\vec{\mu}_{eg} \cdot \vec{E}_0}{\hbar}$ is the *Rabi frequency* and $E = \frac{E_0}{2} e^{-i\omega t} + h.c.$. Even if oscillating at the same frequency of E, the complex nature of α accounts for dephasing due to the induced dipole moment with respect to the driving field.

Dipole force: If we just consider the real part of α we see that for $\delta \gg \Gamma, \Omega$ $H \simeq \alpha E^2 \simeq \frac{I(\vec{r})}{\delta}$. Depending on the sign of the detuning, the real part of α can flip the sign of d with respect to E, causing local maxima ($\delta < 0$) or minima ($\delta > 0$) of the energy. This results in a trapping or in an anti-trapping potential for the atoms. The explicit expression of the force is given by the gradient of the dipole potential, which in analogy with classic physics can be written as [29]:

$$U_{dip} = -\frac{1}{2}\langle \vec{d} \cdot \vec{E} \rangle = -\frac{1}{2\epsilon_0 c} Re(\alpha) I(\vec{r}) \simeq \frac{3\pi c^2}{2\hbar\omega_0^3} \Big(\frac{\Gamma}{\delta}\Big) I \tag{1.59}$$

where the average is intended over fast oscillations and $I(\vec{r}) = \epsilon_0 c |E(\vec{r})|^2/2$. In the last passage we have taken the detuning $\delta >> \Gamma, \Omega$. Only the $Re(\alpha)$,

[15] If the transition is not closed a repumper must be add to close the loop of the transition cycle (see next chapter).

[16] We will refer to δ_0 and $\delta = \delta_0 - \vec{k} \cdot \vec{v}$ respectively as the detuning for an atom at rest (v=0) and for a moving atom.

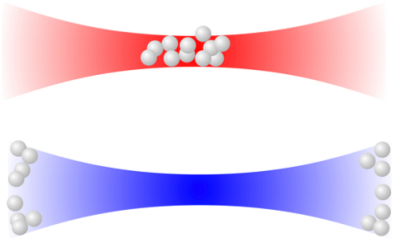

Figure 1.9: *Depending on the sign of the detuning with respect to the atomic transition, is common use to distingue between red and blue traps, meaning trapping and anti-trapping potentials.*

describing in phase oscillations of the dipole moment (coherent processes) with the electric field, intervenes in the potential. Thus the resulting conservative force is,

$$F_{dip}(\vec{r}) = \frac{1}{2\epsilon_0 c} Re(\alpha) \vec{\nabla} I(\vec{r}) \tag{1.60}$$

and vanishes for uniform intensities. At this point it is clear that a focussed beam with gaussian shaped intensity profile will trap or expel atoms from its focus depending on the sign of the detuning with respect to the atomic transitions (see fig.1.9). This is the basic principle on which optical traps work.

Radiative force: The imaginary part $Im(\alpha)$ of alpha accounts for the dephasing (Incoherent processes) of the dipole moment and the field. In the classical picture, the power transferred to the light field by a charged oscillator is $\langle \dot{\mathbf{p}}\mathbf{E} \rangle$ which results in a scattering rate of photons

$$\Gamma_{scattering}(\vec{r}) = \frac{\langle \dot{\mathbf{p}}\mathbf{E} \rangle}{\hbar\omega} = \frac{1}{\hbar\epsilon c} Im(\alpha) I(\vec{r}) \tag{1.61}$$

which are spontaneously emitted in the laser field. Thus the radiative force of eq.1.56 can be written in the form:

$$\vec{F} = \hbar\vec{k}\frac{\Gamma}{2}\frac{\frac{|\Omega|^2}{2}}{\delta^2 + \frac{\Gamma^2}{4} + \frac{|\Omega|^2}{2}} = \hbar\vec{k}\frac{\Gamma}{2}\frac{s}{1+s}\frac{1}{1+\left(\frac{2\delta}{\Gamma_s}\right)^2} \tag{1.62}$$

with

$$\begin{cases} s = \dfrac{I}{I_s} = \dfrac{2|\Omega|^2}{\Gamma^2} & \textit{Saturation Parameter} \\ \Gamma_s = \Gamma\sqrt{1+s} & \textit{Power Broadened Linewidth} \end{cases}$$

which describes a Lorentzian function with linewidth Γ_s dependent from the intensity of the radiation through $|\Omega|^2$.

The maximum[17] $F_{max} = \hbar k\Gamma/2$ of the force is obtained for zero detuning (resonance) when the radiation intensity saturates the transition (s$\rightarrow \infty$) i.e., for a moving atom, when the Doppler effect due to atomic motion compensates the difference between the radiation (ω) and natural transition frequency (ω_0), i.e. when

$$\delta = \omega - \omega_0 - \vec{k} \cdot \vec{v} = 0 \qquad (Resonance\ Condition). \tag{1.63}$$

Optical Molasses

A clever way to employ the radiative force is that to combine two red detuned counter-propagating laser beams with same angular frequency ω, to create what are commonly known as *optical molasses*. We will now see how the radiation pressure gives the light the property to behave as a viscous fluid with respect to moving atoms. To have a better picture of it, imagine to have an atom moving on the same axis of the two beams with velocity $\vec{v}$. Due to Doppler effect, in the atom reference frame, the effective frequency of the counter-propagating photons will be upshifted to $\omega' = \omega(1 + \frac{v}{c})$, while the effective frequency of the photons co-propagating will be down shifted to $\omega'' = \omega(1 - \frac{v}{c})$. Because

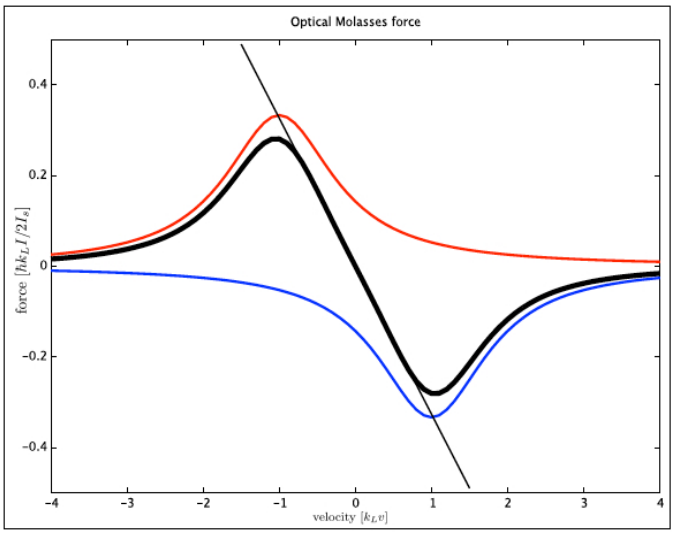

Figure 1.10: *The red and blue curves represents the forces due to single beams, while the black one is the sum of the two. Figure taken from [30].*

the beams are both red detuned, one of these frequency will get closer to be resonant with the atomic transition while the other will do the opposite. Thus

[17] The saturation value of the force is given by the the recoil momentum due to single photon scattering, multiplied for the maximum absorption rate of photon $\Gamma/2$ and thus is limited only by the lifetime of the excited state $\frac{1}{\Gamma}$.

the probability of absorbing a photon will be higher for those photons with $\vec{k}$ opposite to $\vec{v}$, and the atoms will be slowed, no matter their versus of motion along the axis.

Quantitatively, we get two opposite contributions of the same kind of equation 1.62 which, taken into account the correct Doppler shift, reads as

$$\begin{aligned}\vec{F}_{tot} =&\hbar\vec{k}\frac{\Gamma}{2}\Big[\frac{I/I_s}{1+\frac{I}{I_s}+(2(\delta_0-kv)/\Gamma)^2}-\frac{I/I_s}{1+\frac{I}{I_s}+(2(\delta_0+kv)/\Gamma)^2}\Big]\approx\\ \approx&\,\hbar\vec{k}\frac{\Gamma}{2}\Big[\frac{I/I_s}{1+(2(\delta_0-kv)/\Gamma)^2}-\frac{I/I_s}{1+(2(\delta_0+kv)/\Gamma)^2}\Big]\end{aligned} \tag{1.64}$$

where we have taken for simplicity the small intensity limit $I/I_{sat} << 1$. A small velocity $|kv| << \Gamma, \delta_0$ expansion of the equation above yields the viscous-like result for the force:

$$\vec{F}_{tot} = -\alpha\ \vec{v} + O(v^3) \tag{1.65}$$

with the damping coefficient ($\delta_0 < 0$):

$$\alpha = 4\hbar k^2 \frac{I}{I_s}\frac{2|\delta_0|/\Gamma}{(1+(2\delta_0/\Gamma)^2)^2} \tag{1.66}$$

Limits of laser cooling

We might be interested in addressing the smallest temperature possible with this method of cooling. Low temperature for a classical gas means that the velocity of the atoms follows a Maxwell-Boltzmann distribution with a very small width. Since for a moving atom the radiative force depends on its velocity through the detuning due to Doppler effect, variations of δ from the resonance condition eq. 1.63 must be compensated in the slowing process in order to keep the light resonant with the atoms. The engine that solves this problem is described in paragraph 2.10.

In a radiative pressure cooling process, spontaneous emission induces atoms to perform a random walk of step $\hbar k_{ph}$ in momentum space after each random emission. This process can be described with a diffusion equation for the momentum:

$$\frac{d\mathbf{p^2}}{dt} = -2\gamma\mathbf{p^2} + 2D_p \tag{1.67}$$

where γ is the viscous coefficient of the molasses and D_p its diffusion coefficient. The subsequent heating mechanism competes with the cooling one since equilibrium is reached when $\frac{\mathbf{p^2}}{2m} = \frac{D_p}{2m\gamma}$. A temperature can be associated through an analogy with the Maxwell-Boltzmann distribution where $\mathbf{p^2}/(2m) = (3/2)\ k_BT$. Using the diffusion coefficient for a 3D molasses [31] one finds:

$$K_BT = \frac{\hbar\Gamma}{4}\frac{1+(2\delta_0/\Gamma)^2}{2|\delta_0|/\Gamma} \tag{1.68}$$

which for $\delta_0 = \frac{\Gamma}{2}$ gives a relative minimum for the temperature called *Doppler temperature*

$$T_D = \frac{\hbar\ \Gamma}{2K_B} \tag{1.69}$$

and for ^6Li it's of the order of $140\mu K$. Eventually, this temperature becomes extremely low in case of cooling on narrow lines [32]. Furthermore, since the exchange of momentum between photon and atom is discrete, the smallest indetermination on the velocity is given by the recoil limit of single photon emission process. The best way to visualize it, is to look at the radiation laser field as a thermal bath at very low temperature[18]. Atoms in the bath cannot have, in any case, energy lower then the photons energy, stated that in each spontaneous emission they acquire a random momentum $\hbar k_{ph}$ that heats up the cloud. Then the absolute minimum for the temperature, called *recoil temperature*, is defined as

$$T_{rec} = \frac{E_{rec}}{k_B} \tag{1.70}$$

This temperature is usually of the order of $1\mu K$ and depends on the laser wavelength.

It is worth to observe that the semiclassical description done so far for interaction processes between atoms and laser radiation has some limits. So far we considered the atom as a point like particle with precise values of position and velocity. This is clearly an approximation since the atom has itself a quantum behavior. Nevertheless it can be used for simplicity as long as the extension of the wave packet associated to the atom remains much smaller of the wavelength of the radiation and the uncertainty on the velocity is such that the Doppler broadening is much smaller then the natural width of the resonance.

But when the temperature approaches the recoil temperature, the de Broglie wavelength of the atom become of the same order of magnitude of the wavelength of the radiation, and both matter and light start to behave as pure quantum systems. The semi-classical approximation eventually falls.

1.4.2 The Magneto-Optical Trap (MOT)

To perform experiments on our gas we need a trapping technique which can keep our cold atom cloud localized in the space for a reasonable amount of time. Unfortunately the optical molasses does not provide a spatial confinement for the atoms: after a certain time in the molasses they will inevitably escape from it. In 1986 J.Dalibard used an inhomogeneous magnetic field to produce a trapping

[18] This is reasonable if one thinks to the coherence properties of a laser beam.

force toward a well defined trapping center.
The basic ingredients of a magneto-optic-trap (MOT) are a quadrupole magnetic field created by a pair of coils in anti-Helmoltz configuration (see fig. 1.11), and three pairs of counter propagating red-detuned laser beams intersecting orthogonally in the region of zero magnetic field. In addition, beams having opposite directions, must have opposite circular polarization. Due to Zeeman shift of the atomic levels, the inhomogeneous magnetic field ensure the establishing of a trapping harmonic-like force. The total field is the sum of the two independent fields generate by the two coils (fig. 1.11) and near the center of the trap is given by $\vec{B}(z) = (b \cdot z)\hat{z}$.

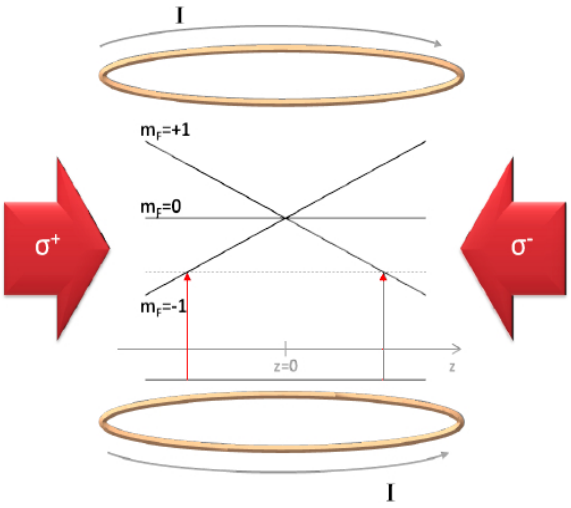

Figure 1.11: *Configuration of the beams and magnetic field coils necessary to produce a MOT.*

To benefit in clearness we will consider the simple case of an atom with ground state J_g=0 and excited state J_e=1. Zeeman shift will split the excited state into the three manifolds m_e=-1,0,1 as reported in figure 1.11. Due to selection rule, deriving from the conservation of the projection J_z of total angular momentum along z axis, the σ^- polarized beam coming from one side can induce only transitions to the m_e=-1, while the σ^+, coming from the opposite direction, will induce those to m_e=+1. If the beams are both red detuned with respect to the atomic transition, due to Zeeman shift, an atom in z>0 will interact much more with the beam coming from the right side of the trap, inducing a $m_g = 0 \rightarrow m_e = -1$ transition and the symmetric thing will happen in the position z<0 where the $m_g = 0 \rightarrow m_e = 1$ transition will be preferentially induced

by the left coming beam. The result is that an atom at near the center at $z \neq 0$ will be pushed back to the center of the trap. In this kind of trap, atoms are then both trapped and cooled with the same mechanism of the optical molasses.

The effective force acting on the atoms has the same form of eq. 1.62 where now also Zeeman shift [19] must be included in the detuning by replacing $kv \rightarrow kv + \frac{\mu' bz}{\hbar}$. In the limit $k\nu,\ \Delta E/\hbar \ll \delta_0$ this force can be reduced to the form:

$$\vec{F}_{tot} = -\alpha\vec{v} - Kz \qquad with \qquad K = \frac{\mu' B}{\hbar k}\alpha \tag{1.71}$$

This is the differential equation of a damped harmonic oscillator, the K-constant being proportional to the gradient of the magnetic field. A capture range and velocity can be defined as functions of the parameters of the trap ($\delta_0,\ B,\ \mu'$). An interesting study on the capture range can be found in [30]. Thus equation 1.71 demonstrates that the described configuration of laser beams and magnetic field is able to produce both a viscous and a spatial dependent spring-like force around the center of the trap, thus providing both trapping (typical density values are $10^{10} - 10^{12}\ cm^{-3}$) and cooling for the atoms. Thus is able to compress the phase-space density of the cloud.

Optical dipole trap

The conservative part of the force of eq. 1.60 is widely used to confine atoms into *optical dipole traps*. In the limit $\delta \gg \Gamma, \Omega$ and far from resonance, it can be approximated using $\Omega^2 = \frac{\Gamma^2 I}{2I_s} = \frac{6\pi}{\hbar c k^2}$ as [33]:

$$F_{dip} \simeq -\frac{3\pi}{2ck^3}\frac{\Gamma}{\delta}\nabla I \tag{1.72}$$

By comparison between dipole force (conservative) and radiative force of eq. 1.62 (dissipative) the following things can be noted:

- they are respectively proportional to the real and imaginary part of the polarizability. They are linked to each other by the Kramers-Kronig relation and thus dispersion cannot occur without absorption.
- they depend respectively on the detuning as $\sim \frac{1}{\delta}$ and $\sim \frac{1}{\delta^2}$: moving out of resonance the contribution of the dispersive dipole force becomes dominant over the dissipative one.
- due to the dependence of 1.72 on the ratio $\frac{I}{\delta}$, a change in detuning can be compensated with a change in the intensity.

[19] The Zeeman energy shift is given by $\Delta E = \mu' Bz$ with $\mu' = \mu_B g_{F'} m_{F'}$, $g_{F'}$ being the Landè factor of the atomic level.

Focussed red-detuned gaussian beams are the easiest choice for optically trapping atoms. A single focussed beam has transversal intensity profile

$$I(\rho, z) = \frac{2P}{\pi W(z)^2} e^{-\frac{2\rho^2}{W(z)^2}} \tag{1.73}$$

where P is the laser power, $W(z) = w^2(1 + z^2/z_R^2)$ contains the Rayleigh range $z_R = \pi w^2/\lambda$ ($W(z_R) = w\sqrt{2}$) and the beam waist w[20], while ρ and z are respectively the radial and axial distances from the focus. Near the focus the trap profile can be well approximated with a harmonic shape $V_{HO}(\rho, z) = \frac{1}{2}(\omega_\rho^2 \rho^2 + \omega_z^2 z^2)$, the trapping frequencies being

$$\frac{\omega_\rho}{2\pi} = \sqrt{\frac{2P}{\pi^3 m w^4}} \tag{1.74}$$

$$\frac{\omega_z}{2\pi} = \frac{\omega_\rho}{2\pi} \frac{w}{z_R} \tag{1.75}$$

and the aspect ratio $\lambda = \frac{\omega_\rho}{\omega_z} = z_R/w$. The latter quantity gives a measure of the ellipticity of the trap.

Evaporative cooling

Due to the intrinsic recoil limit 1.70 of laser based cooling techniques, a last stage of cooling is usually required to achieve quantum degeneracy or Bose Einstein condensation at the experimentally achievable densities. The idea of evaporative cooling is to selectively eliminate from a trapped gas the particles having an energy higher than the average energy of the system. In this way the remaining particles are cooled. To implement this idea on an optical trap, the intensity of the light can be decreased in time so that the depth of the trap is reduced and the hottest particles, which are more likely to populate the higher levels of the trap, will escape it. In other words, the particles of our thermal gas will be Maxwell-Boltzmann distributed. The selective remotion of hottest particles is obtained by means of cutting the wings of the distribution. The resultant out-of-equilibrium condition of the gas, will thermalize through elastic collisions among particles and will find a new equilibrium Maxwell-Boltzmann distribution with smaller width: the resultant temperature is lower. Usually a constant step decreasing ramp of the trapping laser intensity is implemented to run evaporative cooling. Furthermore the elastic collision rate must be large with respect to the time between two successive step of the ramp so to allow thermalization, i.e. redistribution of the energy, after each cut of the wings. This technique is much more difficult to implement for fermions with respect to bosons, due to Pauli suppression of elastic collisions at low temperature. As we

[20] Defined as the radius where the intensity drops of $1/e^2$.

discussed within 1.2.1, the elastic scattering cross section for identical fermions in normal conditions is zero. Mixtures of fermions in different atomic levels must be used in order to allow interparticle collisions to happen and thermalization to be possible.

Chapter 2

Experimental Setup and Procedure

In this chapter we present the optical setup used for cooling and trapping of ^6Li. We also introduce our high field imaging scheme allowing atoms detection across different regimes of interaction. The cooling scheme is described in the first part of the chapter. The middle part is dedicated to the imaging, while in the last part we describe both the Zeeman slower and the magnetic coils that produce the Feshbach and curvature fields.

2.1 Optical scheme for cooling

In our experiment, in addition to the widely used D2 ($2^2S_{1/2} \leftrightarrow 2^2P_{3/2}$) cooling transition (see figure 2.2), we also developed a cooling procedure on the D1 line ($2^2S_{1/2} \leftrightarrow 2^2P_{1/2}$) following the method recently demonstrated in [34] on ^7Li. Details on the D1, exception made for the lock-in scheme which we will present here, can be found in the next chapter. The D1 molasses allows us to achieve a temperature of $\sim\ 40\mu K$, more than 3 times smaller than the Doppler limit. We report in tab. 2.1 the characteristics of these two lines.

Property	D1 line	D2 line
wavelength (λ)	670.979 421 nm	670.977 338 nm
frequency (ν)	446.789 634 THz	446. 799 677 THz
Lifetime (τ)	27.102 ns	27.102 ns
Natural Linewidth (Γ)	$2\pi\cdot$ 5.872 MHz	$2\pi\cdot$ 5.872 MHz
Saturation intensity (I_{sat})	7.59 mW/cm^2	2.56 mW/cm^2

Table 2.1: Optical properties of the D_1 and D_2 lines of the ^6Li.

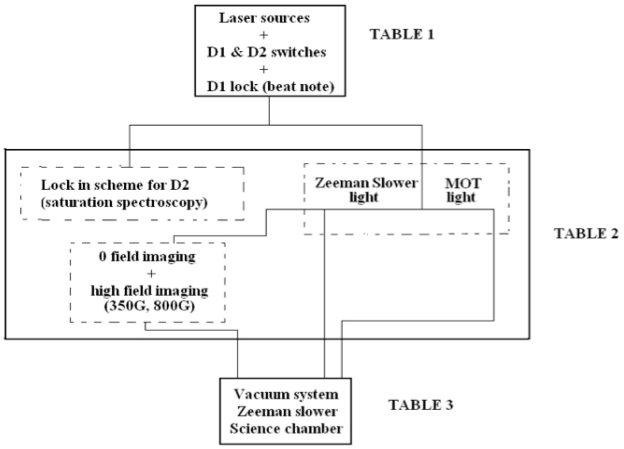

Figure 2.1: *Schematic sketch of the experiment. Continuos lines indicate the light brought by means of optical fibers across different tables and breadboards.*

The experiment is divided into three main parts: a table (Table 1) on which lasers source are placed and switches on D1 and D2 lights are assembled using fast[1] acousto-optic-modulators (AOM). A second one (Table 2) with all optical components to prepare MOT light, Zeeman slower light, imaging light (zero and high field) and with the lock-in scheme for the lasers. This part is actually made on three distinguished breadboards arranged one above the other so to separate imaging, lock-in and the optics for preparation of MOT's lights and whatever. The third part (Table 3) is the actual heart of the experiment and is made of the oven where atoms are evaporated, the Zeeman slower, the vacuum system plus the chamber where the Fermi gas is eventually cool to degeneracy. In figure 2.1 we draw a schematic sketch. In the following paragraphs we provide basic description of each of these parts. The scheme of the experiment is described and commented.

[1] Time scale $< 1\ \mu s$.

Laser sources

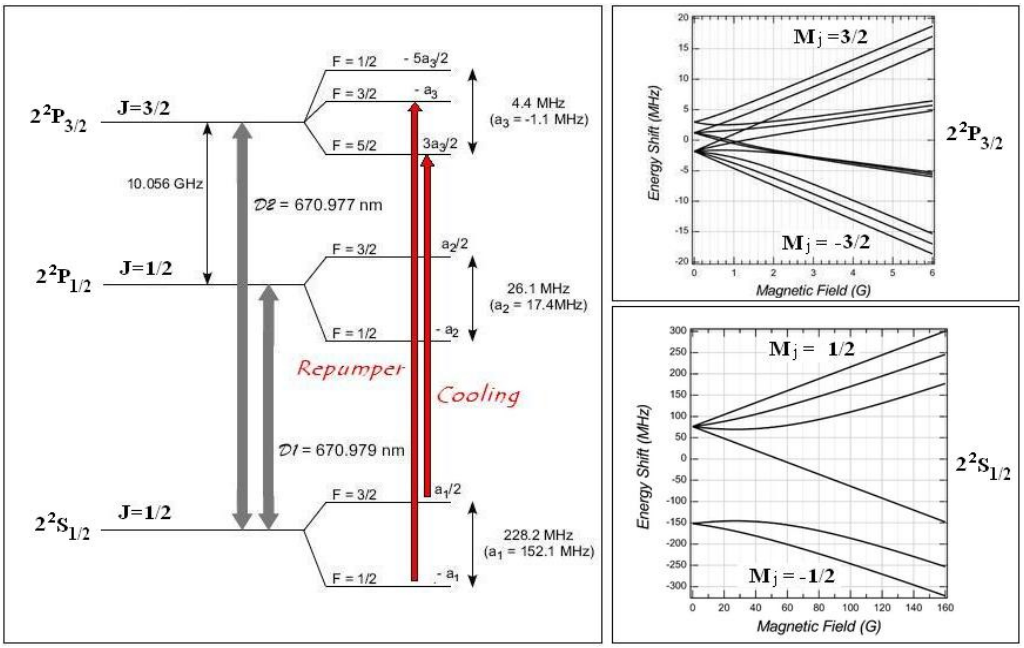

Figure 2.2: *Level diagram of ^6Li. On the left: hyperfine structure of ^6Li. On the right: splittings of levels $2^2S_{1/2}$ and $2^2P_{3/2}$ in the presence of an external magnetic field. Energy splittings are not to scale. Figure adapted from [26].*

We use D1 and D2 lines to laser cool the atoms. Each of them require both repumper (ν_{rep}=$\nu_{F=\frac{1}{2}\rightarrow F'=\frac{3}{2}}$) and cooling ($\nu_{cool}$=$\nu_{F=\frac{3}{2}\rightarrow F'=\frac{5}{2}}$)[2] frequency to work. These lines at zero magnetic field are about 228 MHz far in frequency (see section 1.3) as reported in figure 2.2, so that we can use a single frequency laser source to produce both of them with acousto-optic-modulators (AOM) (see appendix A for some basics). The master laser we use is a Tapered Amplifier High Power Diode Laser produced by TOPTICA. The Master Oscillator Power Amplifier (MOPA) inside it is able to extract a maximum power of 400 mW at a frequency of 671 nm. Using polarization maintaining fibers the light can be brought to other parts of the experiment. All the lights required by the experiment are prepared in power –by meaning of amplifiers- and frequency- by meaning of AOM- on the same table (table 2). The scheme of table 1 is reported in figure 2.3.

[2]We refer to level $2^2S_{1/2}$ with the symbol F and to level $2^2P_{3/2}$ with F'.

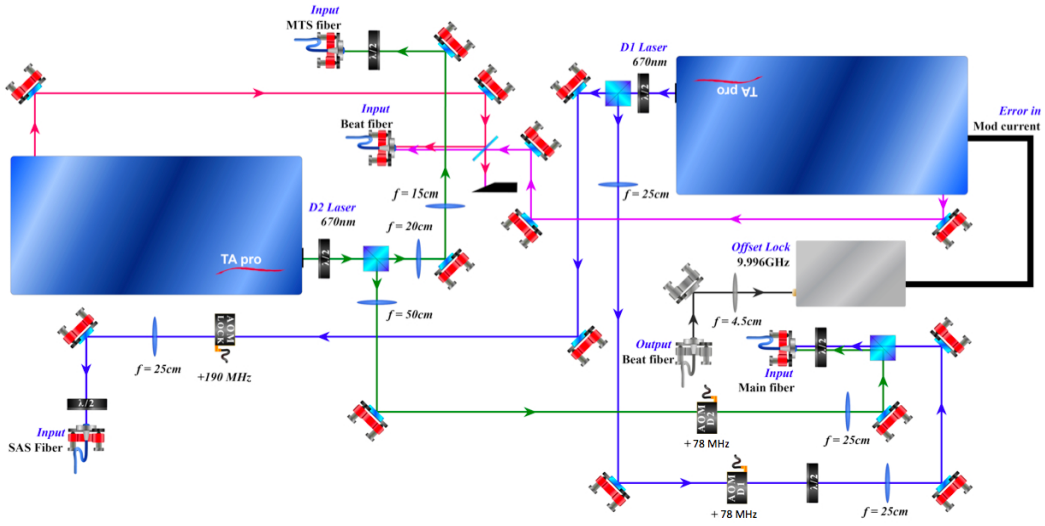

Figure 2.3: *Optical scheme of table 1: we use fast AOMs to switch on/off the light of D1 and D2.*

Lock-in scheme

Having two laser source for D1 and D2 lines, we need two different lock-in schemes for them. The D2 laser is frequency locked by saturated absorption spectroscopy with frequency modulation technique (using an Electro Optic Modulator at 12 MHz), using as *lock point* the cooling transition line $F = 3/2 \rightarrow F' = 5/2$, through a $+140$ MHz double passage configured AOM. Details of our procedure can be found in the master thesis [30]. For the D1 line we arranged a completely different scheme. The difference between the two wavelengths corresponds to a distance in frequency of $\simeq 10$ GHz. We lock the D1 laser on the D2 laser through an offset lock at 10 GHz. To compensate the possible small relative shifts between D1 e D2 transitions, we use both the value of the lock's offset of the D1 laser and the AOMs that we used to produce the D2-frequencies.

2.1.1 Optical system to produce MOT and Slower lights

Frequency shifts

The optical scheme of table 2 concerning the production of MOT lights and Zeeman slower light is reported in figure 2.4. The light is initially split into two paths: one is used for repumping, while the other is used for cooling. Due to lack of separation of hyperfine splitting at low field, their distance in frequency is just due to hyperfine splitting of the ground state level (228 MHz). We

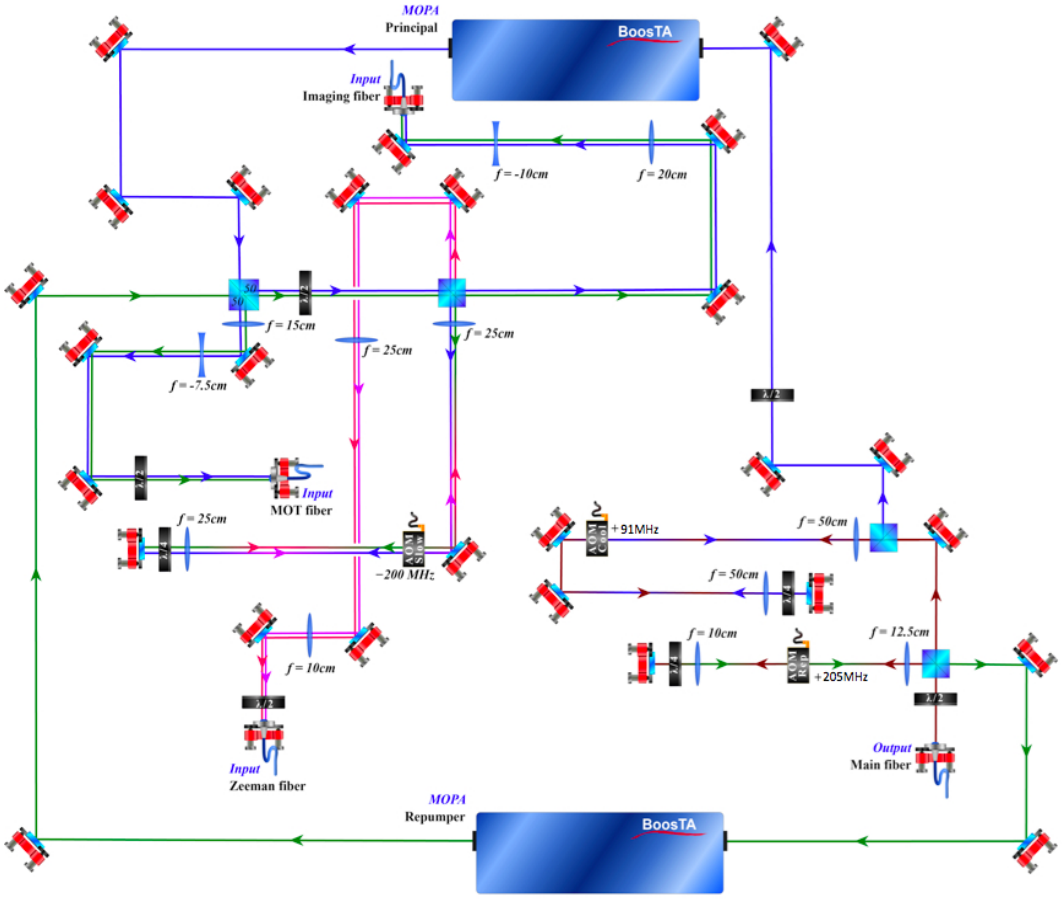

Figure 2.4: *The shifts in frequency reported in figure are referred to single passage of the light. Accounting for double passage configuration they must be multiplied for a factor two to obtain the total shift. The principal beam is used for MOT cooling light, imaging and slower light.*

report in figure 2.5 a scheme of the frequencies shifts. In ν_L we include the frequency shift due to the D2 switch's AOM. Referring to figure 2.3 and 2.4 as

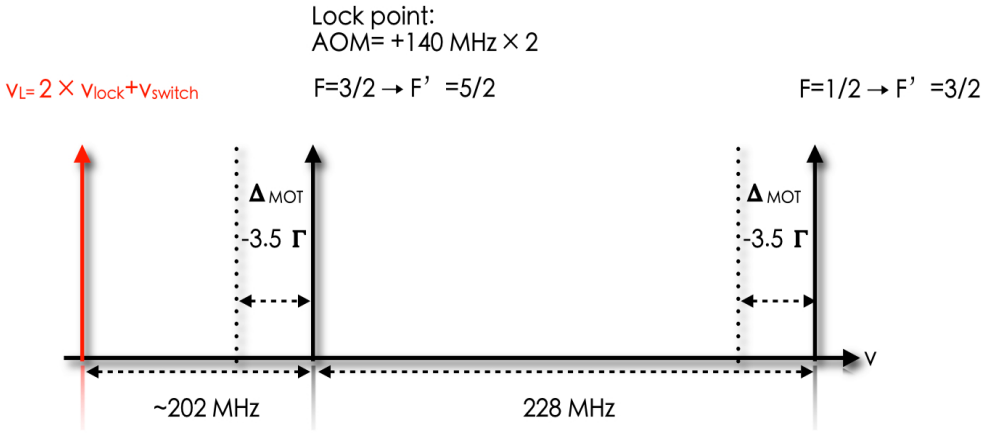

Figure 2.5: *Frequencies scheme of the experiment. The laser light entering the MOT table is frequency locked at* $\sim -202\ MHz$ *of distance from the resonance* $F = 3/2 \rightarrow F' = 5/2$.

outputs of the two BoosTAs we get the MOT beams of frequencies

$$\nu_{MOT} \ : \begin{cases} \nu_{Cooling} = \nu_{+91\times 2} = \nu_L + 91 \times 2\ MHz \\ \nu_{Repumper} = \nu_{+205\times 2} = \nu_L + 205 \times 2\ MHz \end{cases} \tag{2.1}$$

Their difference $\nu_{Repumper} - \nu_{Cooling}$ exactly equals the 228 MHz hyperfine splitting of the ground state (see paragraph 1.3.1). The light power amplifiers (BoosTA) need a linear H-polarized light (in transmission from a PBS system) to work efficiently: entering with about 28 mW of laser light we are able to extract a maximum power of 410 mW from each of them. We then realign the beams along the same track and use a 50% NPB (non-polarization-beam-splitter) to split their powers: half of it goes to the MOT beams - about 200 mW of cooling plus 200 mW of repumper which we split along the three directions x, y, z by means of optical fibers- and the other half is used for both Zeeman Slower light and Imaging. We can control the relative powers of slower and imaging using a $\lambda/2$ plus PBS system.

- *Slower light:* We red-detune this light of $-400\ MHz$ with respect to MOT (and imaging) light by means of double passage through $-200\ MHz$ shifting AOM.

$$\nu_{Slower} = \nu_{MOT} - 400\ MHz \tag{2.2}$$

where with ν_{MOT} we intend both the repumper and cooling frequencies. Details on the Zeeman slower are reported in the paragraph "Zeeman slower".

- *Imaging light:* We inject the light of the slower into an optical fiber and prepare the imaging light on another breadboard. In particular to create the imaging light resonant with the $F = 3/2' = 5/2$ transition we make use of an additional AOM to compensate the shift required for Zeeman slower (see section 2.1.2 for the details).

Independent shutters are used for MOT beams (Uniblitz), imaging (electromechanical shutter), and slower light (Uniblitz plus AOM deflection). All the fibers are stabilized in polarization by means of $\lambda/2$ positioned at their entrances. We can remotely control the detuning of MOT's beams by changing the AOM shifts before the BoosTA; the resultant change in Zeeman slower light's frequency can be compensated with its own AOM.

2.1.2 Imaging cold and ultra cold atoms across different regimes of interaction

Implementation of the optical setup for high field imaging

Since we want to image strong interacting systems, we have to develop a suited optical scheme able to compensate the Zeeman shift at different values of the magnetic field. The main issue that we have to deal with is that, the fast switching off of high magnetic fields, is not straightforward for our apparatus, due to both inductance of our coils and the auto inductance of the chamber. Furthermore at high field we may use non-destructive phase contrast imaging, sensitive to the single spin state, to address the physics close to the Feshbach resonance (834 *Gauss*) [35]. This may result in switching off times of the order of tens of milliseconds. The scheme we developed is reported in figure 2.6. In particular we perform the imaging along the horizontal direction, thus observing the cloud with light ($\mathbf{k}$) $\perp$ to B: selection rules 1.53 apply.

To perform 0 field imaging, we need to compensate the shift of the slower light and the MOT detuning (+210 MHz). Instead for high values of the magnetic field, we image the closed atomic transition (σ line) from level $|M_j = -1/2\rangle$ of the ground state and $|M_j' = -3/2\rangle$ of the excited state which scales as $\mu_B B$ [3]. For example at $B = 800$G, the total Zeeman shift is $\Delta E(800) \simeq$

[3] Their individual split -neglected the nucleus contribution- is given by 1.51:

- $2^2P_{3/2}$: $m_j = -3/2 \quad \rightarrow \quad \Delta E_z \simeq \mu_B g_j m_j B = -\mu_B (1.335) \frac{3}{2} B \sim -2\mu_B B$
- $2^2S_{1/2}$: $m_j = -1/2 \quad \rightarrow \quad \Delta E_z \simeq \mu_B g_j m_j B = -\mu_B 2 \frac{1}{2} B \sim -\mu_B B$

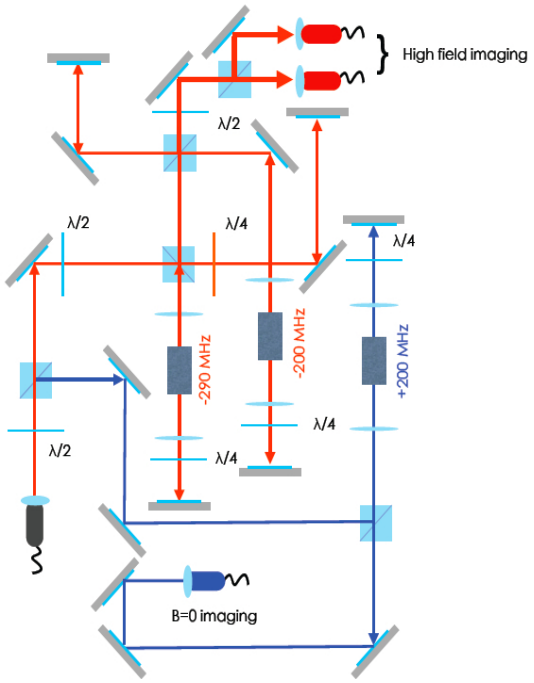

Figure 2.6: *Optical setup for zero field imaging and high field imaging.*

$\mu_B B = 1.4\frac{MHz}{Gauss} \cdot 800 Gauss \sim 1100 MHz$. We can produce the required light shift for imaging adding to the slower's detuning others $-350 \times 2 = -700 MHz$.

Absorption Imaging Scheme

To extract from the atomic cloud all the interesting information, such as the number of atoms or the temperature, we use absorption imaging. A sketch of the absorption scheme is reported in figure 2.7. Absorption scheme is much suited to detect atoms in the dipole trap. While in fluorescence the spontaneously reemitted light by the atoms is collected by a lens and focused to form the image of the cloud, in *absorption imaging* we detect the presence of the gas from the shadow cast on the imaging quasi resonant laser pulse detected by the CCD camera. The power per unit time emitted by atoms as a consequence of the spontaneous decay from excited state is given by [29]

$$P = (\hbar\omega_0)(N\tilde{\rho}_{ee})\Gamma \tag{2.3}$$

At equilibrium we have equal and constant rates of absorbed and emitted energy from the cloud so that, being Σ the laser beam cross section, the decrease of

This means their distance in energy reduces with the field as their difference $\sim -2\mu_B B + \mu_B B = \mu_B B$.

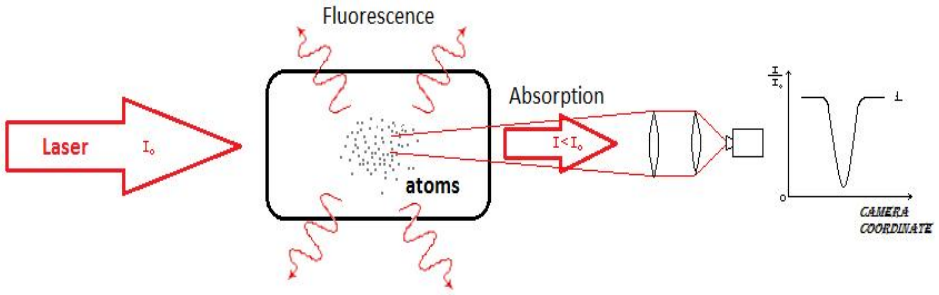

Figure 2.7: *Sketch of experimental setup of absorption imaging. The intensity signal detected by the CCD camera has in the reality two camera coordinates: in figure we reported just one for simplicity.*

laser intensity after a certain distance dz in the gas is given by

$$dI = -\frac{1}{\Sigma}P = -\frac{1}{\Sigma}N\hbar\omega_0\Gamma_{scatt}(\vec{r}) = \cdots = -\sigma(\omega_0)n(\vec{r})I(\vec{r})dz \tag{2.4}$$

where we used equation 1.61 and 1.63, $\sigma(\omega_0)$ being the *photon scattering cross section* of the gas and n the number of atoms per unit of volume. The CCD detects the light passed throughout the entire cloud (as shown in figure 2.7), which means that in the experiment we are actually measuring the integral quantity

$$I(x,y,z) = I_0 e^{-\sigma(\omega_0)\int_{-\infty}^{\infty} n(x,y,z)dz} \tag{2.5}$$

We can then extract the so called *column density* of the cloud, i.e. the integral of density distribution along the probe beam direction

$$n(x,y) = \int_{-\infty}^{\infty} n(x,y,z)dz = \frac{1}{\sigma(\omega_0)} ln\Big(\frac{I_0(x,y)}{I(x,y)}\Big) \tag{2.6}$$

At resonance ($\delta = 0$) and in the linear absorption regime ($s << 1$) we get

$$\sigma(\omega_0) = \hbar\omega_0\frac{\Gamma}{2I_s} = \hbar\omega_0\frac{\Gamma}{2\big(\frac{\hbar\Gamma\omega_o^3}{12\pi c^2}\big)} = \frac{3\lambda^2}{2\pi} \tag{2.7}$$

that is the resonant absorption cross section. To compute equation 2.6 we must measure the intensity before (I) and after (I_0) the atoms. In our experiment three images are actually taken by the same CCD: first the absorption image of the atoms (I), second the intensity profile of the laser probe beam without the atoms (I_0), and third the background with all light off to identify stray light or electronic background noise in the camera picture. To avoid fluctuations in power and direction of the probe beam the first to images should be taken as close as possible compatibly with the acquisition time of the camera: we set

their distance to approximately 200 μs. The first one is a TOF-*Time of Flight*-image of the atom after a free ballistic expansion time that depend on the temperature of the cloud: the hottest the cloud the shortest the TOF should be to allow detection of the atoms before escaping the probe path. More the light pulse must be as short as possible: this is for preventing momentum diffusion of the atoms due to pressure forces arising from resonant scattering process used to picture them. Typical numbers are 30/40 μs. The real density profile is calculated as follow

$$n(x,y) = \frac{1}{\sigma(\omega_0)} ln\Big(\frac{I_{atoms}(x,y) - I_{background}(x,y)}{I_{no\ atoms} - I_{background}}\Big) \tag{2.8}$$

To precise measure the density 2.8 we need also to account for efficiency of CCDs as explained in the next paragraph.

CCDs cameras

The camera adopted for both absorption and fluorescence is a Stingray F-145B model. The first one is a 1388x1038 pixels matrix the size of each pixel being of 6.4μs per side. Calibration of the CCD is required to measure its efficiency. This was done [30] by shining a laser beam of known intensity for a fixed amount of time. The signal on the camera is converted by a software in the number of counts of incident photons during the operation time. Knowing the power of the incident laser beam and the energy of a single photon, we obtain the ratio

$$\eta = \frac{number\ of\ counts}{number\ of\ photons\ shined\ onto\ CCD} \tag{2.9}$$

which gives the efficiency of the CCD. We found $\eta = 0.89 \frac{counts}{photons}$. The number of photons can be evaluated with the formula:

$$N_{ph} = \frac{Pt_{exp}}{\hbar\omega} = \frac{t_{exp}}{\hbar\omega}\frac{IA}{M}\frac{1}{\eta} \tag{2.10}$$

where P is the incident power, M the magnification of the optical system, A the surface of the pixels, t the illumination time of the CCD and the denominator is the energy of the single photon. The quality of the imaging depends on the time of exposure of the cloud to the laser light: in fact the signal to noise ratio for Poissonian statistic of laser light is $S/N \simeq \sqrt{N_{ph}}$ which is indeed proportional to the duration of the imaging pulse. Of course the duration can not be increased arbitrarily since the increase in number of scattered photons leads to displacement of atoms and affects their initial momentum distribution. The displacement induced by single photon scattering event can be estimated with classical arguments using the recoil velocity v_{rec} multiplied for the illumination

time.

Fluorescence imaging

When shined by a laser beam, an atomic vapor will emit a fluorescence signal proportional to the absorbed light. The absorption depends on the scattering rate as already explained in chapter 1. We have to assume that the cloud is transparent to spontaneously emitted photons, so that the fluorescence signal will be directly proportional to the scattering rate and to the total atom number as well. Thanks to eq. 1.64 this can be written as:

$$V = AN\hbar\omega\frac{\Gamma}{2}\frac{I/I_s}{1+I/I_s+(2\delta_0/\Gamma)^2} \tag{2.11}$$

where V is the intensity of the signal, N is the total atom number and A is the conversion factor of our detecting system. The constant A depends both on the response of the photodiode and on the fraction of solid angle covered by our imaging system. The final expression for the determination of the total atom number has the following form:

$$N = \frac{R}{V}\frac{\delta\Omega}{4\pi}\frac{2}{\hbar\omega\Gamma}\frac{1+I/I_s+(2\delta_0/\Gamma)^2}{I/I_s} \tag{2.12}$$

where R is the response of the photodiode and $\frac{\delta\Omega}{4\pi}$ is the fraction of solid angle. We use fluorescence both for imaging trapped cloud in the MOT and for the D1 stage of cooling and proper alignment on the MOT itself. Furthermore, for the optimization of the atom number trapped by the MOT, we look at the atoms through their emitted fluorescence signal, from which we can easily estimate the total atom number. The fluorescence signal from the MOT is collected onto a photodiode, placed just outside the science chamber, the fraction of solid angle we measured for our configuration is $\frac{\delta\Omega}{4\pi} = (9 \pm 2) \cdot 10^{-3}$.

2.1.3 Optical setup for absorption and fluorescence imaging

Horizontal imaging:

We can image the atomic cloud horizontally at both zero and high field. We bring the light from table 2 (see figure 2.6) by means of polarization maintaining fibers close to the science chamber. The optical scheme is reported in figure 2.8. At zero field the polarization of the light is not relevant since quantization of space does not occur. For high field imaging we use a $\lambda/2$ wave plate to rotate the polarization $\perp$ to the direction of the Feshbach field: we image the σ lines

(see eq. 1.53). The fluorescence and absorption signals are collected on a CCD through a $\times 2$ magnification system using lenses of focal $f = 150\ mm$[4] and $f = 300\ mm$[5].

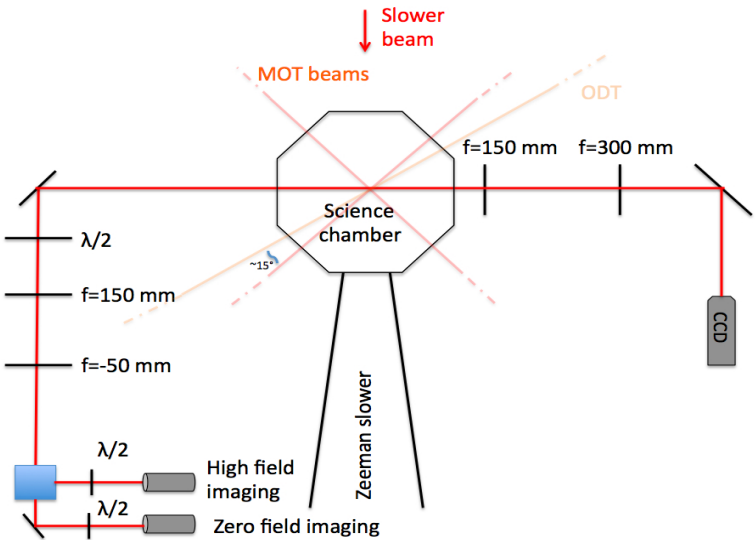

Figure 2.8: *Horizontal optical setup for zero and high field imaging.*

Vertical imaging:
We are going to implement a vertical imaging system, allowing observation along the magnetic field ($\mathbf{k} \parallel B$). Given the selection rules 1.53, we will use circularly polarized light to image the cloud on the close transition $|2S_{1/2}, m_j = -1/2\rangle \rightarrow |2P_{3/2}, m_j = -3/2\rangle$. This improves the imaging contrast due to larger absorption. Furthermore this scheme is much more suited to image our cigar-shaped cloud with respect to the horizontal one, due to the angle between the 1070 nm laser light used for ODT and the horizontal imaging light.

2.2 Vacuum system

The vacuum system of the experiment is composed of different sections. They are schematically reported in figure 2.9. With the help of laser cooling techniques (see section *Cooling scheme*) the experimental apparatus we are going to describe allows for achievement of quantum degeneracy of fermionic Lithium, eventually in the superfluid regime.

[4]Model: Thorlabs AC508-300-A
[5]Model: Thorlabs AC508-150-A

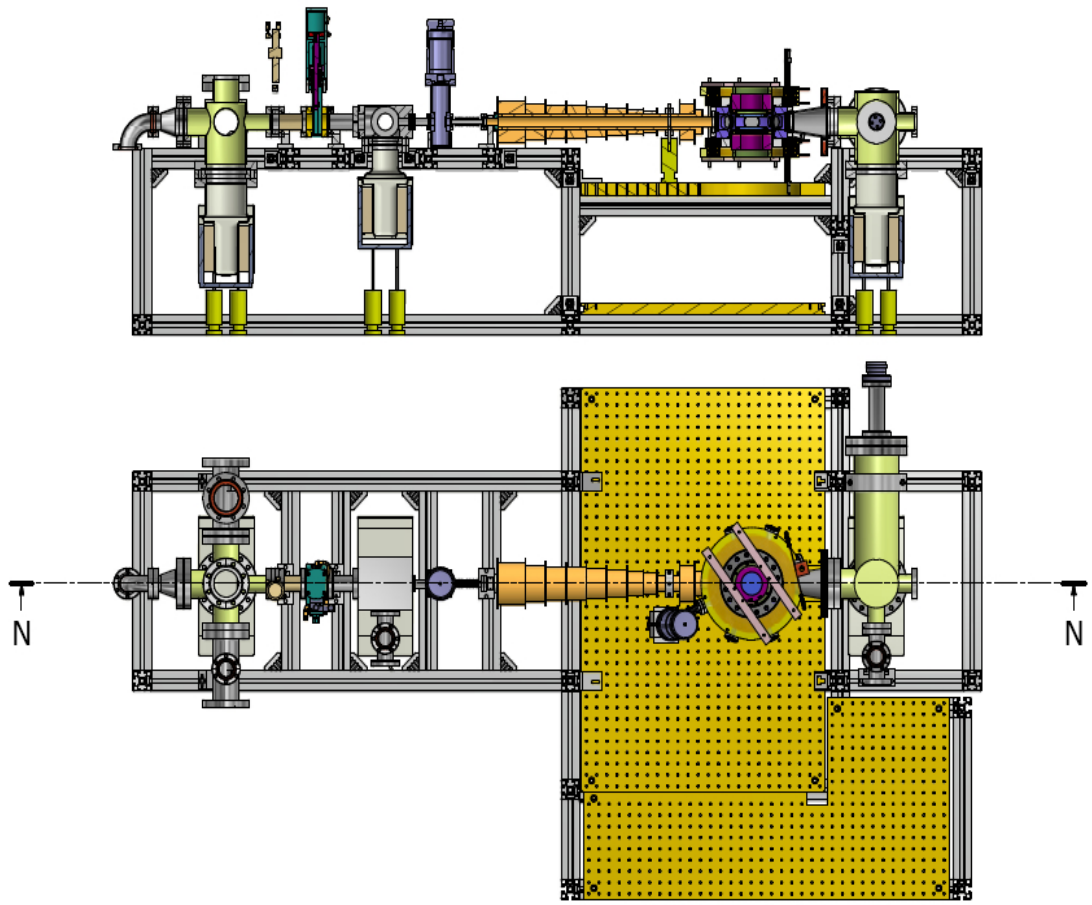

Figure 2.9: *Project of the vacuum apparatus. It can be thought as composed of two main parts: the first (Oven and Differential pumping) is assigned to the production of a thermal lithium beam; the second (Zeeman slower, Science chamber) is devoted to cool the gas down to superfluid regime.*

2.2.1 The oven

In this part we will basically report the summary of what already described in details by [30]. Our experiment has a source of bulk enriched ^{6}Li of about 10 g with purity of 95%. This source is heated up to $\sim$ 400 $^\circ C$ in order to produce a suitable vapor pressure of lithium atoms. The atomic vapor from the effusive oven is collimated by two small successive apertures: the first one is called *nozzle*, and is adjustable in its position, so to achieve a better alignment of the out coming beam with the science chamber. After it a second regulable aperture, a copper plate called the *cold plate*, is kept cold using a Peltier cell[6]: hot atoms with misaligned direction with respect to the science chamber will strike and be stuck onto it and they will be stopped before entering the rest of the experiment. A pneumatic shutter is used to stop the atomic beam preventing it from entering the Zeeman slower. It is kept closed after loading the MOT. The differential pumping stage is not described here. For further details refer to [30].

2.2.2 Zeeman Slower

In order to efficiently load the atoms from the beam into the MOT, we need to affect their velocity distribution. Indeed only the atoms with a velocity lower than the MOT capture velocity- which is about a few tens of m/s- can be trap [30]. Since the oven temperature is about 400°, the average velocity of the atoms coming out of it is approximately:

$$\frac{1}{2} m_{^6Li} v^2 = k_B T \qquad \Rightarrow \qquad v \sim 1350 m/s \tag{2.13}$$

This velocity is roughly two order of magnitude higher than the MOT capture velocity. Therefore to reduce it, we take advantage of the light pressure of a counter-propagating red-detuned laser beam. The red detuning takes care of Doppler effect experienced by moving atoms with respect to the frequency of the radiation: because of their velocity and the counter propagating configuration, the radiation will be "seen" by the atoms as blue-detuned by an amount proportional to their velocity, and must than be red-detuned in advance to match the resonant condition 1.63 that maximizes its slowing force. It must also be noticed that this is not enough to provide an efficient drift of the average velocity toward the capture limit. As soon as atoms are slowed, the Doppler effect will decrease and laser light will no longer affect their velocity distribution. For

[6] A common Peltier cell is formed by two p and n doped semiconductor materials connected with each other by a thin copper plate. Based on Peltier effect, the cell is able to transfer heat from a junction to another when a current is fluxed in the copper circuit.

example after the absorption of N=80000 photons, the detuning $\delta = \delta_0 - \vec{k} \cdot \vec{v}$ will be shifted by an amount of $\Delta\delta = -k\frac{N\hbar k}{m} \sim -2.5\Gamma$ from resonance[7]. In a *Zeeman Slower* the Doppler shift of moving atoms with respect to resonance with laser light is compensated by the energy shift due to an external magnetic field which is tuned in space to maintain the resonance condition. So starting with velocities around 1350 m/s, only atoms absorbing around $N = \frac{m\Delta v}{\hbar k} \sim 10^5$ photons will be trapped. All the others will escape the trap. The magnetic field gradient is generated by a set of in series coils designed in such a way that the deceleration acting on the atoms due to radiative pressure is constant. The design of our *Slower* is sketched in figure 2.10.

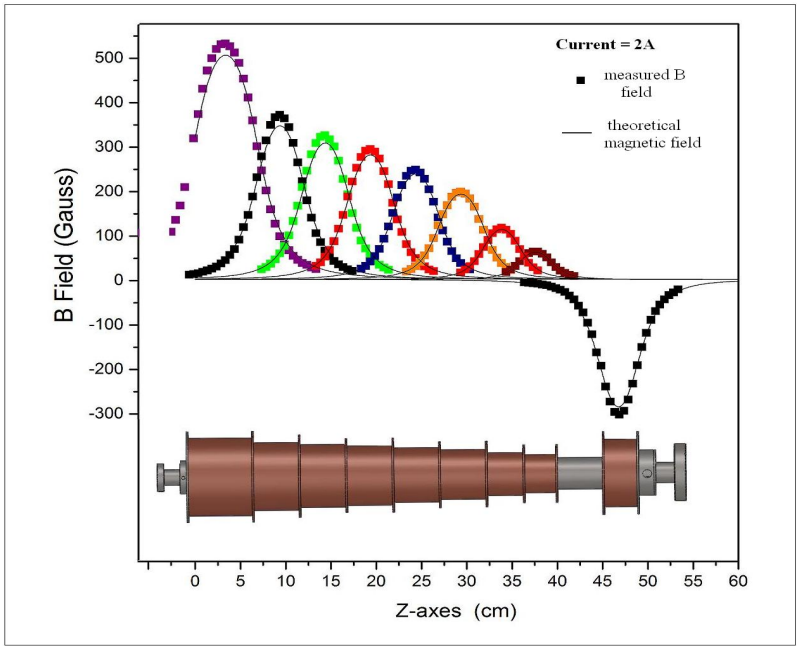

Figure 2.10: *Sketch of the slower with the simulated and measured magnetic fields plotted one on the other for each coil. The simulated field is the one maximizing the deceleration of atoms for certain boundary conditions.*

This condition of resonance $\delta = 0$ is met when the detuning also include Zeeman splitting of hyperfine levels:

$$\delta = \omega - \omega_0 - \vec{k} \cdot \vec{v} + \frac{\Delta E_{zs}(B)}{\hbar} \tag{2.14}$$

being ω the frequency of the laser radiation, ω_0 the atomic transition frequency between hyperfine levels on which the slower is working, $\Delta E_{zs}(B)$ the energy

[7] In fact the variation of velocity due to single (counter propagating) photon absorption is $\Delta v = -\hbar k/m$ while for N photons will be N times larger.

splitting due to Zeeman effect of these levels and $\vec{k} \cdot \vec{v}$ the well known Doppler effect contribution.

Our *Slower* is working on the transition

$$|^2S_{1/2}\ m_j = 1/2\rangle \rightarrow |^2P_{3/2}\ m_j = 3/2\rangle \tag{2.15}$$

The light inducing this transition is parallel to the direction of the magnetic field inside the slower. Thus from selection rules 1.54 this transition can be driven by σ^+ polarized light. The Zeeman shift inside the coils can be calculated through eq. 1.51, that for this transition, as explicitly calculated in section 2.1.2, is approximately $\Delta E_{zs} \simeq \mu_B B$. Now from equation 2.14, at resonance, we get for counter propagating configuration

$$B = \frac{\hbar}{\mu_B}(\delta_0 + kv) \tag{2.16}$$

We designed the slower to get a constant deceleration along the direction of propagation of the atoms as shown in figure 2.11. It can be seen that fast

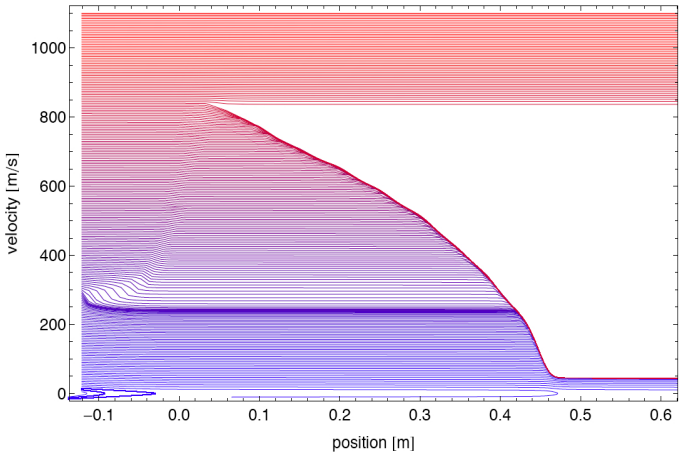

Figure 2.11: *Schematic phase space diagram of the atom trajectories for different initial velocities. For value higher then the capture range v_0 the atomic motion is not affected by the slower. Figure taken from [30].*

atoms are the first ones to be slowed due to their great Doppler effect, while slower ones will be captured in the latest part of the tube. The velocity varies with the position along the axis as $v^2(z) = v_i^2 - 2az$ which means the magnetic field must vary as $B = \frac{\hbar}{\mu_B}\left(\delta_0 + k\sqrt{v_i^2 - 2az}\right)$. For our slower we set $v_i \sim 800m/s$. This gives a starting Doppler shift $(\nu_{Slower}\frac{v}{c})$ at the first coil of $\sim 1.1 \cdot 10^3 MHz$ which must be summed to the red detuning of the light of the slower which is -400MHz. Thus, at the entrance of the slower, the total shift from

the transition resonance 2.15 that has to be compensated with Zeeman effect, is about 700MHz. This requires a magnetic field of $\sim 500 Gauss$ according to $\Delta E_z \sim \mu_B B$. The parameters of our slower, i.e. the powers and detuning of cooling and repumper lights are reported in table 2.2.

$\delta_{0,\ Cool.\&Rep}$	$P_{Cooling}$	$P_{Repumper}$	Final velocity
$-400\ MHz = -68\Gamma$	$50\ mW$	$50\ mW$	$\sim 30\ m/s$

Table 2.2: Optimal parameters of our Zeeman slower.

In addition to the cooling light, we add to the slower beam also the repumper light. This is due to the so called *spin flip* configuration (the last coil of the slower has an inverted magnetic field which produces a flip of the atom's spin): in fact the magnetic field goes to zero at the position were the B field changes its sign. Here m_j is no more a good quantum number and the transition 2.15 is no longer closed. Atoms can escape the cooling cycle and fall in the "dark" state $|F = 1/2\rangle$ of the ground state. Repumper light brings back those atoms into the cooling cycles. The big advantage of this configuration over a simple decreasing one, is that slowed atoms coming out of the Zeeman slower are not resonant with the counter propagating beam, allowing a better loading of the MOT. The relative percentage of cooling and repumper light are due to the intrinsic design of the optical scheme: reducing the repumper intensity on the Zeeman slower beam would reduce also the repumper intensity on the MOT (see figure 2.4). Since the capture velocity of our MOT is $\sim 60\ m/s$ the slower allows good loading. For details refer to the next section.

The magnetic field generated inside the tube has been measured with a Hall sensor. In figure 2.10 we plot the measured field over the simulated field profile optimizing the capture range of the MOT given the initial velocity distribution from the oven, which is Maxwell-Boltzmann distributed. As can be seen the first three coils have value slightly different from the computed ones. To compensate for it we run these coils on independent suppliers and optimize the loading of the MOT. We obtained an increase of about 10% on the loading efficiency. The overall optimization was also run in detuning of Cooling and Repumper light. For details on the windings of the coils see [30].

2.2.3 Main chamber and MOT loading

Atoms leaving the Zeeman slower enter the main vacuum chamber where we perform the experiments. The chamber manufactured by Kimball Physics, has an octagonal shape and it is equipped with re-entrant vertical windows (see

section 3.0.4) allowing close positioning of short focal optics with high NA (and thus high resolution) to its center. The scheme of the chamber is reported in figure 2.12 with an image of the magneto-optical trapped cloud. The differential pumping stage of figure 2.9 provide a pressure drop of about three order of magnitude from $\sim 10^{-8}$ *mbar* in the oven to $\sim 10^{-11}$ *mbar* in the main chamber. For details on its functioning, we address to [30]. We realize our MOT with three retro-reflected opposite circular polarized beams (see configuration 1.11) of 1" diameter. Operating the oven at $400°C$ gives a flux of atoms entering the Zeeman slower of about $\sim 1.57 * 10^{10}$ $atoms/second$. In tab. 2.3 we report the parameters of our MOT and its capture rate.

$\delta_{Cool/Rep}$	$P_{Cool/Rep}$ $[mW]$	$\partial B/\partial z[\frac{G}{cm}]$	$\Gamma_{Capture}$ $[\frac{atoms}{second}]$	T $[mK]$
-3.5Γ	~ 30	24	$\sim 3 \cdot 10^8$	~ 1

Table 2.3: The powers showed are referred to single beam.

The overall loading efficiency is thus $\sim 10^{-3}$. In approximately 4 seconds we are able to load a MOT of $\sim 10^9$ atoms.

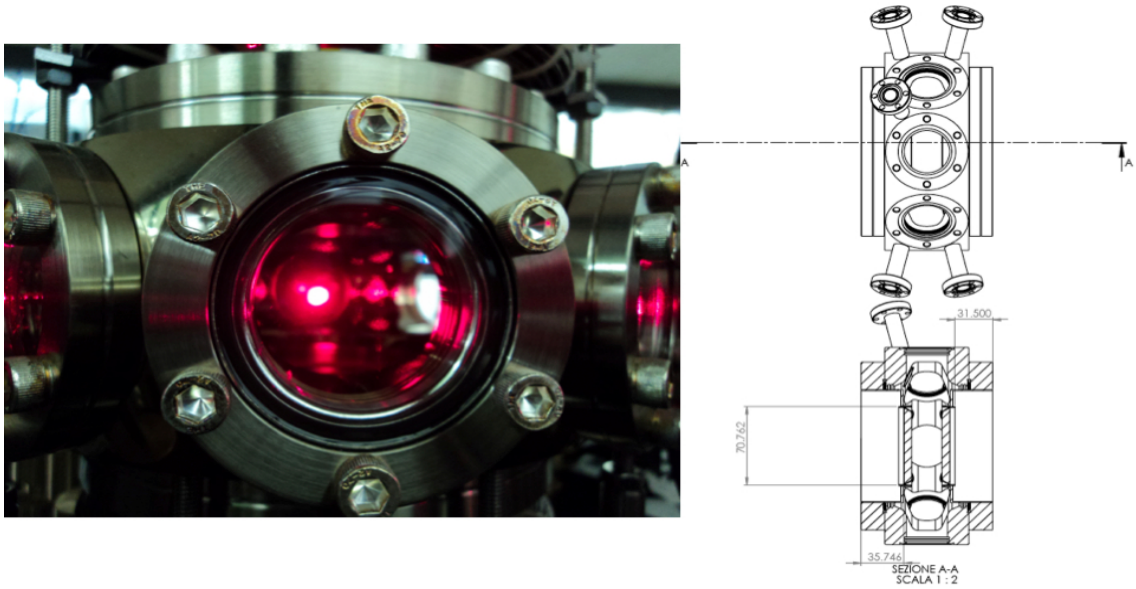

Figure 2.12: *On the right: draw of the main vacuum chamber. On the left: fluorescence image of a MOT of* $\sim 10^9$ *atoms at* ~ 1 mK *temperature.*

2.3 Magnetic field coils

2.3.1 Feshbach coils

To tune the scattering length of ^{6}Li across the Feshbach resonance of the states $|1\rangle$ and $|2\rangle$, we need a set of coils which are able to produce high uniform values of the magnetic field (up to 832 G). The coils we used are placed outside the science chamber as shown in figure 2.13. They are made of a squared hollow wire (4.6×4.6mm including the kapton insulating sheet). Their internal radius is 79 mm and they are 57 mm apart from the atomic cloud. They consist of 6×8 turns. They are in quasi-Helmholtz configuration: at 180 A, corresponding to $B \sim 840$G, they provide a radial[8] magnetic curvature of about $\sim 3\text{G/cm}^2$, which gives a radial frequency for ^6Li atoms in the lowest hyperfine states ($|1\rangle$ and $|2\rangle$) of 10 Hz. These coils[9] are vacuum impregnated, using ARALDIT F. It is an epoxy resin, allowing a maximum temperature of 155°C. The maximum field they are able to produce is $\sim 1\ kG$ corresponding to the maximum current of our power supply[10] of 220 A.

2.3.2 Curvature/Quadrupole coils

Since the axial frequency of a single focussed beam is reduced by a factor w/z_R with respect to the radial one (see 1.4.2), during evaporation a single-beam trap is not able to provide a convenient confinement for the atoms along its axis. Thus along that direction, in addition to the curvature produced with the Feshbach coils, we make use of an additional magnetic curvature providing a trapping potential $U_{curv}(B) = \frac{1}{2}\mu_B B''(0) r^2 = \frac{1}{2} m\omega^2_{curvature} r^2$: in this way at low power, the curvature frequency compensates the low axial frequency of our ODT. We produce this main curvature using relays to switch the currents of the MOT coils from anti-Helmholtz to quasi-Helmholtz configuration[11]. The relay system is mounted in series to the lower coil and in parallel to the upper one, and it's meant to invert the direction of the current in the upper coil of the quadrupole, in such a way that the magnetic curvature field results summed to the Feshbach magnetic field. The MOT coils are a distance $R_{coil} = 54\ mm$ away from the trapped atoms. For high field seekers states $|1\rangle$ and $|2\rangle$, which we use as fermions mixture to perform evaporative cooling efficiently, the coils provide a trapping

[8] We mean with respect to the axis of the coils.

[9] Company: Oswald, Germany.

[10] Model SM 15-200 D, Delta Elektronika.

[11] Perfect Helmholtz configuration would not provide any curvature. Curvature is obtained provided that the distance between the coils is kept a bit larger then their radius.

curvature[12] field along the axis of the optical trap (horizontal) with estimated trapping frequency $\omega_{curvature} = 2\pi \cdot 16\ Hz$, while in the vertical direction states $|1\rangle$ and $|2\rangle$ experience an anti-curvature (anti-trapping potential) of estimated frequency $\omega_{anti-curvature} = 2\pi i \cdot 16 \cdot \sqrt{2}\ Hz$. The quadrupole/curvature coils we use are placed in the re-entrances of the vertical windows of our vacuum chamber (figure 2.13). The calibration of the MOT coils was performed with a

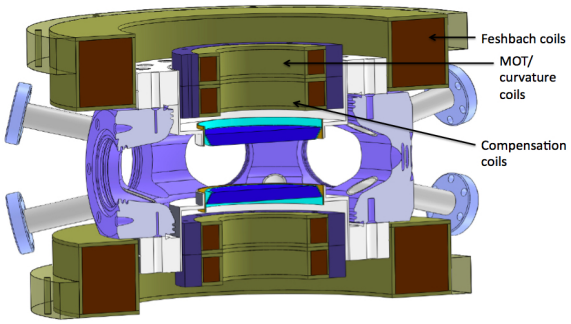

Figure 2.13: *Scheme of the coils around the science chamber. Outside the chamber we have the Feshbach coils, while inside the re-entrant windows we have placed two set of coils: the top ones are used for compensation; the bottom are the quadrupole coils used to produce the MOT and curvature field in the last stage of evaporation.*

Hall sensor outside the chamber.

2.3.3 Compensation coils

To compensate spurious magnetic field inside the chamber we use compensation coils. In correspondence to each optical horizontal access of the chamber we placed compensation coils. Vertical compensation is achieved by placing a second pair of coils beneath the MOT coils (see figure B.1). We can also use this latter pair of coils to produce a displacement of the zero of the magneto-optic-trap. This can be useful particularly in the stage of D1 molasses, since the displacement of the MOT along vertical direction can be used to center the molasses beams on the atoms. To displace the center of the trap of z_0 along $\hat{z}$, we need to add to the MOT field another field such that

$$\begin{aligned} B_{tot}(z) &= B_{comp}(z) + B_{MOT}(z) \\ &= (b_{comp} + b_{MOT})[G/cm](z - z_0)[cm] \end{aligned}$$

[12]The curvature or anti-curvature provided by the magnetic field must be referred to the sign of the magnetic moment of the atoms in a certain internal state.

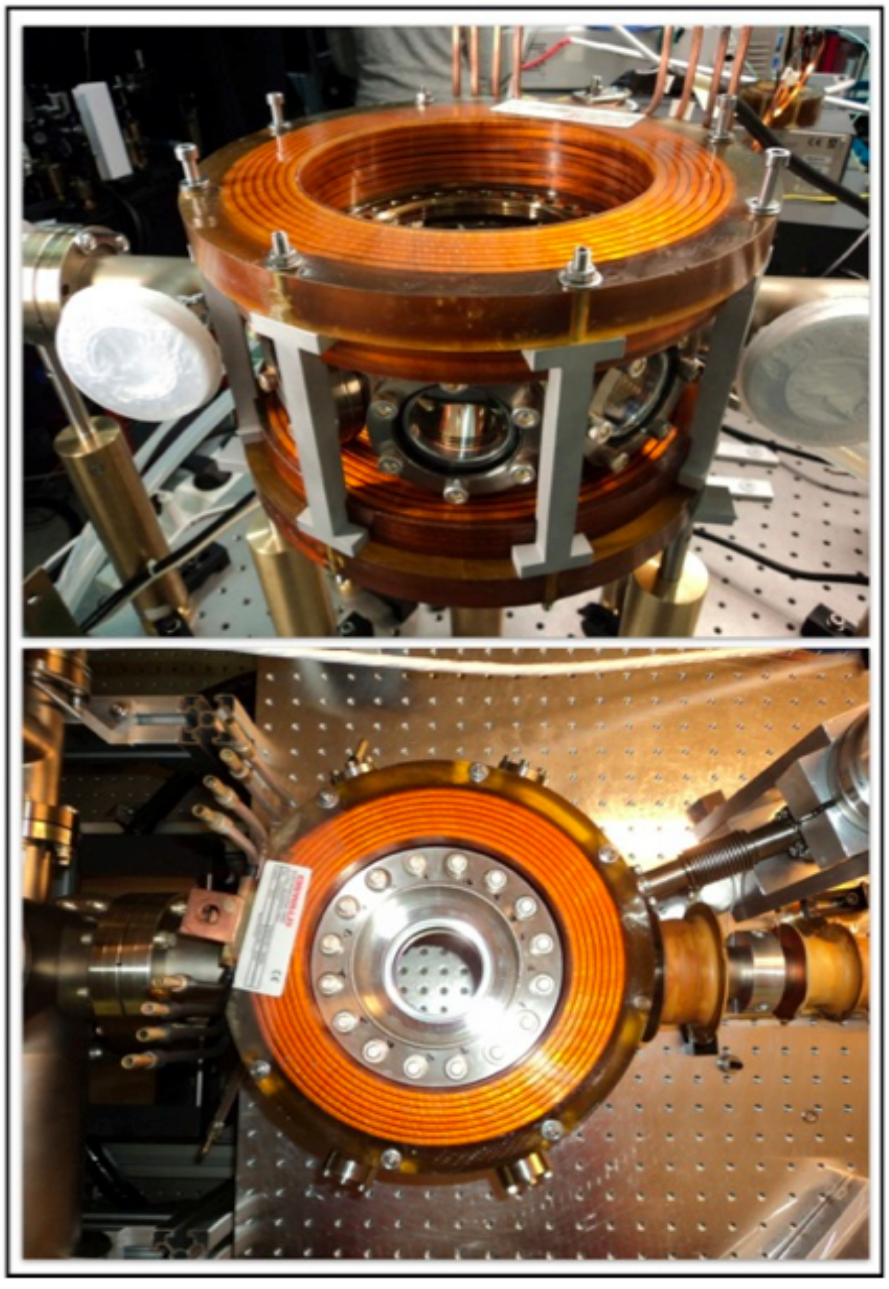

Figure 2.14: *Pictures of the Feshbach coils described in the text.*

Another use we may want to do of these coils is linked to the vertical imaging system we are going to implement in the near future. In fact, moving the cloud along vertical axis could allow to achieve better focussing on the vertical imaging, which we will perform with short focal ($f = 32\ mm$) aspheric lens. We report in appendix B.1 the configuration of the quadrupole/curvature and compensation coils.

Chapter 3

High-resolution imaging and thin barriers for ultra-cold atoms

In this chapter I will describe a good part of my thesis work, i.e. the characterization and design of an optical setup to both perform imaging with resolution ($\sim$1 μm) approaching the diffraction limit and imprint on our superfluid system a sheet-like optical potential barrier. Indeed we are interested in observing and resolving the dynamics of fermionic systems with resolution of a few inter particle spacing ($\frac{1}{k_F} \sim 1$ μm for typical experimental values). We will also discuss how to integrate this imaging with the MOT setup and, eventually, with the rest of the experiment.

3.0.4 Experimental implementation

Within the experiment we have to superimpose several beams along the vertical direction.

- MOT light beams
- Imaging light beam
- Green sheet of light

A sketch of the experimental setup is shown in figure 3.1. The MOT and the imaging beams are superimposed via a polarizing beam splitter. After the chamber (see figure 3.1) to separate the imaging from the retro-reflected MOT

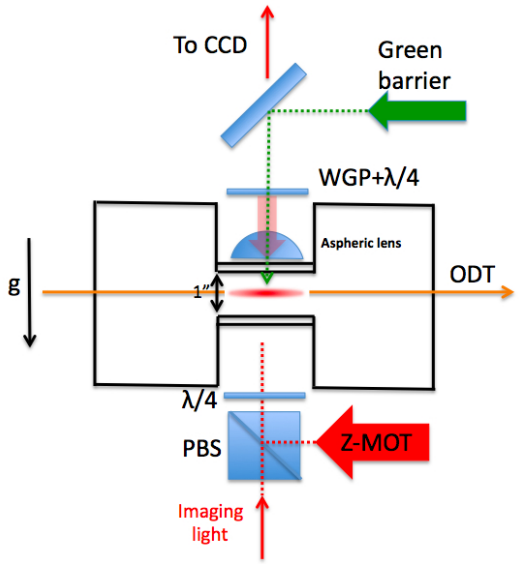

Figure 3.1: *Scheme of the experimental setup to superimpose the MOT, imaging and green beams along the vertical direction. The z-MOT beam is retro-reflected by means of a WGP and $\lambda/4$ waveplate. The imaging beam (670 nm) and the green barrier (532 nm) are combined by a dichroic plate.*

beam with the required $\sigma^+ - \sigma^-$ polarization, we use in close sequence a very thin 2" diameter $\frac{\lambda}{4}$ wave plate (200 μm thick) and a 2" wire grid polarizer [1] (700 μm thick).

To achieve optimal retro-reflection of the MOT beam after crossing the aspheric lens, the WGP and $\frac{\lambda}{4}$ wave plate are displaced of ∼32 mm from it. Due to the damage threshold of the WGP (50 kW/cm^2 for our model) we can not place the optics exactly in its focus. We have designed a compact holder to keep all the optics in the correct position, which for sake of clarity is not shown in fig.3.1.The combination of this holder with a 3D tilter will allow the alignment of the optics on the atoms. The green light (532 nm) required for the barrier is superimposed to the imaging beam by a dichroic plate.

The imaging will be performed using the $f = 32$ mm and a sequence of lenses of focal $f = 300$ mm, $f = 40$ mm (achromat) and $f = 150$ mm. A CCD will collect the signal in the focus of the last lens. The $f = 300$ mm and $f = 40$ mm will be mounted in telescope configuration on flip montages. This allows fast switching between a $\sim \times 5$ and $\sim \times 50$ magnifying imaging system which can be

[1] A WGP is an optical element which reflects light with polarization orthogonal to a certain axis and transmits light with polarization parallel to it. We used Meadow Lark optics model VLR-200-NIR

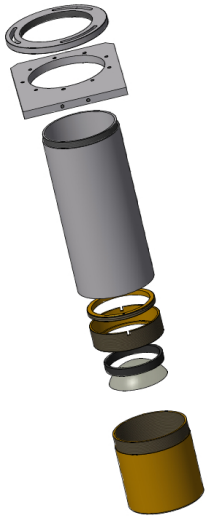

Figure 3.2: *Image of the designed holder for the $f = 32mm$ lens, $\lambda/4$ waveplate and wire grid polarizer.*

used respectively to image the cigar-shaped cloud and the thin barrier.

Re-entrant windows

One of the key features of our vacuum chamber are the two large re-entrant vertical windows. A technical draw is shown in figure 3.3. They are a-magnetic 6mm thick CF100 viewports, made of Spectrosil, a synthetic fused silca produced by UKAEA. Their clear view is 60 mm. The transmitted wavefront error is $\lambda/8$ at 670 nm. They are anti-reflection (AR) coated (R<0.5%) at 323, 532, 670, 780 and 1064 nm. They have been designed in order to have the minimum

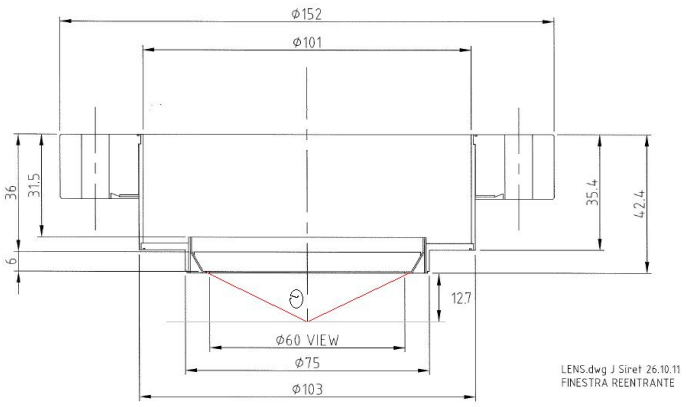

Figure 3.3: *Technical draw of the re-entrant vertical windows. The large clear view (60 mm) and their design provide a large numerical aperture.*

possible distance between their inner glass surface and the atoms working with 1" diameter MOT beams. Then the distance between the inner surface of the window and the center of the chamber is 12.7 mm meaning a minimum possible distance of the aspheric lens from the atomic cloud of 18.7 mm. The presence of the thick Spectrosil windows may introduce spherical aberrations that must be taken into account to design a proper imaging system. In the following we provide some details on spherical aberrations.

Optical aberrations

The fundamental ray-tracing formulas that can be found in standard optics text-book [36] are affected in reality by various kind of *aberrations*. The effect of spherical aberration of a lens is clearly visible in figure 3.4.

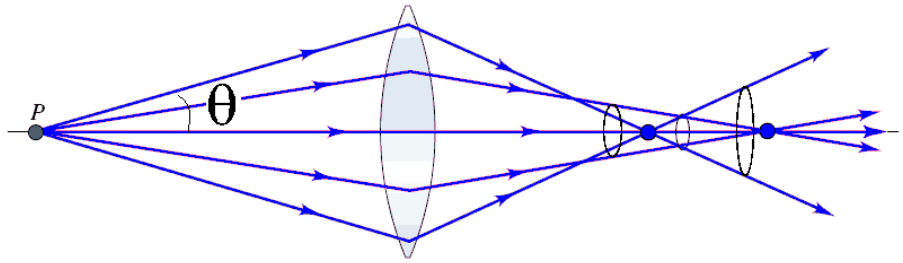

Figure 3.4: *Here we explicitly show the surface dependent effect of spherical aberrations: incident rays close to the lens axis are focussed in different position with respect to rays near its edge.*

Rays incident on different spot of the lens are focussed in different points along the axis of the lens. This results in bad reconstruction of the image, and of course in bad resolution. Particular surface shaped lenses are meant and designed to compensate for this position dependent effect. Aberrations can be described by expanding the sine of each angle in figure 3.4 into its power series $sin(\theta) = \theta - \frac{\theta^3}{3!} + \frac{\theta^5}{5!} - \frac{\theta^7}{7!} + \dots$ keeping the leading orders which significantly affect the image formation. The resulting equations give a reasonably accurate account of the principal aberrations. The differences between $sin(\theta)$ and θ are measures of spherical aberration and, therefore, of image defects. If one keep just the first order of the sine expansion, one gets the so called *first order theory*; if one keeps also the second term $\frac{\theta^3}{3!}$, the theory is said to be *third order*, and is affected by spherical aberration. Their derivation is beyond the interest of this work and can easily be found on text-books. On important result of this theory is that using a standard (non aspheric) plano-convex lens, would limit the resolution of

the imaging to spot diameters (SD) of

$$SD\ limit(third\ order\ theory) = \frac{0.067 \cdot f}{(\frac{f}{D})^3} \tag{3.1}$$

f being the focal length of the lens and D its diameter. This formula is valid for uniform illumination of the lens surface [37]. If we are interested in setting up an imaging system with a certain resolution, we should use this formula to select lenses with SD equal or smaller to the chosen one. In the next paragraphs we will describe the choice made by us. Before doing this, we give a fast description of the science chamber where the optics may be positioned.

3.0.5 Resolution test on aspheric lens

At the heart of the optical scheme is a high numerical aspheric plano-convex lens AL4532 with focal $f = 32$ mm and short working distance and large numerical aperture, $NA = 0.612$[2]. Such lenses have surface profiles which are not portions of either sphere or cylinder and their shape is such to compensate for spherical aberration while moving farther from the axis. A single aspheric lens can often replace a much more complex multi-lens system to reduce aberrations. The resulting device is smaller and lighter, and sometimes cheaper than the multi-lens design. The relevant experimental properties of the lens are reported in the following table.

model	f [mm]	WD [mm]	EFL [mm]	diameter [mm]	NA
AL4532	32	24.12	27	45	0.612

The given numerical aperture NA=0.612 of the lens gives an expected theoretical resolution of

$$R = 0.6\frac{\lambda}{NA} \sim \lambda \tag{3.2}$$

where λ is the wavelength of the incident light and is then the perfect choice for our case.

We also stress out here, that using a standard spheric lens with the same focal length and diameter, would limit its resolution according to equation 3.1 to $\sim 5\mu m$. We tested its resolution by shining He-Ne light (λ=632 nm) on objects of progressively smaller dimension -a grid of 10 μm spaced wires (Thorlabs

[2] A similar lens has been successfully used in the group of Prof. S.Jochim at Heidelberg.

model R1L3S3P), a pinhole of 5 μm (Thorlabs model P5S), a diffraction pattern of 1.6 μm spacing (CD Rom) and a sample with deposited 0.5μm size gold structures on it- and taking images of them. For these preliminary experiments a CCD (Thorlabs DCC1545M) of resolution 1280x1024 pixels has been used. The dimension of each pixel is 5.2x5.2 μm. Because of the multiple optical elements required along z to arrange the whole setup (WGP, dichroic, $\lambda/4$, window of the chamber), our resolution tests must take into account their possible effects on the image.

Grid

As a first test a 10μm spacing grid has been used. By simply shining light on the grid and positioning the lens after it at the working distance a fast check can be made on the resolution. Of course there is no true interest in imaging such large objects, but still it can be useful to get confidence with the system with an easy task.

Pinhole

We use a 5μm pinhole to characterize the resolution of the lens. To image the pinhole we must find an efficient way to align our optical imaging system. The pinhole is mounted on an x,y,z translator stage and can be moved arbitrarily in space. Here the basic idea of the scheme is to use the high focussing performance of the aspheric lens to produce a guide beam (2 in figure 3.5 a) with waist smaller then the aperture of the pinhole, therefore reducing the effect of diffraction. The

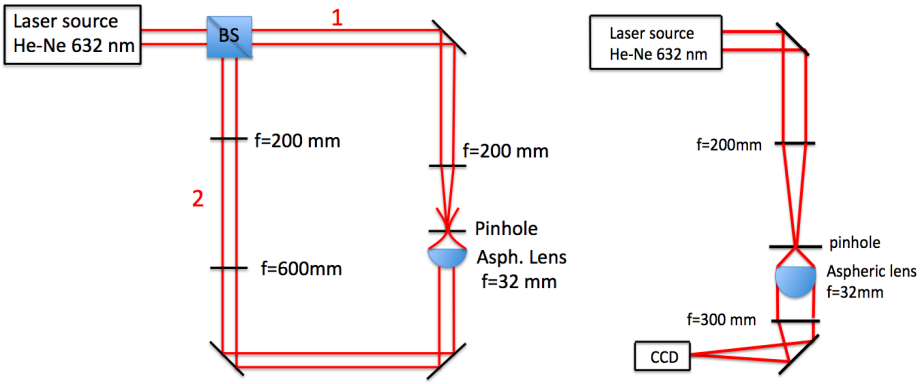

Figure 3.5: *On the left: scheme used to align the pinhole on the lens; on the right: X10 magnifying optical system used to image the pinhole size aperture; the f=200mm has been used to increase the light (thus the signal) that contributed to pinhole diffraction.*

strong suppression in the diffraction pattern[3] will manifest only near the focus, within an uncertainty of the order of the Rayleigh range. This implies that the pinhole is in the focus of the aspheric lens. Referring to figure 3.5, once beam 2 has passed through the pinhole it can also be used to align beam 1 on its path. The beam from the laser is initially split into two lines by a BS. Beam 1 shines the pinhole from its front side [4] while beam 2 passes initially through a telescope. The telescope is such to provide a beam waist in the focus of the aspheric lens (A) smaller at most of a factor $\frac{1}{\sqrt{2}}$ [5] with respect to half the pinhole aperture.

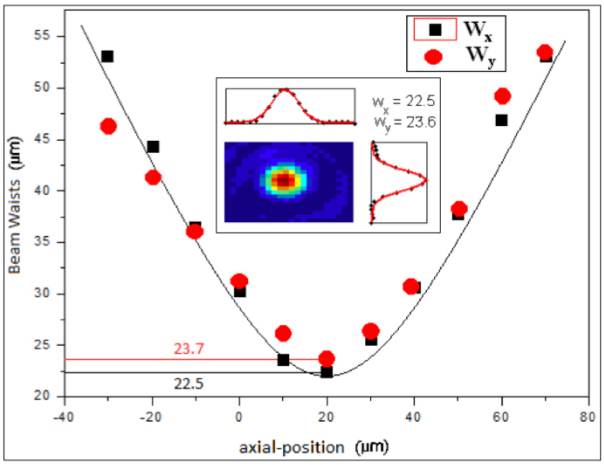

Figure 3.6: *The position of minimum of the waist is found to be about one Rayleigh range of distance from the starting position (origin) as expected. The error on the measurements is within the size of the data symbols. A transverse cut of the beam in the waist is shown in figure to clarify the meaning of w_x and w_y. We also report the gaussian fit (in μm) of the waists along both directions: it is compatible with a real size of the aperture respectively of $4.5\mu m$ and $4.7\mu m$, magnified 10 times. The error admitted by the company on the nominal aperture value of 5 μm is $\pm$ $1\mu m$ which is compatible with the measured aperture.*

This means that 'non diffracted' light will be only visible when the pinhole is 32 mm distant from the lens within an error of the Rayleigh range (z_R), while moving the lens away from the focus will rapidly cause a diffraction pattern to

[3] Of course diffraction will never be completely absent since the intensity profile is gaussian shaped, but can be reduced significantly.

[4] If necessary a lens can be used to focus the beam and increase the diffraction signal after the hole.

[5] The Rayleigh range is defined as the distance after which the beam radius increases by a factor $\sqrt{2}$

appear. The advantage now is that for such focussed beam, z_R is very small, and the resultant accuracy in the focusing is strictly bounded in all directions. In our case (see figure 3.5 b) the laser source has an initial radius of 1.2 mm. We used a telescope with magnification $\times 3$ to obtain a $\sim$3.5 μm beam diameter in the focus of the aspheric. The Rayleigh range is then $z_R = \frac{\pi w_0^2}{\lambda} \sim 15\mu m$. Once the pinhole is in the focus of the aspheric, we shine light from its front side and we can set up the optical magnification system. This is done by using lenses of high quality not to affect the resolution of the initial image. We used a two inches diameter achromatic lens with focal f=300 mm to magnify $\frac{300}{32} \sim \times 10$ the size of the pinhole. When the system is in the 'non diffracted' configuration,

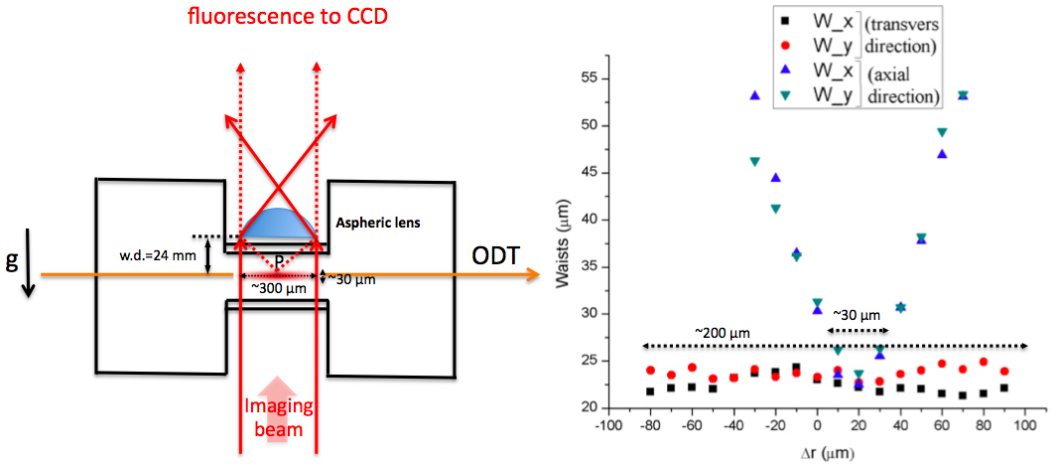

Figure 3.7: *On the left: schematic sketch of the atoms in the cigar shaped ODT. Some of them will necessarily be out of the focus of the lens. On the right: Sensitivity of the lens on the displacement Δr from the focus, measured by moving the pinhole along two spatial directions: axial and transverse. The error on the measurements is within the size of the data symbols. The slow oscillations in the transverse direction are most likely due to small misalignment of the beam on the pinhole aperture.*

we expect to be at a distance from the focus of $\sim z_R$. This is visible in plot 3.6 where the measured dimensions of the waist along the radial directions are reported as functions of the axial position of the pinhole. The origin signs the starting position found by looking the strong suppression in diffraction signal. The resolving image of the pinhole in focus is shown in figure 3.6. As can be seen the classical diffraction pattern from single aperture is not visible, that is the image is taken from the radiation field on the edge of the aperture, before diffraction takes place (near field). With a $\times 10$ magnification system of the 5μm

pinhole aperture we expect a measured waist of about 25μm, in agreement with what is shown in fig 3.6. To extract the size of the pinhole aperture, a gaussian profile is used to fit the counting on the CCD matrix. Since our optical dipole trap (ODT) is made of a single focused laser beam, as already said, it results in a cigar shaped cloud of atoms, meaning it is much longer in one direction with respect to the others. Thus, referring to figure 3.7, we want to test the resolution of this lens while we scan the point P along the cigar shaped cloud axis. On our testing table, P is substituted with the pinhole and we do the scan by simply moving the pinhole in the transverse plane, parallel to the surface of the lens. The results for these measurements are reported on the left side of figure 3.7. We observe basically no variation on the imaging resolution within a lateral extension of $\sim$200 μm.

This indicates that the lens conserves a good resolution even on objects which are misaligned with respect to the axis within a scale $>$100μm, thus allowing good detection on the entire elongated cigar shaped cloud.

CD gratings or "Commercial Diffraction" gratings

To further test the resolution of the aspheric lens we image the diffraction grating from a CD-Rom. A CD is built from a plastic (polycarbonate) substrate and a thin, reflective metallic film (24-carat gold or a silver alloy). The reflective

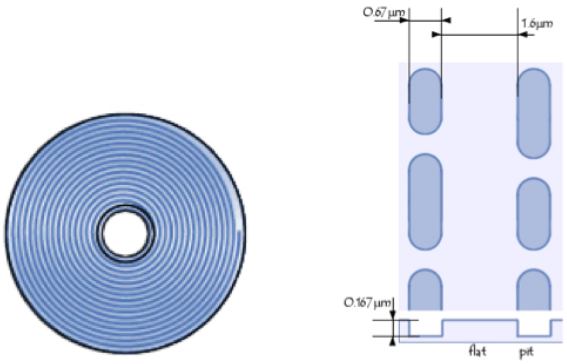

Figure 3.8: *Here is a basic sketch of the structure of a CD.*

layer is then covered with an anti-UV acrylic finish, creating a protective surface for data. Finally, an additional layer may be added so that data can be written on the other side of the CD as well. The reflective layer contains tiny bumps. When the laser passes over the polycarbonate substrate, light is reflected off the reflective surface, but when the laser reaches a bump, that's what allows it to decode information. This information is stored in tracks engraved in grooves

(or better a single long track spiralling inwards). In order to allow for an easier experimental configuration, we removed the reflective layer and observed the diffraction pattern in transmission of the CD. This method does not allow us to resolve in the image dark spots corresponding to bumps, since the reflection principle on which the CD works does not apply any more. Still, this allows us to observe the diffraction signal on a scale smaller then the one of 5μm, which is what we are just interested in at the very end. To perform an imaging of dark spots on the scale of $\sim 1.6\mu$ m, reflection measurements should be done on the surface of the CD, in near 180° back scattering configuration, which is clearly much more difficult to be implemented in laboratory. We can verify the diffraction signal coming from the CD is actually referred to a diffraction grating of the expected size, i.e. 1.6μm. This can be done just by remembering the rays law of diffraction $d\ (sin(\alpha) + sin(\beta_n)) = n\ \lambda$ which for normal incidence ($\alpha = 0$) reads as $d\ sin(\beta_n) = n\lambda$, d being the size of the grating (distance between two successive apertures), n the order of diffraction and α the angle shown in figure 3.9. The angle between the first order and the incident beam is

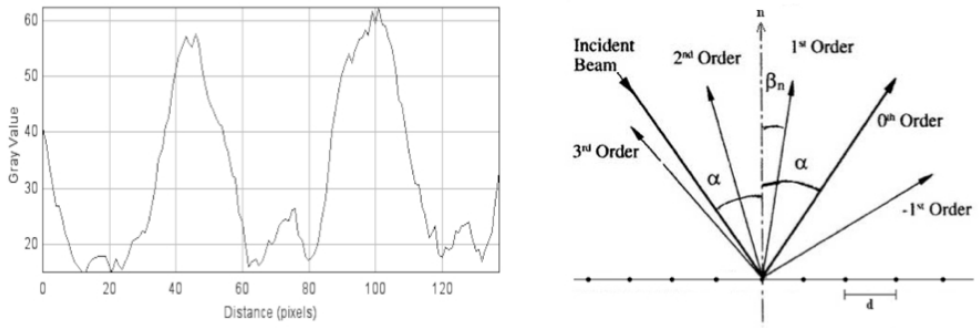

Figure 3.9: *On the left: slice of fringes originated by diffraction grating. Taken account of the ×20 magnification, the distance between the peak fringes (60 pixels) corresponds to a* $1.66\mu m$ *spacing. On the right: diffraction pattern of reflected light. The same situation is found if the incident beam is in transmission of the grating.*

directly related to the spacing between the arms of the spiral. This is measured to be 23°, perfectly consistent with the 1.6μ m spacing. We can then collect the diffraction pattern image (far field) on the camera and measure the spacing between the fringes. A cut of the fringes is shown in figure 3.9.

Gold spheres

Referring to figure 3.10 , to further test the resolution of the lens we implemented

a back scattering experimental setup using as sample, gold made structures of approximately 0.5μm size (below diffraction limit) deposited on the surface of a glass. Such structures scatter the light of wavelength 632nm and are then appropriate for our He-Ne laser source. Back scattering configuration allows

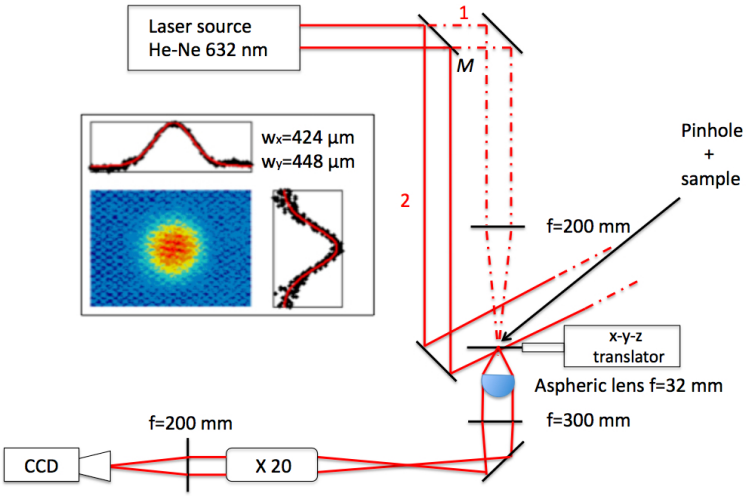

Figure 3.10: *The back scattering setup of the experiment is described. Very critical is having the pinhole mounted on a 3D-translational slit; useful could also be having the lens on one of them to allow micrometric alignment. In the squared picture we show the reference image of the 5 µm pinhole magnified 200 times.*

one to eliminate the signal of the laser pump and conserve just the scattered signal. The sample is prepared using a highly concentrated solution of gold spheres: a small chip is sandwiched between two glasses and the balls get stuck on the glass surface. To remove any other unwanted substance contained in the solution, water is flushed between the glasses. This usually cause these golden structures to dispose on almost straight lines along the direction of the water flow. In order to bring the optical system in focus, before the back-scattering configuration is implemented on the sample, we first take a reference image of the pinhole (of well known dimensions) with exactly the same configuration as before. The sample is glued on the top of its holder so that, once one has a clear image of the expected magnification of the system with the pinhole, then one can simply move along the vertical direction the pinhole and get at focus with the sample. In practice there is a marginal error of namely a couple millimeters due to the thickness of the holder's edge. A scheme of the experiment is shown in 3.10. Mirror M is used to switch between reference configuration (line 1) to

back scattering one (line 2). The optical imaging system is made of a first two

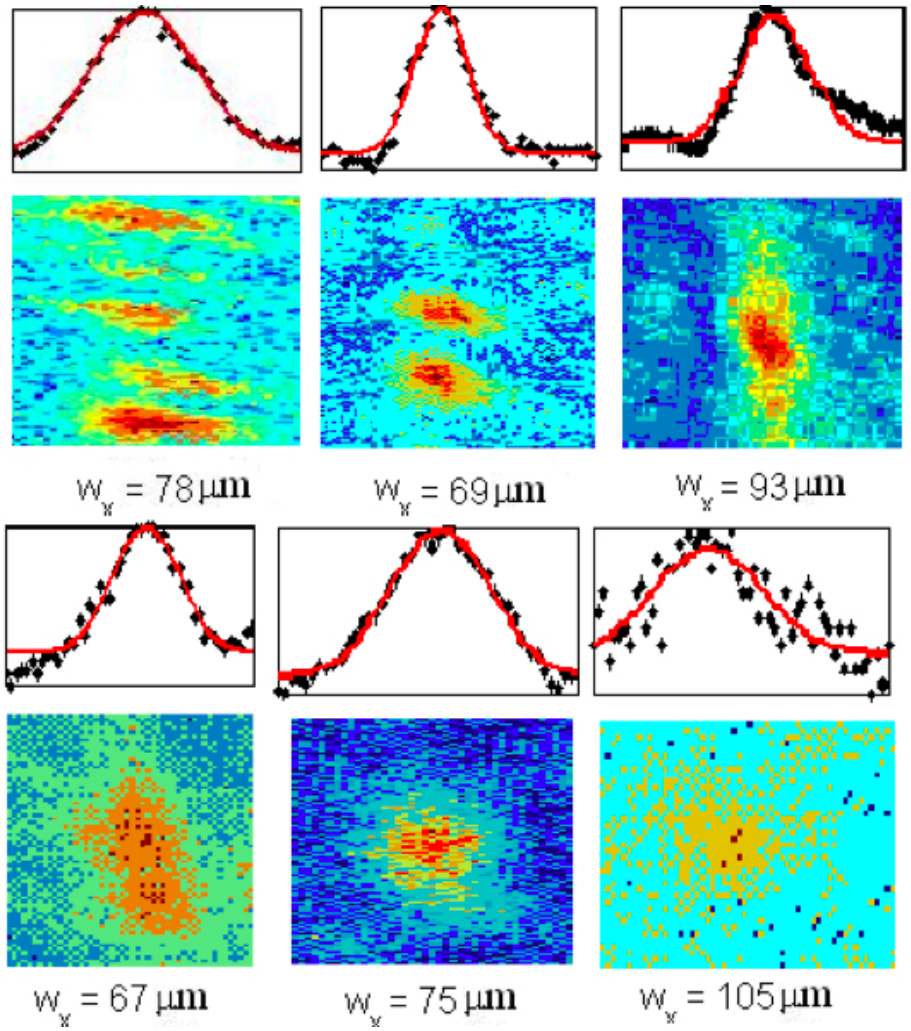

Figure 3.11: *Back scattering signals from the gold spheres detected on the CCD. Their imaged dimension, with a magnification of* $\sim \times 200$*, turned out to be about* $1\mu m$*. The ellipticity of some images is artificial and just due to image treatment: the scales along* x *and* y *may not be the exactly the same.*

lenses telescope with magnification $\sim \times 10$ ($f_1 = 32mm + f_2 = 300mm$) plus an objective that guarantees a magnification of $\times 20$ if a lens of focal f=200 mm is used to refocus the beam after it. The total magnification of the image on the CCD is then $\sim \times 200$. Because the dimensions of the golden balls are below the diffraction limit, we would expect to image them on the scale of $\lambda = 632nm$. With pixels of size $5.2\mu m$, this means an image on the CCD of $\frac{0.632 \times 200}{5.2} \sim 24$ pixels corresponding to dimensions of $24 \times 5.2 \sim 126\ \mu m$. With the same Gaus-

sian fitting procedure as before, we extract the radius of the spheres. Results are shown in figure 3.11. Sometimes it is clear that they arrange themselves in array as expected from the sample flushing procedure. The averaged measured dimension is found to be $81\mu m$ which means a resolution of $1.3 \times \lambda$, which is near the diffraction limit. We also report in figure 3.10 the reference image of the pinhole taken to confirm the optical system to be in focus. Importantly we found that WGP and dichroic mirror, together with the 6mm glass window, have little effect on the resolution of the presented imaging: still the scale of 1 μm seems to remain accessible. As reference, in figure 3.12, we also show an image of the background when the sample is dismounted. This ensures that the signal is coming from the sample and is not due to speckle in the room. One could wonder if the effect of the WGP and $\lambda/4$ wave plate is independent or not from their position with respect to the lens, meaning if the resolution is somehow different if we place them before or after it. In our case, due to the short working distance and the chamber design, we can only place them after the lens, where the MOT beams are diverging. Of course in principle one would prefer a setup where they are positioned before the lens, where the beam is still collimated, avoiding the problem arising from the damage threshold of the WGP. For this reason within the framework of these experiments, testing such

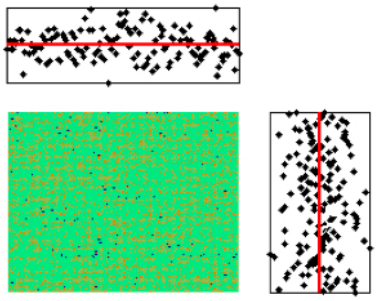

Figure 3.12: *Background signal by the light in the dark room. The fits do not show any interesting signal.*

dependence was considered of little relevance. In any case we performed these measurements just as a side notion when testing the sheet like beam for our thin barrier (refer to section 3.1).

3.1 Production of a thin barrier for double well potential implementation on ultra cold atoms

To observe and resolve the dynamics of fermionic systems, we are interested in implementing a barrier whose width is comparable with the interparticle spacing ($\sim \frac{1}{k_F}$) of the fermions in the trap. In the zero temperature limit, the Fermi energy $E_F = \frac{\hbar^2 k_F^2}{2m}$ can be calculated using eq. 1.17 with angular frequency $\bar{\omega} = (\omega_r^2 \cdot \omega_{curv})^{1/3}$ characteristic of our single beam optical dipole trap[6]. For $N = 10^4$ trapped fermions, we get $1/k_F \sim 0.5\mu m$: this approximately fixes the order of magnitude of the barrier we are interested in producing.

By means of a single cylindric lens, we succeeded in the realization of an anti-trapping potential barrier with spatial extension of $1.5 \times (> 1000)$ μm in the plane transversal to the direction of propagation of the focussed laser light. The Rayleigh range of the beam corresponding to the two directions is $(> 10^6) \times 25$ μm. We can then superimpose this sheet-like shaped barrier to our single focussed ODT beam to implement with very good approximation a double well potential with highly tunable properties.

Anti-Trapping potentials with laser light

As explained by eq.1.59, the sign of the light detuning with respect the atomic transition determines the nature of the potential experienced by the atoms, i.e if it is attractive or repulsive while the intensity controls the depth of the well ($\delta > 0$) or the height of the barrier ($\delta < 0$). As we pictured in figure 1.9, realizing an anti-trap requires a blue (detuned) trap: we choose green light (532 nm) . Our request is for a barrier being larger than the Fermi radius in two directions and extremely narrow (1.5 μm) in the third one (the axis of cigar), as a very long and thin sheet. The height of the barrier can be controlled through the intensity of the light.

The green laser used for testing is generated by a source[7] which is able to produce a maximum power of 5mW. The mode of the laser is cleaned by means of injecting the light into an optical fiber. The sheet-like shape is realized using a very simple optical scheme: the light out from the fiber is collimated to a gaussian beam of radius 5 mm and then passes into a cylindric lens of focal $f = 200$ mm; the resulting sheet-shape beam is focussed on the atoms taking advantage of the same aspheric lens ($f = 32$ mm) used for the high resolution

[6] Our ODT has $\omega_r \simeq 2\pi \times 250$ Hz and $\omega_{curv} \simeq 2\pi \times 20$ Hz - see next chapter or section 2.3 for further details.

[7] Model: Thorlabs CPS 532.

vertical imaging (AL4532). In this configuration we can squeeze the mode to obtain a highly focussed beam in one direction (~ 1.5 μm) while having a very broad waist onto the other (~ 800 μm). To characterize the optical properties

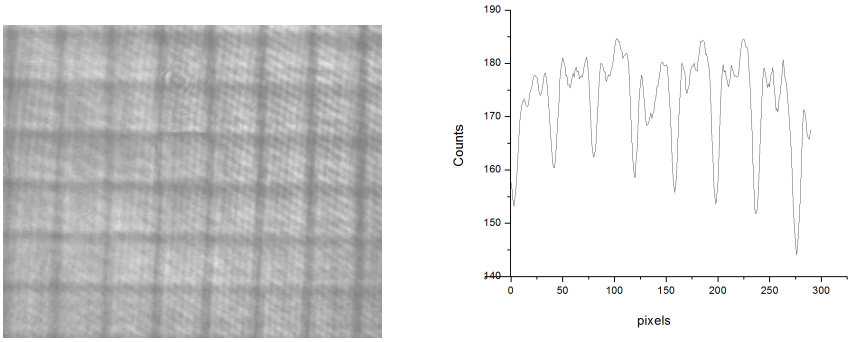

Figure 3.13: *A snap of the grid on the camera is shown (left) with a horizontal cut (right). The average distance between the wires has been measured to be approximately 10 μm.*

of the barrier, in particular the dimensions of the waist in the focus, we make use of a $\times 20$ imaging setup: to image the sheet-of-light in the focus of the AL4532 we use a microscope[8] (w.d.=32 mm) giving a magnification of $\times 20$ if a lens of focal $f = 200$ mm is used to refocus the beam after it. First of all we tested the goodness of the magnification power of the microscope using as reference a grid with known spacing (10 μm). The camera used for the test is the same used for the vertical imaging experiments. The image taken is shown in figure 3.13. Taking a horizontal cut of it we can extract the magnified spacing on the CCD in number of pixels, and knowing the dimension of the pixel, convert it in μm[9]: as can be seen on the right side of figure 3.13, the result of the cut confirms the $\times 20$ magnification. Then we proceeded in measuring the dimensions of the waist in the focus. The laser beam that enters the cylindric lens has a gaussian profile with waist of 1 cm. We injected the light in a fiber and used a collimator [10] to obtain easy collimation. The beam is than squeezed by the cylindric lens in the direction of its curvature while it is left unaltered along the perpedicular direction. It results in a sheet like beam which we then focus by means of the aspheric lens (see figure 3.14). We stress out that in both directions the beam stays approximately gaussian and so we can use at the zero order the well known

[8] Model: Mitutoyo M Plan Apo SL20x:378-810-3.

[9] As can be seen in 3.13 the spacing is about 45 pixels, which means a dimension in microns of about 40·5.2 μm = 208 μm, which is 20 times larger than the real spacing.

[10] Model: 60FC-T-4-M60-10, Shäfter-Kirchoff

relation for Gaussian beams to estimate the beam waist in the focus $w \sim \frac{\lambda f}{\pi w_0}$. According to this formula, large waists entering the aspheric will be focused much more than small waists. To measure w_x and w_y in the focus, in principle

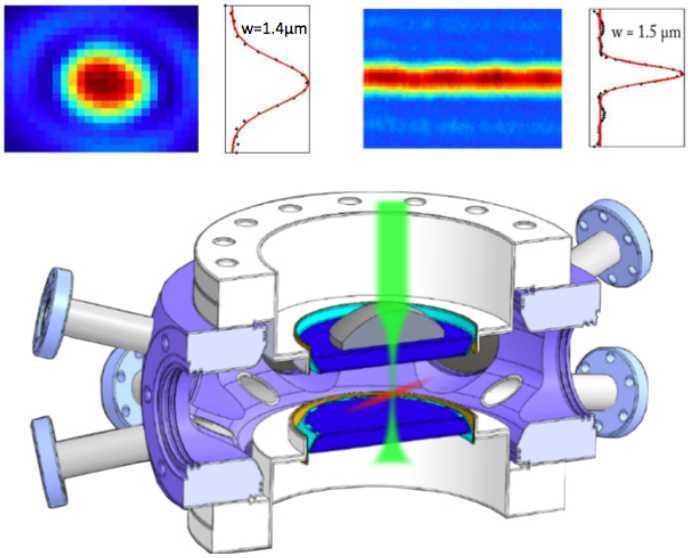

Figure 3.14: *On the top left: Beam shape before using the f=200 mm cylindric lens. On the top right: beam shape after its use.*

would be sufficient to shine the beam on the CCD screen and fit its shape along the two directions. This is feasible to do with the thin waist (w_y), but not that easy with the stretched one: it is in fact too long to fit the small CCD matrix. We used a razor blade mounted on a micrometric translator to gradually shutter the beam in its focus and simultaneously took measures of the decreasing power of the beam: we found $w_x \sim 800$ μm. We also tested the effect on the waists of

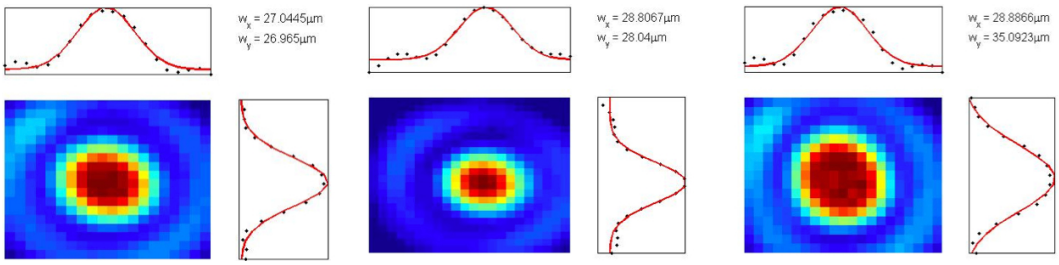

Figure 3.15: *On the left: Reference image of the beam in the focus without WGP. In the center: beam waist with WGP before the aspheric (planar side). On the right: beam waist with WGP after the aspheric (convex side).*

interposing a WGP on the path of the green light before and after the aspheric lens, to check possible differences in focusing power or focus shape. The test was made without the cylindric lens. We found that WGP does not really affect the focal properties of the system, as shown in figure 3.15. We also checked the sensitivity of the waists dimensions on the position of the cylindrical lens. We found a substantial independency of them, which turns out to be very useful allowing more flexible design of the experimental scheme. Substituting eq. 1.73 in equation 1.59 the potential barrier is proportional to

$$U \sim \frac{P}{w_x w_y} \tag{3.3}$$

meaning that highly focused light in one direction results in a high barrier, even for low power of the laser used. In particular for our values of the waists and using a 100 mW laser source we are able to produce a barrier of height $\sim$2 μK, larger then the Fermi energy which, for typical parameters, is of the order of hundreds of nK.

Chapter 4

Quantum Degeneracy of ^6Li

As we have seen in chapter 2, the initial temperature of the cloud in our MOT is $\sim 1mK$. Since we want to exploit an all-optical trapping method to produce superfluid Fermi gases, we need to reduce the temperature of the atoms to hundred μK before the evaporation stage. Indeed an effective loading in the optical trap requires a ratio $\eta = \epsilon/k_B T \simeq 10$ where ϵ is the depth of the trap and T the temperature. In fact, as we are going to explain in the following, the maximum trap depth of our single focussed ODT is of the order of 5 mK. Furthermore since the ODT waist is limited to $\sim 30\mu m$ we need also to spatially compress the cloud. Such achievements are obtained by performing two different cooling stages, namely D2 and D1 cooling stages. While the first one is routinely applied in many experiments of this kind, the second one is applied for the first time on ^6Li[1]. We will show that using these two cooling stage we can decrease the temperature to about 50 μK and increase phase-space density of one order of magnitude (10^{-5}). These values are the optimum starting point to proceed with the successive trapping and evaporation into our ODT.

4.1 Experimental cooling sequence

4.1.1 D2 Cooling Stage (CMOT)

We optimize the MOT loading with a detuning of $\sim -3.5\Gamma$, allowing a larger capture range of the MOT and an overall faster loading. Nevertheless, for such parameters the temperature of the ^{6}Li cloud is still pretty high (of the order of 1 mK). Thus an additional cooling stage is required. On the D2 transition line,

[1] D1 cooling stage is actually applied and proposed by C. Salomon group at ENS on Potassium40 and Li7.

this stage is performed reducing the powers of both the repumper and cooling lights to about 20%. This procedure reduces the overall rate of photon-atom scattering (see eq. 1.61), thus resulting in a net reduction of the temperature and in an increase of the density of the cloud. In addition, just before the full transfer into the optical trap and the switching off of the MOT beams, we bring the detuning of the cooling light to about $-\Gamma$ where an experimental minimum of the temperature is achieved (see eq. 1.68) and we increase the gradient of the quadrupole field of the MOT up to $\sim 35G/cm$. This last stage must last no longer than a couple of milliseconds, after which, light-induced losses begin to occur due to the increase of the density[2]. Reducing the intensity of the repumper light is also very critical since this light is necessary to keep the atoms in the MOT: indeed, atoms will not stay trapped without it, falling in the dark ground state $|F = 1/2\rangle$, scaping from the cooling cycle, and thus from the MOT. The last sequence of this stage is the loading of the ODT: while we ramp the power of the ODT-laser to its maximum value ($\sim$ 170W) we abruptly reduce the powers of both repumper and cooling to almost zero. In particular we perform *hyperfine pumping* to the lowest hyperfine state $|F = 1/2\rangle$ by means of turning off the repumper light few hundreds of microseconds before the cooling light: here they don't scatter anymore with photons and are able to achieve temperatures of about 200 μK.
At the end of the D2 cooling stage we obtain a sample of $\sim 5\times10^8$ atoms at 200 μK occupying the fundamental ground state F=1/2. The atoms equally populate the two lowest Zeeman sub-levels $|F, m_F\rangle = |1/2, -1/2\rangle$ and $|F, m_F\rangle = |1/2, +1/2\rangle$ creating a mixture of non identical fermions ready for evaporative cooling.

4.1.2 D1 optical molasses

D2 transition is widely used in laser cooling schemes since it has a closed optical transition ($|^2S_{1/2}, F = 3/2\rangle \rightarrow |^2P_{3/2}, F = 5/2\rangle$). However for ^{6}Li, standard sub-Doppler cooling techniques does not work efficiently because of the small separation between the hyperfine states of the $^2P_{3/2}$ atomic level [38]. In fact , the transition linewidth ($\sim$5.4 MHz) is of the same order than the separation between the hyperfine states ($\sim$ 4.4 MHz). To reduce furthermore the temperature of our cloud we perform an additional cooling stage using the D1 transition ($2^2S_{1/2} \rightarrow 2^2P_{1/2}$), as already demonstrated in previous works on different atoms [34, 39]. As we said, the D2 and D1 optical transitions are separated by

[2]Multiple scattering of photons may occur resulting in an increasing of the temperature.

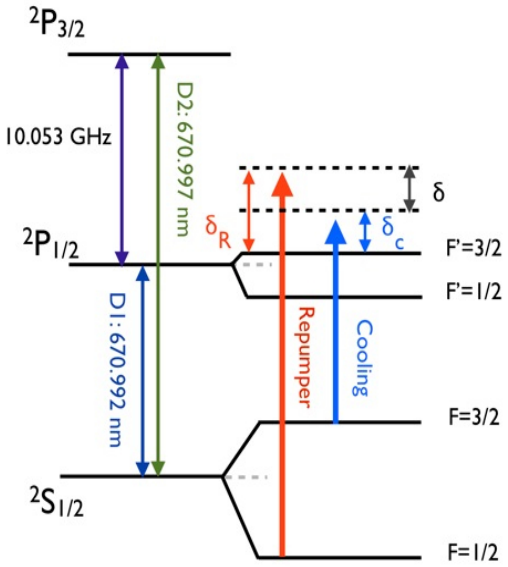

Figure 4.1: *Scheme of the D1 transition line showing both cooling and repumper frequencies.*

about $\sim$ 10GHz. To generate the D1 lights (cooling and repumper frequencies as shown in figure 4.1), we use another solid state amplified laser source TApro from TOPTICA equal to the one used for the D2 setup. This laser is able to generate a power up to 400 mW. As we already discussed previously the D1 laser is frequency locked on the D2 laser via an offset lock scheme at 10 GHz. The optical scheme is shown in figure 2.3. Another important characteristic of our scheme is that it allows to use the same amplifiers for both optical lines, significantly simplifying the optical setup and reducing costs. By means of two independent switch AOMs we can turn on and off the two cooling stages independently. Indeed they are performed at different times to avoid overloading of the MOPAs.

Parameters	Experimental optimal values
δ_C	$+5.2\ \Gamma$
δ	$+0.08\ \Gamma$
I_C	$8\ I_{sat}$
I_R	$1.2\ I_{sat}$
t_{mol}	$2\ ms$
T_{min}	$\sim 40\ \mu K$

Table 4.1: Optimal values of the D1 cooling stage.

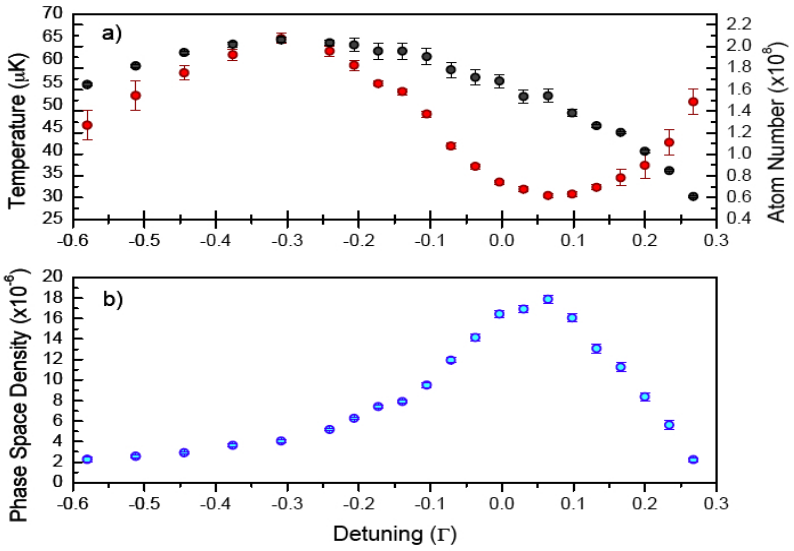

Figure 4.2: *Upper panel: In red we report the temperature of the atomic cloud. We obtain an absoulte minimum corresponding to an absolute detuning of* 0.6Γ. *In black we over-plot the corresponding number of atoms. Lower panel: Phase-space density calculated from the experimental points of the upper plots.*

Without entering into details -see [34]- this cooling stage combines a gray molasses of $\sigma^+ - \sigma^-$ polarized beams: both are detuned from the $|F = 3/2\rangle \rightarrow |F' = 3/2\rangle$ transition (cooling) and the $|F = 1/2\rangle \rightarrow |F' = 3/2\rangle$ transition (repumper), respectively by δ_C and δ_R. With this scheme it is possible to create dark states at the two-photon resonance. In particular we observe a strong influence of the relative detuning between the two cooling lasers and a strong decrease of the temperature of the cloud. The optimal parameters are reported in table 4.1. The characterization of the cooling scheme was performed by tuning the different parameters of the beam and measuring the temperature of the atoms via TOF (Time-of-Flight) imaging. After a D2-CMOT cooling stage of 25ms[3], the D1 stage is performed. While the magnetic field of the MOT is turned off, the MOT lights are substituted with the D1 molasses by means of fast AOMs switch. The cooling in the D1 molasses lasts $\simeq$ 2 ms. After it, absorption imaging after 11 ms of TOF is performed to extract the temperature of the cloud. Indeed a free expansion of the cloud leads to a broadening of the gaussian density profile of the cloud, according to

$$\sigma^2(t) = \sigma_0^2 + \langle v^2 \rangle t^2 \tag{4.1}$$

[3]Not including the changing in detuning of the cooling light to $-\Gamma$.

where $\sigma(t)$ is the width of the cloud at time t and $\sigma_0 = \sigma(t = 0)$. Since the average velocity for a thermal gas can be related to the temperature via equation $\frac{1}{2}m\langle v^2\rangle = \frac{1}{2}k_BT$, the temperature of the system can be extracted as $T = \frac{m}{k_B}\left(\sigma^2(t) - \sigma_0^2\right)/t^2 \simeq \frac{m}{k_B}\sigma^2(t)/t^2$ for TOF > 10 ms. In figure 4.2 we report the behaviour of the number of atoms and temperature versus the absolute detuning δ referred to the optimal values shown in table 4.1. As shown in figure 4.2, we can achieve temperatures as low as $\sim 30\mu$K for a cloud of about 10^8 atoms. We also calculated the corresponding phase-space density which is significantly increased thanks to this stage of about one order of magnitude, approaching 10^{-5}.

4.1.3 Single beam optical dipole trap

Our dipole trap is produced by a single polarization multimode laser[4] at 1070 nm, with a maximum output power of 200W. The trap is a FORT (far-of-resonant-trap) made by a single focused red-detuned gaussian beam. The intensity of the laser is controlled by an AOM which allows both the switch on and off of the power and its continuos control. The intensity is actively stabilized using a PID[5] control through a logarithmic photodiode. As shown in figure 2.8 the laser enters into the chamber with an angle of $\sim 15°$ with respect to the MOT beams. The parameters of our trap at maximum power are:

w$[\mu m]$	$z_R[mm]$	$P_{loading}[W]$	$U_{loading}$ $[mK]$
$\sim$31	2.8	150	$\sim$5

The maximum depth of the trap, allows efficient loading of the atoms directly from the MOT and provides good conditions for evaporative cooling. If the depth of the trap is higher compared to the thermal energy of the gas, it will trap the cloud. In the case of lithium 6 magnetic traps can not be used due to the high field seekers nature of the states $|1\rangle$ and $|2\rangle$ which are necessary to have good collisions rate at low temperature to perform evaporative cooling.
A single focused beam trap, has intensity profiles along the axial and radial directions respectively of $I \sim e^{-\frac{x^2+y^2}{w^2}}$ and $I \sim e^{-\frac{z^2}{z_R^2}}$ where z_R is the Rayleigh range of the beam and w the beam waist of the beam. Thus, as can be seen from equation 1.59, the radial and axial trapping frequencies scales with the intensity of the beam respectively as $\omega_r \sim \sqrt{I}$ and $\omega_{ax} \sim \sqrt{I} \cdot \frac{w}{z_R}$. Thus ω_{ax} is smaller then ω_r by a factor $\frac{w}{z_R}$. At low intensity the axial confinement ($\propto \omega_{ax}^2$) is not

[4]Model:YLR-200-LP-WC, IPG Photonics.
[5]Model: SIM 960 from SRS.

enough to keep the atoms in the trap. For these reasons, as we already discussed in section 2.3, we superimpose a magnetic curvature to the optical potential. We make use of both Feshbach coils and curvature coils which give a total confinement defined by a frequency of $2\pi \cdot 18$ Hz at 834 G. The anti-curvature along the axis of the coils is sensitively smaller then the optical confinement even at low intensities and therefore can be neglected.

Astigmatism: It is important to say that we took care of designing and aligning the optical path to suppress the astigmatism of the ODT beam. Indeed we found an extremely sensitive dependence of the astigmatism on the centering of the optics. For this reason in our optical scheme almost all our lenses have two inches of diameter and all the reflections of the beam on the mirrors are of 45° or 0°. This provides a better quality of the beam, reducing significantly the astigmatism to values $< 100\mu$m. Furthermore to reduce the thermal lensing we use Suprasil 3001-made lenses [6].

4.2 Molecular Bose-Einstein condensate of ^6Li

The first experiment performed with our machine is the production of a molecular Bose-Einstein condensate (mBEC) of ^6Li atoms in a 50%-50% mixture of $|1\rangle$ and $|2\rangle$ states. We evaporative cool our atomic cloud at 804 G, starting from a potential depth of few mK to a final value of 0.4 μK. In particular we can produce a BEC of about $50 \cdot 10^3$ molecules with a condensed fraction up to 85%. In the following paragraphs we describe briefly the experimental procedure to obtain quantum degeneracy.

4.2.1 Properties of mBEC

Molecules begin to form in the cloud as soon as its temperature becomes comparable with the binding energy of the molecules ($k_B T \sim \frac{\hbar^2}{ma^2}$). For the offset value $B = 804$ G this means molecules begin to form at ~ 200 nK.
Above the transition temperature (T_c) the density of the thermal gas can be conveniently be described by a gaussian distribution profile. When the temperature is reduced below T_c, the bosonic nature of the molecules manifests as they condense into a Bose-Einstein condensate. For $na^3 << 1$, the density distribution of a interacting BEC of particles can be extracted by solving the time-independent Gross-Pitaevskii equation [40]:

$$\Big(\frac{\hat{p}^2}{2m} + V_{ext}(\mathbf{r}) + g|\Psi(\mathbf{r})|^2\Big)\Psi(\mathbf{r}) = \mu\Psi(\mathbf{r}) \tag{4.2}$$

[6] From LaserComponents Germany.

where μ is the chemical potential of the gas. Here the mean-field interaction is proportional to the density $|\Psi(\mathbf{r})|^2$ and $g = 4\pi\hbar^2 a/m$. When the kinetic energy of the particles (ultra-cold limit) is much lower then the interaction term, Thomas-Fermi approximation applies and eq. 4.2 yields to the simple solution for the spatial density:

$$n_{BEC}(\mathbf{r}) = |\Psi(\mathbf{r})|^2 = max\Big(\frac{\mu - V(\mathbf{r})_{ext}}{g}, 0\Big). \tag{4.3}$$

This may be thought as the condensate filling the bottom of the trap up to the value of the chemical potential. For harmonically trapped clouds [35] one finds the shape of an inverted parabola where the size of the condensate is given by the so called Thomas-Fermi radius $\bar{R} = (\frac{2\mu}{m})\Big(\frac{1}{\omega_x^2\omega_y^2\omega_z^2}\Big)^{1/3}$ where the wavefunction of the BEC goes to zero. As the cloud is released from the trap and expands

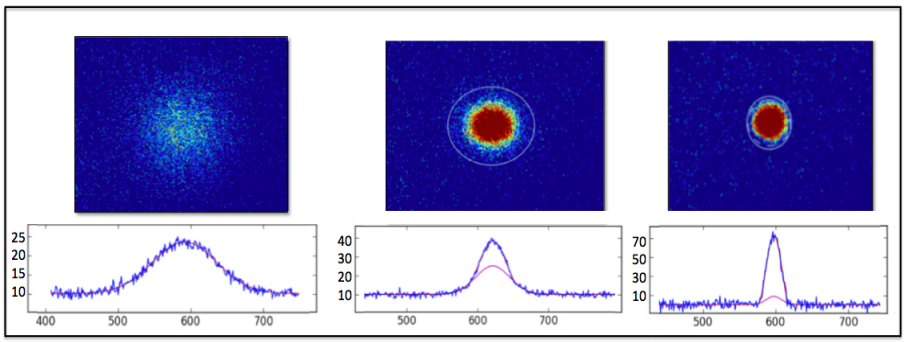

Figure 4.3: *Bimodal distribution is the clear evidence of the formation of a Bose-Einstein condensate in our gas. Here the Thomas Fermi profile clearly emerges from a thermal (gaussian) distribution. The gas is imaged by absorption imaging after 5 ms of TOF.*

freely, the interaction energy is converted in kinetic energy: since interaction depends on the density, in an anisotropic trap, the stronger the confinement the faster the expansion. As soon as condensation occurs the Thomas Fermi profile emerges from the gaussian profile of the thermal cloud (see figure 4.3). Time-of-flight measurements are thus appropriate for the experimental detection of condensation through bimodal distribution of the density profile. The critical temperature of a non-interacting Bose gas harmonically confined is given by:

$$T_c = (0.94)\frac{\hbar\bar{\omega}}{k_B}N_{mol}^{1/3} \tag{4.4}$$

where $\bar{\omega} = (\omega_r^2\omega_{axial})^{1/3}$ for a cigar shaped trap.

4.2.2 Experimental sequence

As first step we transfer the atoms from the MOT into our optical dipole trap: as we ramp the power of the ODT laser from 0 to 150W, we perform the D2 cooling stage (CMOT) discussed above. At this point we are not using the D1 cooling stage, since the merging of the atomic cloud with the ODT is still not optimized. The use of the D1 cooling stage to improve the ODT loading will be done in the near future. We are able to transfer 1% of the atoms of the MOT into the ODT. Even if the transfer is not so efficient, we obtain 10^6 atoms per spin state ($|1\rangle$ and $|2\rangle$) which are enough for our goals. We estimate the temperature to be of the order of hundreds of μK. The experimental sequence is shown in details in figure 4.4. Immediately after the transfer in the optical trap

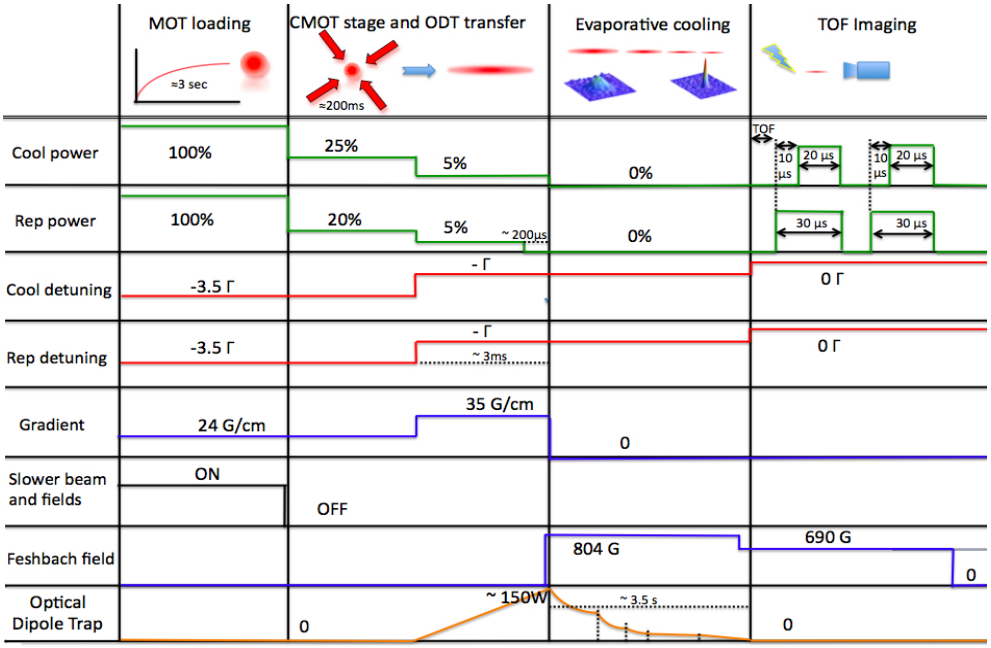

Figure 4.4: *Experimental sequence showing the timings of the cooling sequence.*

we tune the magnetic field close to the Feshbach resonance at a value of 804 G: here the scattering length is approximately $15000 \cdot a_0$ (a_0 being the Bohr radius) and collisions are strongly enhanced. Evaporation is much more efficient if the scattering rate of the atoms stays high enough to allow atoms to exchange and redistribute energy in the cloud quite fast in time. Indeed, from eq. 1.38, the scattering rate is approximately given by:

$$\Gamma = n\sigma\langle v\rangle \sim n\ 4\pi a^2 \sqrt{k_B T/m} \tag{4.5}$$

being n the density of the gas, $\sigma \simeq 4\pi a^2$ its scattering cross section far from the resonance[7] and $\langle v \rangle \sim \sqrt{T}$ the average scattering velocity. The density n

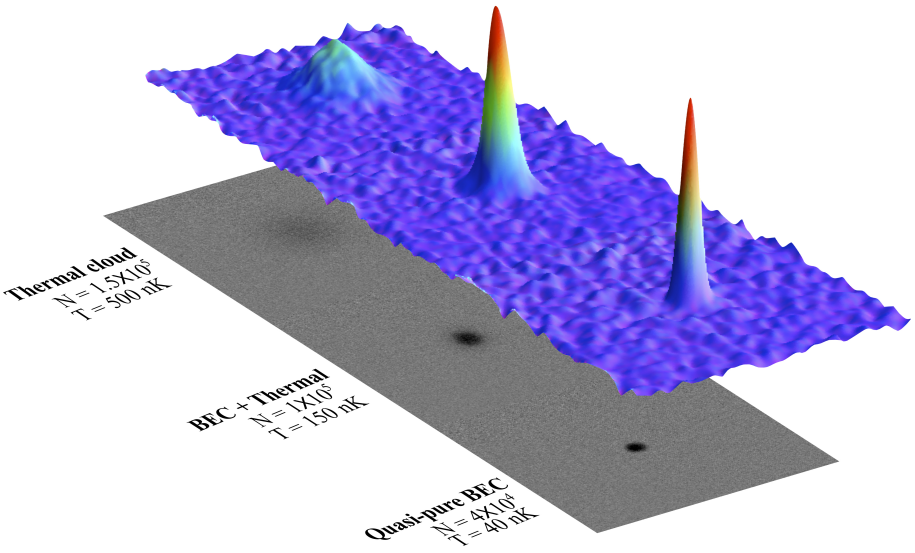

Figure 4.5: *Bose Einstein condensation of molecules. The picture shows three 5ms TOF images of the cloud distribution, taken at different times along the last ramp of the evaporation stage. Thomas Fermi profile arises from a thermal cloud.*

in direction x_i actually depends on both the temperature and on the harmonic confinement as

$$n(x_i) \sim e^{-m\frac{\omega_i^2 x_i^2}{k_B T}} \tag{4.6}$$

where $2\pi\omega_i$ is the trapping frequency along the direction x_i[8]. The magnetic field is ramped from zero up to 804 G in 20 ms. We then perform evaporation using four successive ramps till a final trap depth of 0.4μK. The temperature of the system after the last evaporation ramp is so low that molecules condense as soon as they are formed in the gas. To observe a mBEC we perform a fast sweep (20 ms) to 690 G: here the interaction energy is lower and allows a better observation of the bimodality of the cloud (see figure 4.3). Imaging is performed by simply releasing the atoms from the trap: the free expansion of the cloud can be imaged in TOF, allowing easy detection of its density profile. The BEC formation appears as a Thomas-Fermi distribution (inverted parabola) centered on a gaussian thermal profile. In figure 4.5 we can see the Thomas-

[7] Valid for $(ka)^2 << 1$.

[8] Here we stress out how the magnetic axial curvature we use to increase the axial density, results in a good scattering rate and in a subsequent efficient evaporation.

Fermi profile emerging from a thermal gaussian cloud. From eq. 4.4 we estimate the critical temperature to be T_c=190 nK. The measured temperature on the residual thermal fraction after the last ramp results of 40 nK and is compatible with a condensated fraction larger than 90%.

Chapter 5

Conclusions

During the period of my thesis at LENS my main research activities have been focused on two main directions: from one side I realized optical schemes to tailor light potentials that will be used to manipulate superfluid Fermi gases. In particular I developed a new optical setup to produce and imprint thin sheet-shaped barriers on the atomic cloud. I have also designed and realized an optical scheme to image the atoms with high resolution ($\sim 1\mu$m) approaching the diffraction limit. Both these tools are now ready to be implemented on the experiment.

Moreover, on the present apparatus, I implemented a completely new cooling scheme for the first time realized on ^{6}Li atoms, that allows the reduction of the MOT temperature to $\sim 40\mu$K, far below the standard Doppler limit of 140μK.
I have also characterized the final cooling stage of lithium atoms in the optical dipole trap (ODT) which eventually allowed the observation - on the positive side of the Feshbach resonance - of molecular Bose-Einstein condensate of ^{6}Li atoms. The number of condensed molecules is $N_{mol} \sim 5 \cdot 10^4$ with a final condensed fraction larger than 90%. This is the first step toward the production of strongly interacting Fermi gases at the BEC-BCS crossover.

The future perspectives of this work are:

- merging the new D1 cooling stage with the evaporation stage in our dipole trap. We are confident that the lower initial temperature will allow a better loading in the ODT and thus a more effective evaporative cooling to quantum degeneracy. The faster and more efficient production of superfluid gases of fermions, thanks to the combination of all optical traps and

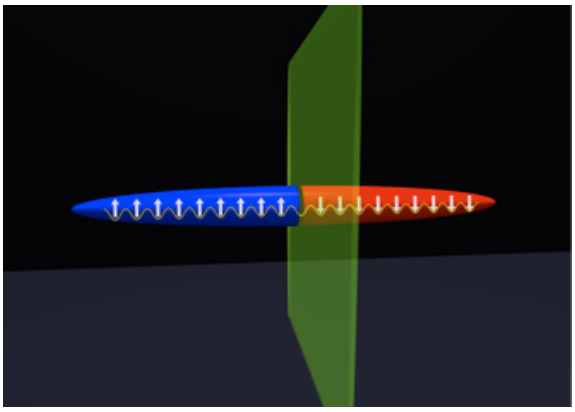

Figure 5.1: *Sketch of the cigar-shaped atomic sample cut by a thin optical barrier. We prepare two-component degenerate Fermi gases of ^6Li and we then separate the two states by applying a combination of a magnetic field gradient and a barrier. We study the spin dynamic while lowering the barrier for different regimes of interaction.*

D1 cooling, is of worldwide interest in the ultra-cold atoms community. This step is actually under implementation in the present days. In addition it would be possible to use the D1 cooling to perform single-site addressing in optical lattices preventing the light lithium atoms to escape from the lattice sites during the fluorescence measurements [41, 42].

- implementation of thin barriers on the cigar shaped atomic cloud to study the spin transport properties of a fermionic gas across different regimes of interaction. In particular we may address two physical situations: the first one concerns the experimental investigation of the ground state of a repulsive Fermi gas (Stoner model), which was first theoretically demonstrated in 1933 to be ferromagnetic [43]. This model finds one possible realization in the study of a two-spin-component atomic Fermi gas close to a Feshbach resonance [44]. So far, three body recombinations, leading to molecules formation, hinders a clear experimental evidence of such phase. It has been recently suggested [45] that the combination of a cigar-shaped trap, i.e. with large aspect ratio, with the addition of an optical lattice (fig.5.1), may stabilize the ferromagnetic ground state, allowing for its experimental detection. In our system we could easily implement this theoretical proposal, opening the possibility of studying still unexplored phases.
  The second one is the study of Josephson tunneling of paired fermions

across the barrier. This experiment mimics the ordinary superconducting junctions. By studying the dynamic in this double-well potential, we can measure the superfluid gap as done in ordinary superconductive systems [46].

The experimental study of the Josephson effect with a superfluid Fermi gas through optical barriers is still an unexplored research topic. Only recently [47], it has been reported the first observation of solitons generated by phase imprinting on superfluid Fermi gases at resonance .The two phenomena are deeply connected and rely on the nature of the superfluid wavefunction. The theoretical description of such strongly-interacting systems at finite temperature is still to be developed. We think that the implementation of our experimental scheme could trigger even more the research in this area, creating the conditions required to develop new theory and to promote new experimental investigations.

Appendix A

Acousto-optic-modulator

We use AOM to tune the frequency of the light. They take advantage of the photon-phonon interaction to deflect the angle and change the frequency of an incident photons beam. The scattering process can be described diagrammatically as shown in figure A.1. By absorbing N phonons with wavelength Λ, the photon changes both its direction and energy (λ) according to

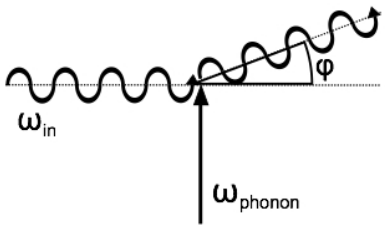

Figure A.1: *Diagrammatic representation of photon-phonon interaction.*

$$\omega_f = \omega_i + N\omega_{phonon} \tag{A.1}$$

$$sin(\phi) = \frac{N\lambda}{2\Lambda} \tag{A.2}$$

An AOM is basically made of a transparent crystal whose refractive index can be modulated through a piezo crystal driven by a radio frequency signal who is able to generate mechanical stress on the medium. We can separately operate on the amplitude and the frequency of the scattered light by changing the RF and its amplitude. Because of the deflection of the incident beam we can also use AOMs as fast optical switch. This is done both on D1 and D2 lines. Each AOM can be controlled with amplitude modulation (AM) and frequency modulation (FM) analogic signal and with digital TTL signal.

Appendix B

Coils scheme

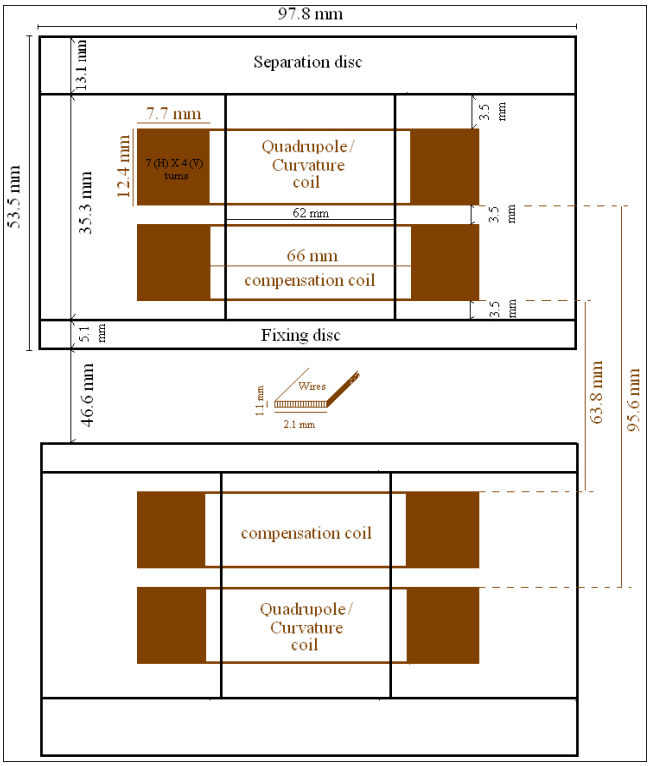

Figure B.1: *Scheme of the coils placed inside the re-entrant windows of the science chamber. The holder of these coils is done by polyether ether ketone plastic (PEEK), a thermoplastic with excellent mechanical and chemical resistance properties kept also at high temperatures. The PEEK melting temperature of about 350 C. In these supports the coils are immersed in fluxing water to assure their correct cooling during the normal operation.*

Bibliography

[1] Feynman R.P. Simulating physics with computer. *International Journal of Theoretical Physics*, 21((6/7)):467–488, 1982.

[2] Trabesinger A. et al. Nature physics insight: Quantum simulation. *Nature Physics,*, 8(4):262–299, 2012.

[3] Zwerger W. Bloch I., Dalibard J. Many-body physics with ultracold atoms. *Review of Modern Physics*, 80(4):885–964, 2008.

[4] M.Messer D.Greif W.Hofstetter U.Bissbort T.Uehlinger, G.Jotzu and T.Esslinger. Artificial graphene with tunable interactions. August 2013.

[5] C.Chin R.Grimm P.Julienne E.Tiesinga. Feshbach resonances in ultracold gases. *Rev. Mod. Phys.*, 82:1225–1286, 2009.

[6] M.W.Zwierlein and W.Ketterle. Making, probing and understanding ultracold fermi gases. In *Proc. of the International School of Physics "Enrico Fermi" edited by M.Inguscio, W.Ketterle and C.Salomon*, number CLXIV, Varenna, 20-30 June 2006. (IOS Press, Amsterdam, 2008).

[7] Leggett A.J. *Quantum Liquids: Bose Condensation and Cooper Pairing in Condensed-Matter Systems.* Oxford Graduate Texts, 2006.

[8] Qijin Chen Jelena Stajic Shina Tan and K. Levin. Bcs-bec crossover: From high temperature superconductors to ultracold superfluids. *Physics Reports*, 412(1):1–88, 2005.

[9] Modugno M. Wiersma D.S. Fort C. Inguscio M. Lye J.E., Fallani L. Bose-einstein condensate in a random potential. *Physical Review Letters*, 95(7):070401, 2005.

[10] M.Inguscio A.Aspect. Anderson localization of ultracold atoms. *Physics today*, 62(8):62, 2009.

[11] E.M.Lifsits L.D.Landau. *Quantum Mechanics: Non-Relativistic Theory.* Butterworth Heinemann, 1977.

[12] Kerson Huang. *Statistical Mechanics.*

[13] S.Stringari Lev Pitaevskii. *Bose-Einstein Condensation.* Clarendon Press, Oxford, 2003.

[14] Jun John Sakurai. *Modern Quantum Physics.* 2009.

[15] C.J. Pethick and H.Smith. *Bose-Einsten Condensation in Dilute Gases.* 2002.

[16] P.Massignan M.Zaccanti G.M.Bruun. Polarons, molecules, and itinerant ferromagnetism in ultracold fermi gases. 2013.

[17] C.A. Sackett E.R.I. Abraham, W.I. McAlexander and Randall G. Hulet. Spectroscopic determination of the s-wave scattering length of lithium. *Phy.Rev. Lett.*, 74,(8), 1995.

[18] J.M. Gerton E.R.I. Abraham, W.I. McAlexander and R.G. Hulet. Triplet s-wave resonance in ^6li collisions and scattering lengths of ^6li and ^7li. *Phy. Rev. A*, 55(5), 1997.

[19] G.Zurn T.Lompe A.N.Wenz S.Jochim P.S.Julienne J.M.Hutson. Precise characterization of 6li feshbach resonances using trap-sideband-resolved rf spectroscopy of weakly bound molecules. *Phys. Rev. Lett.*, 110(135301), 2013.

[20] Esslnger T. Hansch T.W. Bloch I. Greiner M., Mandel O. Quantum phase transition from a superfluid to a mott insulator in a gas of ultracold atoms. *Nature*, 415(6867):39–44, 2002.

[21] G.Roati et all. K-39 bose-einstein condensate with tunable interactions. *Physical Review Letters*, 99(1):010403, 2007.

[22] J. Dalibard I. Bloch and W.Zwerger. *Rev.Mod.Phys.*, 80(885), 2008.

[23] T.Esslinger. *Annu.Rev.Condens.Matter Phys*, 1(129), 2010.

[24] Charles J. Joachain B.H.Bransden. *Physics of Atoms and Molecules.*

[25] M.Inguscio E.Arimondo and P.Violino. Experimental determinations of the hyperfine structure in the alkali atoms. *Rev. Mod. Phys.*, 49(1):31, 1977.

[26] Gehm M.E. *Preparation of an optically-trapped Degenerate Fermi Gas of 6Li: Finding the route to degeneracy.* PhD thesis, Duke University, 2003.

[27] J.Clarke B.Lu J.Walls, R.Ashby and W. Wijngaarden. Measurement of isotope shifts, fine and hyperfine structure splittings of the lithium d lines. 2002.

[28] T.W. Hänsch and A. Schawlow. *Opt. Commun.*, (13):68, 1975.

[29] M.Inguscio and L.Fallani. *Atomic Physics:Precise Measurements and Ultracold Matter.* Oxford University Press, 2013.

[30] G.Valtolina. Development of an experimental apparatus for the production and study of ultracold atomic gases of fermionic lithium. Master's thesis, Università degli studi di Milano Bicocca, 2012.

[31] J.Dalibard. Atomes ultra-froids. notes de cours rédigées par Jean Dalibard.

[32] S. Stellmer B. Pasquiou R. Grimm F. Schreck. Laser cooling to quantum degeneracy. *Phys. Rev. Lett.*, 110:263003, 2013.

[33] van der Straten P. Metcalf H.J. *Laser Cooling and Trapping.* Springer, 1999.

[34] Andrew T. Grier Igor Ferrier-Barbut Benno S. Rem Marion Delehaye Lev Khaykovich Frederic Chevy and Christophe Salomon. lambda-enhanced sub-doppler cooling of lithium atoms in d1 gray molasses. *Phy. Rev. A*, 87(1):063411, 2013.

[35] and D.M. Stamper-Kurn W.Ketterle, D.S. Durfee. Making, probing and understanding bose-einstein condensate. In *Bose-Einstein Condensation in Atomc Gases: Proceedings of the International School of Physics (EnricoFermi)*, Varenna, 1999.

[36] Frances A. Jenkins and Harvey E. White. *Fundamentals of optics.* 4th Edition. Mc Graw-Hill, 2005.

[37] CVI Melles-griot.

[38] J.Dalibard and C.Cohen-Tannoudji. *J.Opt.Soc.Am.B*, 6(2023), 1989.

[39] D.Rio Fernandes F.Sievers N.Kretzschmar S. Wu C.Salomon and F.Chevy. Sub-doppler laser cooling of fermionic 40k atoms in three- dimensional gray optical molasses. *EPJ*, 2012.

[40] H.Smith C.J. Pethick. *Bose-Einstein condensation in dilute gases*. Cambridge University Press, 2002.

[41] W. S. Bakr A. Peng M. E. Tai R. Ma J. Simon J. I. Gillen S. Fölling L. Pollet M. Greiner. Probing the superfluid–to–mott insulator transition at the single-atom level. *Science*, 329(5991):547–550, 2010.

[42] Jacob F. Sherson Christof Weitenberg Manuel Endres Marc Cheneau Immanuel Bloch and Stefan Kuhr. Single-atom-resolved fluorescence imaging of an atomic mott insulator. *nature*, 467:68–72, 2010.

[43] Stoner. *Philosophical magazine series*, 7(15):1018, 1933.

[44] G.-B. Jo et al. *Science*, 325:1521, (2009).

[45] Lei Wang Ilia Zintchenko and Matthias Troyer. Ferromagnetism of the repulsive atomic fermi gas: three-body recombination and domain formation. *arXiv*, 1308.1961v1([cond-mat.quant-gas]), 8 Aug 2013.

[46] A.Barone G.Paternò. *Physics and applications of of the Josephson effect*. (Wiley), 1982.

[47] Tarik Yefsah Ariel T. Sommer Mark J. H. Ku Lawrence W. Cheuk Wenjie Ji Waseem S.Bakr Martin W. Zwierlein. Heavy solitons in a fermionic superflud. *Nature*, 499:426, 2013.